Longitudinal Dispersion in Vegetated Flow

by

Enda Murphy

Submitted to the Department of Civil and Environmetal Engineering
in partial fulfillment of the requirements for the degree of

Master of Science in Civil and Environmental Engineering

at the

MASSACHUSETTS INSTITUTE OF TECHNOLOGY

June 2006

Author .....
Department of Civil and Environmetal Engineering
May 12, 2006

Certified by .....
Heidi M. Nepf
Professor of Civil and Environmental Engineering
Thesis Supervisor

Accepted by .....
Andrew J. Whittle
Chairman, Departmental Committee for Graduate Students

Longitudinal Dispersion in Vegetated Flow

by

Enda Murphy

Submitted to the Department of Civil and Environmetal Engineering
on May 12, 2006, in partial fulfillment of the
requirements for the degree of
Master of Science in Civil and Environmental Engineering

Abstract

Vegetation is ubiquitous in rivers, estuaries and wetlands, strongly influencing both water conveyance and mass transport. The plant canopy affects both mean and turbulent flow structure, and thus both advection and dispersion. Accurate prediction of the fate and transport of nutrients, microbes, dissolved oxygen and other scalars depends on our ability to quantify vegetative impacts. In this thesis, the focus is on longitudinal dispersion, which traditionally has been modeled by drawing analogy to rough boundary layers. This approach is inappropriate in many cases, as the vegetation provides a significant dead zone, which may trap scalars and augment dispersion. The dead zone process is not captured in the rough boundary model.

This thesis describes a new theoretical model for longitudinal dispersion in a vegetated channel, which isolates three separate contributory processes. To evaluate the performance of the model, tracer experiments and velocity measurements were conducted in a laboratory flume. Results show that the mechanism of exchange between the free stream and the vegetated region is critical to the overall dispersion, and is primarily controlled by the canopy density. A numerical random walk particle-tracking model was developed to assess the uncertainty associated with the experimental data. Results suggest that the time scale required to obtain sound experimental data in tracer studies is longer than the commonly used Fickian time scale.

Thesis Supervisor: Heidi M. Nepf
Title: Professor of Civil and Environmental Engineering

Acknowledgments

This material is based upon work supported by the National Science Foundation under Grant No. EAR-0309188. Any opinions, findings, and conclusions or recommendations expressed in this material are those of the author(s) and do not necessarily reflect the views of the National Science Foundation. Financial support was also provided by a Fulbright/Marine Institute Scholarship (2004-2005).

I would like to thank my advisor, Heidi Nepf, for her insight, enthusiasm, and direction. I am particularly thankful for her encouragement during my time at MIT. I count myself extremely lucky to have had an advisor who is both an outstanding professional and a welcoming, amicable person. I could not have found a better role model for the future.

Thanks to members of the Nepf research group, past and present, for their help, suggestions, and ideas – particularly Marco Ghisalberti, Anne Lightbody, Lindsey Sheehan, Yukie Tanino and Brian White. I am extremely thankful to Peter Israelsson, for his help with the numerical model. I would like to thank Jeff Tester for providing additional financial support and enabling me to pursue my interests in sustainable energy. I wish to acknowledge all the faculty at Parsons who contributed to my learning in some way, including Pete Shanahan, Eric Adams, Harry Hemond, Chiang Mei and Roman Stocker. Special thanks must go to Ole and Grace Madsen, for sharing their wisdom, friendship and humour. I am lucky to have made some great friends at MIT, in people like Bob and Nona, Cathal, Conor, Dan and Shari, Frank, Mack, Paudie, and Rory, to name but a few.

Now, to the people that really matter. I am very lucky to have a wonderful family – Matt, Marian and Jess. They have always supported, encouraged and inspired me, in my work and in my life. I hope they know how much I appreciate them. Finally and most of all, I want to thank Cathy, who makes everything I do worthwhile. Her love, patience, wit, strength and support make me very happy. I am thankful for every second that I spend with Cathy and this thesis is dedicated to her.

Contents

List of Figures

List of Tables

Chapter 1

Introduction: The Role of Vegetation in Waterways

Traditionally, vegetation has been removed from waterways to improve conveyance [64]. Coupled with increased nutrient loading and deteriorating water quality, this has led to a decline in submerged aquatic vegetation populations worldwide [25]. This is highly unsatisfactory, since submerged vegetation is both an indicator of, and a contributor to, good water quality [79, 25]. It is known that vegetation directly improves the quality of coastal and inland waters through nutrient uptake and oxygen production [48]. Submerged aquatic vegetation also plays an important ecological role, providing habitat, food and breeding grounds for finfish, shellfish, crustaceans and waterfowl [25, 23, 90, 79]. Dense, submerged plant stands afford refuge to zooplankton from predatory fish [102]. Roots, leaves and stems of aquatic vegetation provide complex anoxic-oxic interfaces on which microbiota thrive [82], and stabilize sediments containing invertebrate life. Thus channelization activities, while highly effective at reducing flood risk [8], introduce serious ecological implications through the removal of vegetation cover. This illustrates the conflicts faced by hydraulic engineers in relation to vegetated aquatic systems. Understanding of the interplay between physical, biological and chemical processes in these systems will facilitate more sustainable water resource management. This chapter examines the role of vegetation in waterways, and motivates a closer investigation of the effects of submerged

vegetation on mass transport, which is the underlying theme of this thesis.

In aquatic systems, the primary impact of submerged vegetation is an increase in flow resistance and subsequent reduction in conveyance capacity [54, 103, 104, and references therein]. Therefore, the conventional approach to flood management has been to dredge river and channel beds to improve hydraulic efficiency [8]. However, this may alter natural channel processes, and deprive channel banks of sediments crucial to the maintenance of floodplain elevations [23]. Constructed levees and bank stabilization practices reduce connectivity between rivers and their floodplains, preventing natural flooding and sedimentation, which are critical to the survival of riparian wetlands. Such wetlands promote sedimentation and increase bank resistance, thereby providing a natural defense against flooding. In addition, riparian wetlands help to dissipate storm surge, and dampen the impacts of waves [23]. Removal of biomass from channel beds adversely affects channel ecology and bed stability, as experienced in the Mississippi river, a prime example of the negative effects of channelization [7]. Improved conveyance of the Mississippi river and its tributaries through channelization has resulted in the sediment load being deposited further downstream [23]. This is a potential contributor to severe eutrophication in the Gulf of Mexico (second only to the Baltic Sea in terms of hypoxic area [89]), due to enhanced nutrient loading carried with the sediments and loss of riverine wetlands as nutrient sinks. In recent times, river restoration projects have commonly involved planting of aquatic vegetation to enhance biodiversity and improve bed stability [7, 8]. Further research is needed to establish the long-term impacts of such schemes on riverine water quality and on ecosystems in general [8].

Water quality is heavily influenced by aquatic vegetation. Submerged macrophytes sequester nitrogen and phosphorus, such that some researchers have advocated widespread planting in waterways [66]. The fate and transport of contaminants is also indirectly affected by the presence of vegetation, which dramatically alters flow dynamics [36]. Reduced velocities due to canopy drag cause particulate matter, such as sediment grains, heavy metals and pesticides to settle out of the water column [58, 59, 63, 83]. Bed shear stress is also reduced, preventing resuspension of polluted

sediments [97]. The baffling effect of vegetation suppresses turbulence [69], which influences the growth and distribution of organisms such as phytoplankton [57]. Residence time within the canopy is affected by vegetation density [80, 97, 47], which has implications for the transport of dissolved substances and chemical kinetics.

Constructed wetlands containing emergent species of vegetation have found widespread use for treatment of wastewater and contaminated stormwater [48]. The ability of wetlands to remove a variety of contaminants, ranging from heavy metals [81] to nitrogen [111], make them particularly effective at treating diffuse sources of pollution [26], typically arising from activities such as agriculture, mining and forestry. However, it has been difficult to achieve high phosphorus removal efficiencies using wetlands containing only emergent species [26]. This is because phosphorus is typically retained in plant tissue (or sediments at the bed) [66, 26], unlike nitrates for example, which are subject to removal in the gas phase through denitrification. The result is that the land areas required to remove large quantities of phosphorus are prohibitive [111, 26], such that in many countries constructed wetlands are used only to perform tertiary "polishing" treatments [42]. However, recent research has shown that phosphorus removal may be greatly enhanced by the presence of submerged vegetation [66, 26]. Submerged macrophytes can absorb phosphorus directly from the water column, whereas emergent vegetation is limited to supply from the sediment [40]. Almost the entire surface area of a submergent plant is exposed to water, allowing for greater contaminant removal than that by an emergent plant, which is mostly above the surface [66]. Therefore, there is potential for improved wetland design and channel management, through incorporation of submergent plant species such as *Triglochin huegelii*, *Najas guadalupensis* and *Ceratophyllum demersum* [66, 26].

The ability of vegetation to remove pollutants from contaminated water is directly linked to the time which each particle spends in close contact with the plants [61]. The mean residence time is often used to characterize the average time spent by water particles in a given system. For uniform flow conditions, mean residence times increase with vegetation density [47], which could be thought of as favorable for water treatment purposes. However, the real measure of hydraulic efficiency for water

quality control is the distribution of residence times about the mean. If all water particles spend the same amount of time in a system (and thus receive the same level of treatment), 'plug flow' conditions exist [120]. However, in real vegetated flows, longitudinal mixing will result in a distribution of residence times, such that individual water particles will experience varying levels of treatment. Therefore, understanding residence time distributions is critical to implementation of efficient water quality control. The longitudinal dispersion coefficient is a widely used parameter in water quality modeling that describes the rate of mixing in the longitudinal direction. The fact that it provides estimates which are cross-sectional averages makes it an extremely useful parameter in the context of rivers and other environments where flow is essentially unidirectional. Since residence times are affected by longitudinal mixing, accurate prediction of the longitudinal dispersion coefficient will improve our ability to quantify contaminant removal by submerged vegetation. A review of longitudinal dispersion theory is given in Chapter 2, with particular reference to riverine applications.

The water depth-to-plant height ratio is another important hydrodynamical constraint [74], and dictates the availability of light [25], oxygen and nutrients to the vegetation. Responses to water level change vary according to the type of vegetation [45]. Fluctuations in the free surface elevation affect flowering, seed dispersal and plant growth rates [66, 10, and references therein]. Submergent macrophytes may adapt to changes in water level by changing their morphologies and biomass distributions, depending on species [39]. This affects the plant surface area available for nutrient uptake and as habitat for micro-organisms [66]. Many species of submerged aquatic vegetation are native to coastal waters, where they are subject to continuously changing water depths (due to waves, tides and seasonal changes) [79]. Thus over very short periods, the flow regime may change from a simple boundary layer (corresponding to thoroughly submerged vegetation and a logarithmic velocity profile) to a complex flow through emergent stems and leaves. To date, no studies have examined the effect of changes in water level on mass transport processes in flows containing submerged vegetation. This study addresses this issue, by developing a predictive

model for the dispersion coefficient in the transition between flows containing deeply submerged and emergent vegetation. The hydrodynamics of this transition have been investigated previously in detail [34, 74], and this provides a useful starting point.

In addition, recent work has shown in more detail how submerged vegetation dramatically alters the mean and turbulent structure of the flow [46, 37, 85]. In particular, the velocity profile is far from logarithmic over the full depth, so that traditional treatments of longitudinal dispersion in open channels cannot be directly applied to vegetated channels. Flow within vegetated zones is distinct from that in unobstructed regions. Aquatic plants are sinks for momentum and scalars, creating dead zones, which affect dispersion. While dispersion in flows with emergent vegetation has been studied [72, 122, 62], the effects of submerged vegetation on dispersion have not to date been fully investigated.

The aim of this thesis is to develop a predictive model for the longitudinal dispersion coefficient in flows containing submerged vegetation. Insight into dispersion in vegetated flows will provide a basis for greater understanding of the transport of contaminants, nutrients and sediments in natural channels. This is critical to improving channel management and water quality control methodologies. A secondary objective is to develop a particle-tracking model, which will eventually be a useful tool for predicting residence times and pollutant uptake by submerged vegetation.

Chapter 2

Theory

There have been many studies of the hydrodynamics of flow in systems containing both submerged [29, 64, 74, 71, 35, 36, 37, 38, 11, 84, 54, 65] and emergent [121, 62, 73, 69, 41, 67] vegetation. Initially, analyses were limited to flow above submerged vegetation, and in-canopy flow was neglected. Velocity profiles were observed to be logarithmic at some distance above the vegetation [54, 74, 11], suggesting a rough boundary layer form. Later work focused on flow within emergent arrays, which provided a greater basis for understanding the effects of vegetation on hydrodynamics. More recently, flow at the top of a canopy has been shown to closely resemble a mixing layer [36, 35], containing an inflection point in the velocity profile. Both the boundary layer and mixing layer analogies provide useful insights to mass transport processes in vegetated channels. In this chapter, we explain the terminology used to describe vegetated flows, develop theory for the transport of momentum and mass, and show how it leads to a model for a dispersion coefficient for vegetated channels.

2.1 Canopy Morphology

In this study, the term "canopy" refers to an array of aquatic vegetation, which we model by rigid circular cylinders (see e.g., [69, 38, 122]). Rigid, cylindrical stems have similar physical properties to salt-marsh vegetation species, such as *Spartina alterniflora* and *Juncus roemerianus*, which are relatively stiff and emergent [69, 58].

However, most submergent vegetation in rivers and natural channels exhibits some degree of bending. Previous attempts have been made to match the flexural rigidities of model vegetation to prototypes [74, 36, 54, 46, 103, 115, 12]. As discussed in [116], flexible vegetation can be associated with significant plant-flow interaction (e.g. monami - a periodic waving of the vegetation [74, 36]). To first order, these dynamics are considered less important than the mean flow structure, in particular the difference between canopy and overflow. Therefore, for simplicity we adopt a simple model canopy of rigid, circular cylinders.

Plant-geometry and stem packing-density are important parameters that describe canopy morphology. We assume that stems are uniformly distributed, but in a random configuration, i.e. the average density is spatially constant but the stems are not aligned in any regular pattern. The physical impedance that real vegetation provides to the flow is a function of vertical position within the canopy [116, 74, 58, 62]. Therefore, for a vertical slice i of thickness Z_i, we introduce the canopy density parameter

$$a_i(z) = \frac{NA_i(z)}{\Delta x \Delta y Z_i(z)} \tag{2.1}$$

[74]. Here, N is the number of plants in a plan area Δx by Δy. A_i is the frontal area of the vegetation in the slice. Terrestrial canopy studies usually adopt a vertical average of $a(z)$, so that a single parameter can be used to describe the canopy. A common metric is the leaf area index [91, 74, and references therein] LAI, given by

$$LAI = \int_0^h a(z)\, dz. \tag{2.2}$$

For a canopy consisting of vertical cylinders, $a \neq f(z)$, such that a is the frontal area per unit volume of the entire canopy. Of course, a will be spatially inhomogeneous in a real canopy and this may greatly influence mass transport [62, 58]. For simplicity, this is not considered here. The dimensionless density, ad (where d is the mean diameter of the vegetation), represents the solid volume fraction within the canopy. Field values of ad range from sparse ($ad < 0.1$) in rivers, lakes and salt marshes, to extremely dense (up to $ad \simeq 0.4$ [67]) in mangrove swamps.

The total height of the canopy, h, is another important descriptor of vegetation morphology. Specifically, the ratio of the canopy height to the water depth (H) is of critical importance to flow hydrodynamics [74]. The height of vegetation in the field is expected to range from $O(1\,\mathrm{cm})$ in rivers and surface-flow wetlands to $O(1\,\mathrm{m}) - O(10\,\mathrm{m})$ in kelp forests [20].

2.2 Vegetated Flow Hydrodynamics

2.2.1 Momentum Balance

Transport of momentum in vegetated flows is governed by the Navier-Stokes equations for incompressible flow of an isothermal Newtonian liquid with constant density and viscosity, namely

$$\rho\frac{D\underline{v}}{Dt} = -\underline{\nabla}p + \mu\nabla^2\underline{v} + \rho\underline{g} \tag{2.3}$$

and continuity,

$$\underline{\nabla}\cdot\underline{v} = 0. \tag{2.4}$$

Here and afterwards, a single underbar represents a vector quantity and a double underbar denotes a tensor. $\underline{v} = (u, v, w)$ is the velocity vector, defined in terms of a right-handed cartesian co-ordinate system with position vector components, x, y, and z in the downstream horizontal, transverse horizontal, and vertical directions, respectively. p is the mechanical pressure, μ is the dynamic viscosity of the fluid (which is assumed to be water), and ρ is the fluid density. $\underline{g} = (g\sin\beta, 0, g\cos\beta)$ is a body force vector in which only gravitational forces are considered, i.e., g is the acceleration due to gravity and β is the bed slope. $\underline{\nabla} = (\frac{\partial}{\partial x}, \frac{\partial}{\partial y}, \frac{\partial}{\partial z})$ is the del operator, $\nabla^2 = \underline{\nabla}\cdot\underline{\nabla}$ is the Laplacian, and $\frac{D}{Dt}$ denotes the material derivative, defined by

$$\frac{D}{Dt} = \frac{\partial}{\partial t} + \underline{v}\cdot\underline{\nabla}. \tag{2.5}$$

Flow in field conditions is usually turbulent to some degree. To resolve mean quantities in turbulent flows, it is necessary to separate variables in (2.3) into mean

and temporally fluctuating components. This process, known as Reynolds' decomposition, yields

$$\underline{v} = (u, v, w) = (\overline{u} + u', \overline{v} + v', \overline{w} + w') \tag{2.6}$$

and

$$p = \overline{p} + p', \tag{2.7}$$

where overbars and primes denote temporal averages and fluctuations, respectively. The decomposed variables are substituted into (2.3) and (2.4) and then all terms are time-averaged. All of the terms containing single fluctuation components conveniently drop out, since they time average to zero. Continuity becomes

$$\underline{\nabla} \cdot \underline{\bar{v}} = 0. \tag{2.8}$$

For brevity and clarity, it is convenient to consider only the x-component of the non-conservative, time-averaged momentum equation:

$$\frac{\partial \bar{u}}{\partial t} + \bar{u}\frac{\partial \bar{u}}{\partial x} + \bar{v}\frac{\partial \bar{u}}{\partial y} + \bar{w}\frac{\partial \bar{u}}{\partial z} + \frac{\partial \overline{u'u'}}{\partial x} + \frac{\partial \overline{u'v'}}{\partial y} + \frac{\partial \overline{u'w'}}{\partial z} = -\frac{1}{\rho}\frac{\partial \bar{p}}{\partial x} + \frac{\mu}{\rho}\left(\frac{\partial^2 \bar{u}}{\partial x^2} + \frac{\partial^2 \bar{u}}{\partial y^2} + \frac{\partial^2 \bar{u}}{\partial z^2}\right) + g\sin\beta. \tag{2.9}$$

All of the steps that follow are completely analogous for the y- and z-components of the Navier-Stokes equation. Although the last three terms on the left-hand side of (2.9) are generated by Reynolds' averaging of the convective inertial terms in (2.3), the convention is to combine them with the viscous terms on the right-hand side, such that they are viewed as stresses. The resulting x-momentum equation is

$$\frac{\partial \bar{u}}{\partial t} + \bar{u}\frac{\partial \bar{u}}{\partial x} + \bar{v}\frac{\partial \bar{u}}{\partial y} + \bar{w}\frac{\partial \bar{u}}{\partial z} = -\frac{1}{\rho}\frac{\partial \bar{p}}{\partial x} + \nu\left(\frac{\partial^2 \bar{u}}{\partial x^2} + \frac{\partial^2 \bar{u}}{\partial y^2} + \frac{\partial^2 \bar{u}}{\partial z^2}\right) + \frac{1}{\rho}\left(\frac{\partial\left[-\rho\overline{u'u'}\right]}{\partial x} + \frac{\partial\left[-\rho\overline{u'v'}\right]}{\partial y} + \frac{\partial\left[-\rho\overline{u'w'}\right]}{\partial z}\right) + g\sin\beta, \tag{2.10}$$

where $\nu = \mu/\rho$ is a kinematic viscosity. This equation can also be written as

$$\frac{\partial \bar{u}}{\partial t} + \bar{u}\frac{\partial \bar{u}}{\partial x} + \bar{v}\frac{\partial \bar{u}}{\partial y} + \bar{w}\frac{\partial \bar{u}}{\partial z} = -\frac{1}{\rho}\frac{\partial \bar{p}}{\partial x} + \frac{1}{\rho}\left(\frac{\partial \overline{\tau_{xx}}}{\partial x} + \frac{\partial \overline{\tau_{yx}}}{\partial y} + \frac{\partial \overline{\tau_{zx}}}{\partial z}\right) + g\sin\beta \qquad (2.11)$$

where we define

$$\overline{\tau_{xx}} = \mu\frac{\partial \bar{u}}{\partial x} - \rho\overline{u'u'} \qquad (2.12)$$

$$\overline{\tau_{yx}} = \mu\frac{\partial \bar{u}}{\partial y} - \rho\overline{u'v'} \qquad (2.13)$$

$$\overline{\tau_{zx}} = \mu\frac{\partial \bar{u}}{\partial z} - \rho\overline{u'w'}. \qquad (2.14)$$

The terms in (2.12)-(2.14) that contain the auto- and co-variances of the turbulent velocity fluctuations are thus referred to as Reynolds' stresses, even though they originate from convective acceleration terms. Further simplifications can be made if we assume steady ($\frac{\partial}{\partial t} = 0$), uniform ($\frac{\partial}{\partial x} = 0$), two-dimensional ($\frac{\partial}{\partial y} = 0$) flow in the longitudinal direction. From continuity and the no-flux boundary condition at the bed, $\bar{w}(z = 0) = 0$, the temporal mean of the vertical velocity is zero everywhere, such that (2.11) reduces to

$$0 = \frac{1}{\rho}\frac{\partial \overline{\tau_{zx}}}{\partial z} + g\sin\beta. \qquad (2.15)$$

Similarly, the z-momentum equation simplifies to

$$0 = -\frac{1}{\rho}\frac{\partial \bar{p}}{\partial z} + \frac{1}{\rho}\frac{\partial \overline{\tau_{zz}}}{\partial z} - g\cos\beta. \qquad (2.16)$$

Integrating (2.16) with respect to the vertical and applying the boundary condition $\bar{p} = 0$ at $z = H$, we obtain the pressure distribution

$$\bar{p} = \rho g\cos\beta\,(H - z) + \overline{\tau_{zz}}. \qquad (2.17)$$

Except for just at the surface (i.e., $z = H$), we would expect that hydrostatic pressure completely dominates the stress due to turbulent fluctuations in the vertical velocity component. Furthermore, $\partial w/\partial z = 0$ from conservation of mass, so we conclude that

$\overline{\tau_{zz}} = 0$. (2.17) then reduces to

$$\bar{p} = \rho g \cos\beta \, (H - z) \, . \tag{2.18}$$

Thus far, we have considered the equations of fluid motion at a single point, and the effects of vegetation on the governing equations have not been considered. The presence of an array of cylinders introduces heterogeneities in the velocity field at scales that are too small to be of interest if we want to consider dispersion on the scale of many water depths. To characterize transport on a macroscopic scale, some sort of spatial averaging needs to be applied to the governing equations. This is generally carried out directly after the Reynolds' decomposition and time-averaging. The spatial-averaging process is completely analogous to the Reynolds' averaging and results in the generation of additional dispersive terms due to spatial deviations from the mean in-canopy velocity [64]. These are parameterized by a bulk drag coefficient, defined as

$$C_D = \frac{\langle F_D \rangle}{\frac{1}{2} a \langle \overline{u^2} \rangle}, \tag{2.19}$$

where F_D is the drag force per unit mass of fluid and angle brackets denote spatial averaging in the horizontal plane over a scale larger than the stem spacing.

Lopez and Garcia [64] emphasize that the drag term arises as a consequence of the spatial averaging process, which does not require artificial introduction of a quadratic drag expression into the momentum equation (as in, e.g., [56]). In any event, the one-dimensional, spatially-averaged, x-component of momentum becomes

$$0 = \frac{1}{\rho} \frac{\partial \langle \overline{\tau_{zx}} \rangle}{\partial z} + g \sin\beta - \frac{1}{2} C_D a \langle \overline{u^2} \rangle. \tag{2.20}$$

Strictly speaking, the gravitational term should be modified to account for reduced body force in the fluid due to the volume occupied by cylinders. However, this correction is generally expected to be negligible for sparse canopies [74]. For high Reynolds' number flows (which occur at moderate velocities in water, since the viscosity is rela-

tively low[1]), viscous stresses are only important in very narrow boundary layers [95, pp. 79]. Therefore, (2.20) can be simplified further, yielding

$$0 = -\frac{\partial \langle \overline{u'w'} \rangle}{\partial z} + g \sin\beta - \frac{1}{2} C_D a \langle \overline{u^2} \rangle. \tag{2.21}$$

For clarity, we will henceforth denote the channel slope by S, such that $S = \sin\beta$.

If we consider a channel containing submerged vegetation (as shown in Figure 2-1), we can divide the flow into two vertical layers: (i) The unvegetated region, $h < z < H$, and (ii), the in-canopy zone, $0 < z < h$. Evaluating (2.21) for the unvegetated zone, we see that the drag term is zero. We are then left with a balance between gravity and Reynolds' stress. Assuming that $\langle \overline{u'w'} \rangle|_H = 0$ and integrating with respect to z over the entire layer, we find

$$gS(H-h) = \langle \overline{u'w'} \rangle|_h \equiv u_*^2. \tag{2.22}$$

u_* is a friction velocity, which characterizes the momentum flux at the top of the canopy. Note the distinction from the classic friction velocity for an open channel, which is given by $u_{*H} = \sqrt{gSH}$ [33, pp. 21].

Now, focusing our attention on flow within the canopy region, and integrating (2.20) over the vertical, we obtain

$$gSh = -u_*^2 + \frac{1}{2} C_D a \int_0^h \langle \overline{u^2} \rangle \, dz. \tag{2.23}$$

Bed drag is ignored, since it is negligible in comparison to vegetation drag for dimensionless densities $ad \geq 0.01$ [69]. As discussed in [74], (2.23) or (2.21) can be used to estimate the bulk drag coefficient for an array of plants, once mean and turbulent velocity statistics are known.

[1]See 2.2.2 for a full discussion of Reynolds' numbers.

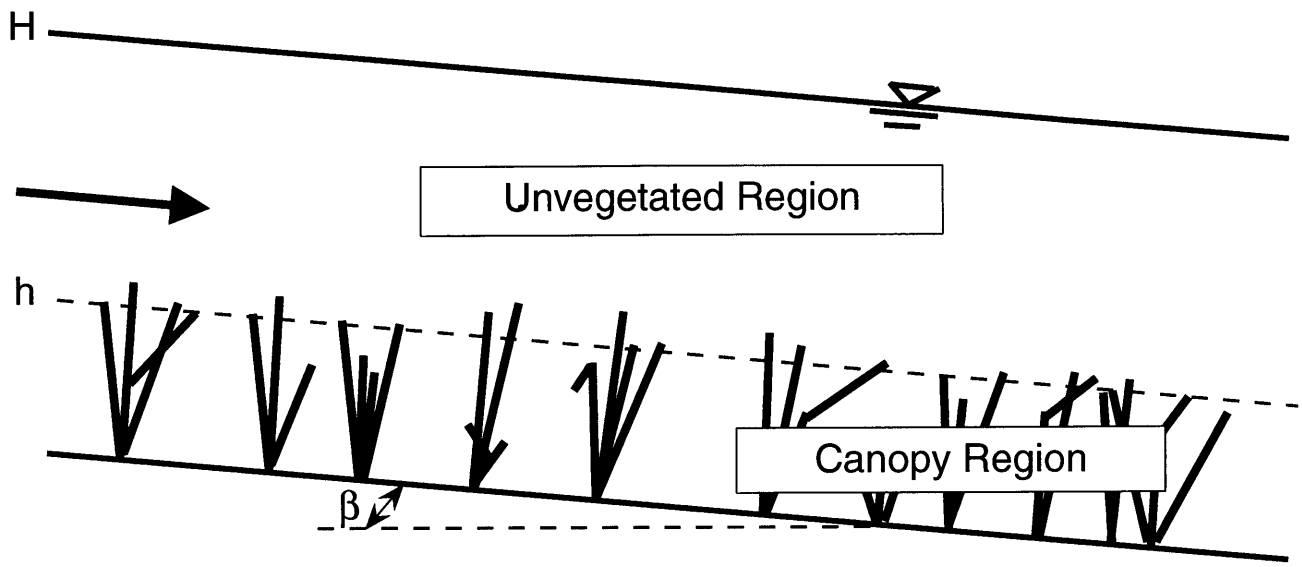

Figure 2-1: Schematic of channel containing submerged vegetation

2.2.2 Reynolds' Number

From §2.2.1, it should be clear that the full Navier-Stokes equations are too complex for many practical applications, and it is necessary to make simplifying assumptions (e.g., the neglect of viscous terms in §2.2.1). Such assumptions can be formally justified by non-dimensionalizing (2.3) with carefully chosen length (L), velocity(V) and pressure (P) scales. Using these scales, we introduce the dimensionless variables

$$\underline{x}^* = \frac{\underline{x}}{L}, \qquad \underline{v}^* = \frac{\underline{v}}{V}, \qquad P^* = \frac{p}{P}.$$

The Navier-Stokes equations then become

$$\frac{D\underline{v}^*}{Dt^*} = -\underline{\nabla}^* P^* + \frac{\mu V}{L}\frac{1}{P}\nabla^{*2}\underline{v}^* + \frac{gL}{V^2} \tag{2.24}$$

$$\underline{\nabla}^* \cdot \underline{v}^* = 0, \tag{2.25}$$

where $t^* = \underline{x}^*/\underline{v}^*$ and $\nabla^* = L\nabla$. For inertia-dominated flows, the pressure scale can be chosen as $P = \rho V^2$, such that (2.24) yields

$$\frac{D\underline{v}^*}{Dt^*} = -\underline{\nabla}^* P^* + \left(\frac{\mu}{\rho V L}\right) \nabla^{*2} \underline{v}^* + \left(\frac{gL}{V^2}\right). \tag{2.26}$$

If appropriate scales have been chosen, every term in (2.26) with a '*' superscript is of order unity. Thus, the relative importance of each term depends only on the dimensionless coefficients, which are

$$Re = \frac{\rho V L}{\mu} = \frac{VL}{\nu} = \frac{\text{inertial forces}}{\text{viscous forces}} = \text{Reynolds' Number}$$
$$Fr^2 = \frac{gL}{V^2} = \frac{\text{body forces}}{\text{inertial forces}} = (\text{Froude Number})^2.$$

In §2.2.1, we assumed $Re \gg 1$, such that viscous forcing was negligible.

The Reynolds' number is a very powerful descriptor of flow characteristics but its usefulness is entirely dependent on choice of the appropriate length and velocity scales, L and V, respectively. For example, in vegetated flows, there are many relevant length scales (plant diameter, plant height, water depth, etc.) and velocity scales (e.g., mean channel velocity, in-canopy velocity). Thus, the choice of parameters needs to be tailored to specific analyses.

The Reynolds' number is often used to characterize whether a flow is laminar, transitional or turbulent. For pipes, turbulent flow can be expected for $Re > 4000$, where the mean cross-sectional velocity and diameter are the relevant scales. Assuming that this transfers easily to open channel flow by replacing the diameter with the hydraulic radius, R_H, we find that turbulence should exist for $Re > 1000$ [13, pp. 120]. For an infinitely wide channel, $R_H \approx H$, and we can define a critical water-depth Reynolds' number as

$$Re_{H,cr} = \frac{UH}{\nu} = 1000, \tag{2.27}$$

where H is the water depth and $U = \frac{1}{H}\int_0^H \langle \bar{u} \rangle \, dz$. Re_H ranges from $O(1)$ to $O(10^5)$ in coastal and freshwater vegetated flows [58, 59, 61], depending on factors such as the degree of tidal inundation, rainfall, and location.

The stem-diameter Reynolds number, Re_d, is used to describe dispersion on the scale of individual plant elements. We define $Re_d = \frac{\langle \bar{u} \rangle d}{\nu}$ for flow in a random cylinder array, where $\langle \bar{u} \rangle$ is the temporally and horizontally averaged velocity and d is the diameter of the cylinders. For $Re_d < 1$, flow past an isolated cylinder is essentially laminar (see Figure 2-2). As the Reynolds' number increases to $Re_d > 4$, the vorticity on the downstream face becomes sufficiently strong to generate two steady recirculating eddies [55, pp. 346]. Just beyond $Re_d = 40$, the wake becomes unstable and oscillates gently, until the vortices roll up and shed periodically (in alternate fashion) at around $Re_d = 55$. These vortices are carried downstream by the mean flow in what is known as a von Karman[2] vortex "street" (since they resemble staggered footprints). For $Re_d > 200$, the vortices themselves become turbulent and irregular, until any remaining periodicity becomes barely distinguishable for Reynolds' numbers greater than about 5000 [55, pp. 349]. This illustrates that the flow around a circular cylinder is extremely complex, resulting in non-linear mass transport processes, particularly when multiple cylinders are in such close proximity that their wakes intermingle and interact with one another [30, 28, 122]. The latter may result in a transition to turbulent vortices at $Re_d < 200$ for arrays of cylinders, particularly in finite, bounded canopies [122]. For real vegetated flows, $O(10^0) < Re_d < O(10^3)$ [61, 58, 59], such that the majority of flow conditions are in the regime where vortex shedding occurs.

2.2.3 Drag Coefficient

The bulk drag coefficient defined in §2.2.1 describes the ratio of total canopy drag to the dynamic pressure force. Much research has focused on determining the drag coefficient for isolated circular cylinders as a function of Re_d. The following curve fit from [123] provides an accurate prediction for an infinitely long, isolated cylinder:

$$C_{D,isolated} = 1 + 10.0 Re_d^{-2/3}, \qquad 1.0 < Re_d < 2 \times 10^5 \tag{2.28}$$

[2]After the Hungarian scientist, Theodore von Karman.

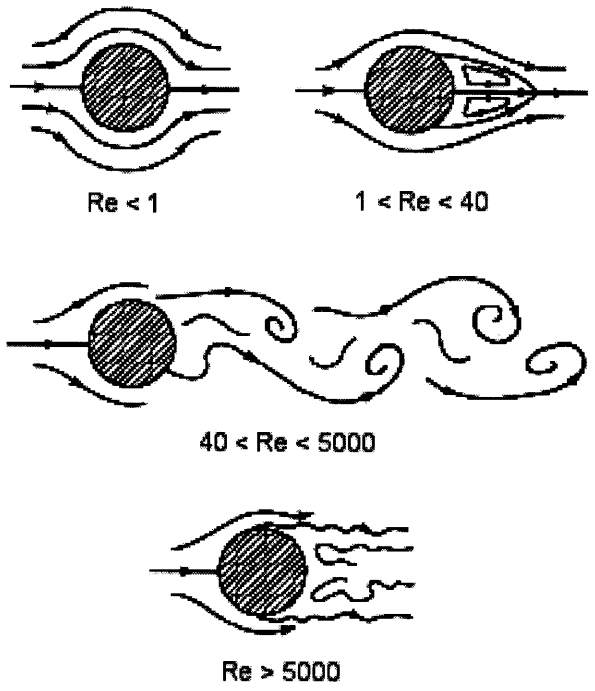

Figure 2-2: Regimes of flow past a circular cylinder.

However, the *bulk* drag coefficient for a submerged array is likely to differ from this, due to wake interaction [69] and free-end effects [37, 129]. For $Re_d > 200$, [69] showed that C_D decreases with increasing ad. The reverse has been observed for low Reynolds numbers ($Re_d \lesssim 50$), i.e. C_D increases with increasing solid volume fraction when viscous drag dominates [51].

2.2.4 Boundary-Layer and Mixing-Layer Theory

As discussed at the beginning of this chapter, the first analyses of vegetated flows were based on rough boundary-layer theory. The concept of boundary-layer theory was first put forward by Ludwig Prandtl in August 1904. Prior to this, fluid mechanicians had focused on solving the inviscid Euler equation, due to inherent mathematical difficulties in solving the Navier-Stokes equations for viscous flow. Prandtl showed that it was possible to analyse real flows for a number of special cases and that, in particular, the Navier-Stokes equations could be greatly simplified within the boundary layer. This breakthrough essentially brought together the divergent fields

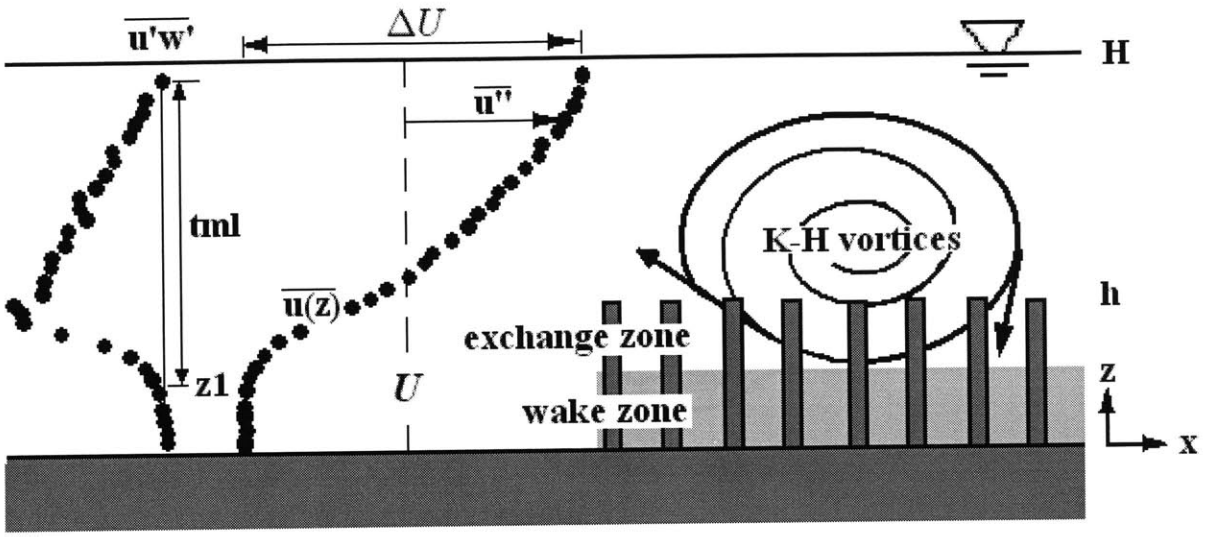

Figure 2-3: Typical shape of the Reynolds' stress and velocity profiles in a vegetated shear layer

of hydraulics and theoretical hydrodynamics. Blasius, a student of Prandtl, used similarity solutions to solve the boundary-layer equations for two-dimensional flows over a flat plate and a circular cylinder [55, pp. 330]. Then, in 1921, Theodore von Karman (another Prandtl student) integrated the boundary-layer equations across the thickness of the layer, allowing the theory to be applied to more complicated scenarios. The ubiquity of boundary layers in engineering applications and in everyday life has prompted extensive research, both theoretical and empirical. An exhaustive review of boundary-layer theory is given in Hermann Schlichting's classic text [95].

Many boundary-layer concepts have been applied to flows in the region above submerged vegetation [1, 11, 54, 2, 103, 12, 56]. However, a better mechanistic understanding of flow within vegetation [69, 73, 62, 80, 122] has prompted some revision of the philosophy concerning vegetated flows. As first presented by Raupach et al. [91], flows near the top of submerged vegetation more closely resemble mixing layers, rather than boundary layers (see Figure 2-3). A mixing layer is a confined region of shear (of size t_{ml}) that separates two regions of approximately constant velocity. The total velocity difference across the layer is denoted by ΔU. The mean velocity profile is closely approximated by a hyperbolic tangent [36], and contains an inflec-

tion point, which is a source of instability. Reynolds' stress profiles exhibit a sharp peak near the top of the canopy, and decay rapidly towards the bed and free surface [92, 36, 74, 64, 11, 115]. As in a free-shear-layer (e.g., [43]), the shear layer produced in vegetated flow is characterized by a street of coherent Kelvin-Helmholtz (K-H) vortices that dominate vertical transport between the canopy and overlying layer [46, 38]. These coherent structures do not always grow to encompass the entire flow depth [74]. Consequently, as shown in Figure 2-3, the canopy is often separated into an upper region of rapid vortex-driven transport (the "exchange zone") and a lower region with greatly reduced mixing [74]. Denoting the canopy height as h and the bottom of the shear layer as z_1, the exchange zone spans $z_1 < z < h$. Vertical mixing in the exchange zone is characterized by strong "sweeps" (inflows of high momentum fluid at the downstream end of the vortices) and "ejections" (upward flows out of the canopy from the tail of the vortices), as evident from periodicity in Reynolds' stress profiles (see Figure 9 of [36]). Vertical transport in the lower region (termed the "wake zone", $0 < z < z_1$) is dominated by stem-wake turbulence, with significantly smaller length and velocity scales than the shear-layer vortices. Consequently, the diffusivity in the wake zone (D_w) is typically an order of magnitude lower than that in the exchange zone [38]. Nepf et al. [70] showed that the penetration of shear $(h - z_1)$ into a vegetation canopy is inversely proportional to the drag coefficient and the canopy density parameter,

$$(h - z_1) \approx 0.2(C_D a)^{-1}. \tag{2.29}$$

The extent of vortex penetration, given by (2.29), is expected to have a tremendous impact on the overall rate of dispersion in the flow.

2.3 Fundamentals of Mass Transport

2.3.1 Governing Equations

This section reviews the equations of mass transport in incompressible fluid flows. It should be observed that many of the steps in the derivation of the three-dimensional mass transport equation are analogous to procedures in §2.2, where the transport of momentum is described. This is expected, since the only difference is that we are now dealing with the transport of scalars, instead of vectors.

The equation that governs the transport of scalar quantities (such as mass, thermal energy and electrical charge) is the advective-diffusive equation,

$$\frac{D\,c}{Dt} = D_m \nabla^2 c + \sum r \tag{2.30}$$

where D_m is a molecular diffusion coefficient, assumed to be constant and isotropic. $c(\underline{x}, t)$ is the concentration of the scalar quantity of interest. r represents production (+) or decay (-) and will be neglected in the following derivations to avoid complication. The instantaneous conditions represented by (2.30) can be decomposed into mean and temporally fluctuating components, in a manner completely analogous to the Reynolds' decomposition applied in §2.2, i.e.,

$$\underline{v} = \bar{\underline{v}} + \underline{v}' \tag{2.31}$$

$$c = \bar{c} + c'. \tag{2.32}$$

Similar to before, we substitute (2.31) and (2.32) into (2.30) and time-average. This removes terms with a single prime such that the governing equation for the transport of *mean* scalar quantities is

$$\frac{\partial \bar{c}}{\partial t} + \bar{\underline{v}} \cdot \underline{\nabla} \bar{c} = -\underline{\nabla} \cdot \overline{\underline{v}' c'} + D_m \nabla^2 \bar{c}. \tag{2.33}$$

The usual assumption is that the turbulent dispersive term can be represented by an

equivalent Fickian diffusion, i.e.,

$$\begin{aligned} -\underline{\nabla} \cdot \overline{\underline{v}'c'} &= \frac{\partial \left[-\overline{u'c'}\right]}{\partial x} + \frac{\partial \left[-\overline{v'c'}\right]}{\partial y} + \frac{\partial \left[-\overline{w'c'}\right]}{\partial z} \\ &= \frac{\partial}{\partial x}\left(D_x \frac{\partial \bar{c}}{\partial x}\right) + \frac{\partial}{\partial y}\left(D_y \frac{\partial \bar{c}}{\partial y}\right) + \frac{\partial}{\partial z}\left(D_z \frac{\partial \bar{c}}{\partial z}\right) \end{aligned} \tag{2.34}$$

where D_x, D_y, and D_z are non-isotropic, Fickian, eddy diffusivities. In turbulent flows, $D_x, D_y, D_z \gg D_m$ (except very close to boundaries where turbulence is damped), such that

$$\frac{\partial \bar{c}}{\partial t} + \bar{\underline{v}} \cdot \underline{\nabla} \bar{c} = \frac{\partial}{\partial x}\left(D_x \frac{\partial \bar{c}}{\partial x}\right) + \frac{\partial}{\partial y}\left(D_y \frac{\partial \bar{c}}{\partial y}\right) + \frac{\partial}{\partial z}\left(D_z \frac{\partial \bar{c}}{\partial z}\right). \tag{2.35}$$

This step, where molecular diffusion is ignored, is analogous to the neglect of viscous contributions to the momentum flux in §2.2. (2.35) is the mass conservative form of the three-dimensional advective-diffusive equation.

2.3.2 Turbulent Schmidt Number

In 1877, Boussinesq first defined a turbulent eddy viscosity (by analogy to the kinematic viscosity for laminar stresses),

$$\nu_{tz} = \frac{-\langle \overline{u'w'} \rangle}{\partial \langle \overline{u} \rangle / \partial z}, \tag{2.36}$$

which describes the rate at which momentum is diffused in a fluid. This parameterization of turbulent transport works very well, provided that eddies are smaller than the scale of the reference frame being considered. It should be clear from inspection of (2.35) and (2.36) that turbulent diffusivities are the mass transport analogues of the eddy viscosity. Since there is reasonably good understanding of the transport of momentum in turbulent flows, it is desirable to parameterize mass transport with this in mind. The dimensionless turbulent Schmidt number, Sc, is the ratio of turbulent viscosity to turbulent diffusivity:

$$Sc = \frac{\nu_{tz}}{D_z}. \tag{2.37}$$

Sc varies considerably across the width of boundary layers, from about 0.4 at the outer edge to 0.9 at the wall [53], with an average around 0.8 [38]. $Sc \approx 0.54$ for mixing layers and $Sc \approx 0.47$ for vegetated shear layers [38].

2.4 Longitudinal Dispersion

While (2.35) provides an accurate description of mass transport in bodies of water, resolution of concentration distributions in three dimensions is not usually necessary (or desired) for most engineering applications. This is especially the case in long, slender water bodies such as rivers, estuaries and wetland channels, where information about longitudinal concentration distributions is usually sufficient. The use of (2.35) under these conditions would be overkill, and possibly too computationally expensive, for most practical applications. Only transport in the x-direction need really be considered. Therefore, some spatial averaging is required to reduce the complexity of the governing equation. This idea led G.I. Taylor to investigate longitudinal dispersion, a concept that reduces scalar transport to a balance between differential advection and transverse diffusion, through cross-sectional averaging. Taylor first analyzed dispersion in laminar pipe flow in 1953 [106]. Aris corroborated Taylor's results with a more formal analysis in 1956 [3]. Taylor extended his theory to turbulent pipe flow [107] and Elder completed an analysis for open channels [31]. Much effort has gone into developing the theory for application to natural channels (see [32, 33] for reviews) but agreement between theory and observations is rare [118, 77, 22, 16, 49]. The following section reviews the derivation of the advection-dispersion equation, with the aim of applying it to real vegetated flows.

First, we define a cross-sectional average concentration as

$$C = \frac{1}{H}\int_0^H \langle \bar{c} \rangle \, dz, \tag{2.38}$$

and vertical perturbations from this mean as $\langle \bar{c}(z) \rangle'' = \langle \bar{c}(z) \rangle - C$. Applying similar decomposition to the velocity field, $\bar{u}(z,t)$, we substitute these expressions into

(2.35) to obtain a mass transport equation that is an average over the cross section. Assuming that the flow is non-divergent (i.e., no lateral inflow or outflow) and the cross section does not change appreciably over short distances in x, this yields

$$\frac{\partial C}{\partial t} + U\frac{\partial C}{\partial x} = \frac{\partial}{\partial x}\left(\langle D_x\rangle \frac{\partial C}{\partial x} - \langle \overline{u''c''}\rangle\right). \tag{2.39}$$

The assumption that gives rise to the definition of a longitudinal dispersion coefficient is that mass transport due to the spatial covariance, $\langle \overline{u''c''}\rangle$, approximately follows Fick's second law. Thus, it can be approximated by a constant times a concentration gradient, i.e.,

$$-\langle \overline{u''c''}\rangle \cong K_x \frac{\partial C}{\partial x}, \tag{2.40}$$

where K_x is an average longitudinal dispersion coefficient for the entire cross-section. Taylor showed that the covariance term representing differential advective mass transport in (2.39) is much more important than diffusive transport in the longitudinal direction. Therefore, $\langle D_x\rangle \ll K_x$, and the diffusive term in (2.39) can be dropped, yielding

$$\frac{\partial C}{\partial t} + U\frac{\partial C}{\partial x} = K_x \frac{\partial^2 C}{\partial x^2}, \tag{2.41}$$

which is the one-dimensional advection-dispersion equation.

Employing a moving co-ordinate system [33, pp. 83], Taylor showed that (after some initial time) the two-dimensional mass transport equation reduces to a balance between longitudinal advective transport and transverse diffusive transport, from which $\langle \overline{u''c''}\rangle$, and hence K_x, can be determined. The result is that K_x can be found by a triple integration, which for an open channel is given by

$$K_x = -\frac{1}{H}\int_0^H \langle \bar{u}\rangle'' \int_0^z \frac{1}{D_z}\int_0^z \langle \bar{u}\rangle'' dz\, dz\, dz \tag{2.42}$$

[31]. Elder evaluated (2.42) for an infinitely wide, straight open channel by assuming a logarithmic velocity profile and found that $K_x \simeq 6u_{*H}H$. However, Fischer [33, pp.128] showed that transverse horizontal velocity shear can have more of an effect than vertical shear on dispersion in real rivers. Under such conditions, he found that

experimentally determined dispersion coefficients could be up to three times greater than Elder's prediction. Elder's analytical prediction compares well to dispersion coefficients observed in very wide ($w_c/H \sim O(10)$, where w_c is the channel width), straight, rough-bottomed laboratory channels [32]. However, these conditions do not hold in most aquatic systems. For example, lateral nonuniformities in rivers and estuaries such as bends and dead zones can result in significant lateral shear and dramatically increased dispersion [22, 77, 21]. Likewise, the drag imparted by submerged vegetation generates velocity profiles and vertical mixing that differ significantly from those in a logarithmic boundary layer [38], invalidating several assumptions behind Elder's analysis. Discrepancies on the order of a factor of five between observed dispersion coefficients and rates predicted by (2.42) are not uncommon [22]. Even from a theoretical standpoint, a comparison of Taylor's [107] result for turbulent pipe flow to Elder's expression for the dispersion coefficient in an open channel (in terms of hydraulic radii) reveals substantial quantitative differences. This illustrates the point that, in practice, dispersion is highly dependent on channel geometry. Therefore, in channels with complex geometries, or with vegetated beds, a more complex and careful analysis of dispersion is required.

2.5 Dead-Zone Dispersion

Transient storage or dead-zone models were developed to explain observations of persistently skewed concentration distributions in natural channels [22, 77, 114]. Channel observations have led to widespread consensus that an accurate analysis of longitudinal dispersion must explicitly consider the effects of "dead", or "slow" zones [113, 19]. A dead zone is a region of reduced velocity and diminished turbulence caused by irregularities in channels or pipes, such as the inside of bends [101, 24, 99, 98, 32], channel sidearms [96], pools and riffles [98, 113], pockets in gravel beds [68, 6], hyporheic zones [68, 125, 126], wakes of bank structures [112, 33, 119], the viscous sub-layer [14] and vegetated regions [41, 88, 87, 125, 126]. Dead zones tend to trap scalars and hold them up relative to the main channel flow, thereby increasing longitudinal dispersion.

The idea that zones of reduced velocity could affect dispersion was first developed during the application of dispersion theory to gas chromatography and distillation. In 1959, Aris [4] found that the stationary phase of a tubular chromatographic column behaved as a thin retentive layer, which increased the dispersion coefficient in proportion to the quantity of mass retained. He derived the dispersion coefficient for a column of gas flowing within an annulus of liquid as a simple case and then generalized for co-axially flowing streams of arbitrary cross-section. A plethora of multi-layer models have since emerged (e.g., [108, 100, 19, 17, 93]), attempting to characterize the effect of transverse variability in pipe and open channel hydraulics. The basis for most of these analyses involves the application of coupled advection-dispersion equations to each region of the flow. There are numerous ways to approach the solution of these equations (see e.g., [19, 93]) but here we adopt a similar method to the one given by [18].

In 1986, Chikwendu [18] presented a prediction for the asymptotic longitudinal dispersion coefficient in a flow divided into an arbitrary number of layers. For simplicity, we will show the result for a two-layer system only, but the theory is easily extended for additional zones. The conceptual model is shown in Figure 2-4, which shows a two-dimensional (x and z) flow in an open channel divided into an upper fast zone ($h_1 < z < H$) and a slow zone near the boundary ($0 < z < h_1$). Constant mean velocities, U_1 and U_2), are assumed for the slow and fast zones, respectively. The two zones are assumed to be well-mixed with concentrations C_1 and C_2. The Taylor dispersion coefficients for the layers, K_1 and K_2, are obtained by evaluating (2.42) for each zone separately. Exchange between the zones is characterized by the exchange coefficient, b, with dimensions T^{-1}. Thus, the coupled advection-dispersion equations for each zone are

$$\frac{\partial C_1}{\partial t} + U_1 \frac{\partial C_1}{\partial x} = K_1 \frac{\partial^2 C_1}{\partial x^2} + b\left(\frac{H}{h_1}\right)(C_2 - C_1) \tag{2.43}$$

$$\frac{\partial C_2}{\partial t} + U_2 \frac{\partial C_2}{\partial x} = K_2 \frac{\partial^2 C_2}{\partial x^2} + b\left(\frac{H}{H - h_1}\right)(C_1 - C_2). \tag{2.44}$$

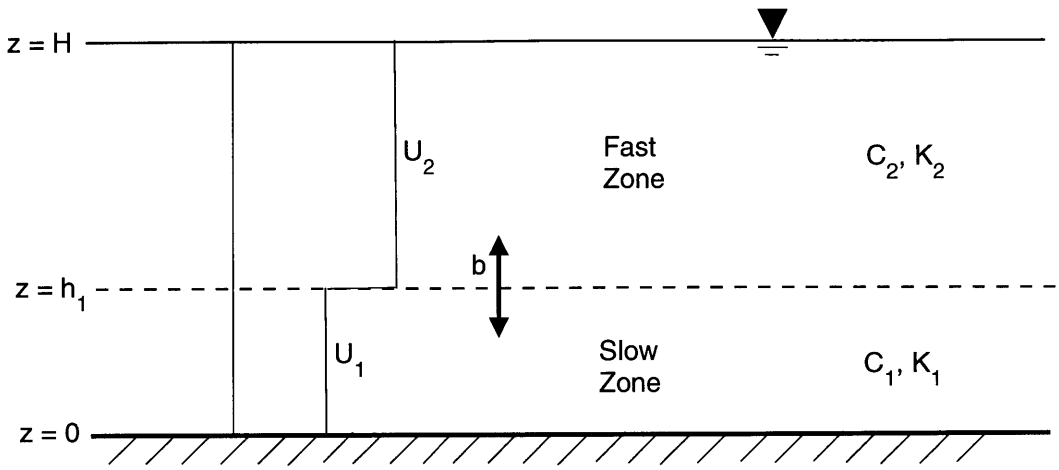

Figure 2-4: Slow zone model for an open channel.

The only difference between these equations and (2.41) is the inclusion of an additional coupling term to account for transfer of mass across the boundary of the zones ($z = h_1$).

The solution of this set of equations proceeds as follows. The Fourier transforms (see [105] for a review of Fourier transformations) of $C_1(x,t)$ and $C_2(x,t)$ are defined as

$$\hat{C}_1(k,t) = \int_{-\infty}^{\infty} C_1(x,t)e^{-ikx}\,dx \tag{2.45}$$

and

$$\hat{C}_2(k,t) = \int_{-\infty}^{\infty} C_2(x,t)e^{-ikx}\,dx, \tag{2.46}$$

respectively. Substitution of (2.45) and (2.46) into the partial differential equations, (2.43) and (2.44), reduces the problem to a system of ordinary differential equations:

$$\frac{\partial \hat{C}_1}{\partial t} + ikU_1\hat{C}_1 = -k^2K_1\hat{C}_1 + b\left(\frac{H}{h_1}\right)(\hat{C}_2 - \hat{C}_1) \tag{2.47}$$

$$\frac{\partial \hat{C}_2}{\partial t} + ikU_2\hat{C}_2 = -k^2K_2\hat{C}_2 + b\left(\frac{H}{H-h_1}\right)(\hat{C}_1 - \hat{C}_2). \tag{2.48}$$

Chikwendu and Ojiakor [19] assumed exponential solutions of the form $\hat{C}_1 = f(k)e^{\gamma(k)t}$

and $\hat{C}_2 = g(k)e^{\gamma(k)t}$, giving a characteristic equation of the system,

$$\gamma^2 + \gamma\left[ik(U_1+U_2) + k^2(K_1+K_2) + b\left(\frac{H}{h_1} + \frac{H}{H-h_1}\right)\right] + \left[ik^3(U_1K_2+U_2K_1) + k^2(k^2K_1K_2 - U_1U_2) + ikb\left(U_1\frac{H}{H-h_1} + U_2\frac{H}{h_1}\right)\right] = 0. \tag{2.49}$$

Since we are only interested in the dispersion coefficient in the Fickian limit[3] as $t \to \infty$, higher order terms in k disappear and $\gamma \approx ikB - k^2A$, where A and B are constants. We then plug this value for γ back into the expressions for $\hat{C}_1$ and $\hat{C}_2$. Taking an initial condition of $\hat{C}_1(k,0) = \hat{C}_2(k,0) = C_0$ (i.e., a line source), we invert $\hat{C}_1$ and $\hat{C}_2$ to find that the concentration distributions in the two layers are equal at long times and are given by

$$C(x,t) = \frac{C_0}{\sqrt{4\pi At}} exp\left[\frac{-(x-Bt)^2}{4At}\right]. \tag{2.50}$$

This resembles a Gaussian solution with mean velocity, $B = U = \left(\frac{h_1}{H}\right)U_1 + \left(\frac{H-h_1}{H}\right)U_2$, and asymptotic dispersion coefficient, $A = K_x$. Chikwendu [18] determined these constants analytically by substituting γ back into (2.49) and, setting the coefficients of k^i to zero, for $i = 0, 1$ and 2. This confirmed that $B = U$ and yielded a final solution for the longitudinal dispersion coefficient,

$$K_x = \frac{(\frac{h_1}{H})^2(\frac{H-h_1}{H})^2(U_2-U_1)^2}{b} + \left(\frac{h_1}{H}\right)K_1 + \left(\frac{H-h_1}{H}\right)K_2. \tag{2.51}$$

2.6 The Method of Moments

In 1956, Aris [3] first applied moment-generating equations to show that some of the conditions on (2.41) could be relaxed. Moment-generating equations allow (2.41) to be expressed in terms of the spatial variance of the concentration distribution, which is of great practical use. The i^{th} spatial moment of a concentration distribution is

[3] See §2.7 for a discussion of the Fickian limit.

given by

$$M_i = \int_{-\infty}^{\infty} x^i c(x,t) dx. \tag{2.52}$$

The various moments provide useful information about the properties of a concentration distribution. For example:

$$M_0 = \text{constant} = \text{mass} \tag{2.53}$$

$$\frac{M_1}{M_0} = \chi(t) = \text{center of mass} \tag{2.54}$$

$$\frac{M_2}{M_0} - \chi^2 = \sigma_x(t)^2 = \text{spatial variance of the distribution} \tag{2.55}$$

$$\frac{M_3}{\sigma_x^3} = G(t) = \text{skewness coefficient} \tag{2.56}$$

$$\frac{M_4}{\sigma_x^2} = \kappa(t) = \text{kurtosis.} \tag{2.57}$$

The first three statistical quantities are fairly well known. However, the parameters containing higher-order moments are not so commonly understood. They are generally used to describe the deviation of a particular distribution from Gaussianity. The skewness coefficient provides a measure of the asymmetry of a concentration distribution [86]. A perfect Gaussian has zero skewness. A negative skewness coefficient ($G < 0$) indicates a distribution biased to the right (i.e., the peak is to the right of the center of mass) and a positive skewness coefficient indicates left bias. If temporal moments are used to define the skewness coefficient, positive skewness indicates bias to short times. The kurtosis of a distribution describes the sharpness of its peak [86]. Because comparisons are usually made to Gaussian distributions, which have a kurtosis of 3, the kurtosis "excess",

$$\kappa_e = \kappa - 3, \tag{2.58}$$

is a more commonly used parameter. $\kappa_e > 0$ indicates a high peak and is referred to as leptokurtic. $\kappa_e < 0$ represents a flatter distribution, termed platykurtic.

A useful application of the moment-generating equations relates to the 1-D advection-dispersion equation given by (2.41). First, we switch to a moving co-ordinate system that travels at the mean velocity U, i.e.,

$$\xi = x - Ut \qquad \text{and} \qquad \tau = t \tag{2.59}$$

(e.g., [33, pp. 83]). By the chain rule of calculus, we find that

$$\frac{\partial}{\partial x} = \frac{\partial \xi}{\partial x}\frac{\partial}{\partial \xi} + \frac{\partial \tau}{\partial x}\frac{\partial}{\partial \tau} = \frac{\partial}{\partial \xi} \tag{2.60}$$

$$\frac{\partial}{\partial t} = \frac{\partial \xi}{\partial t}\frac{\partial}{\partial \xi} + \frac{\partial \tau}{\partial t}\frac{\partial}{\partial \tau} = -U\frac{\partial}{\partial \xi} + \frac{\partial}{\partial \tau}. \tag{2.61}$$

In the new co-ordinate system, (2.41) then becomes

$$\frac{\partial C}{\partial \tau} = K_x \frac{\partial^2 C}{\partial \xi^2}. \tag{2.62}$$

Now, we multiply each of the terms by ξ^2 and integrate over $-\infty < \xi < \infty$ to obtain

$$\frac{\partial}{\partial \tau}\int_{-\infty}^{\infty} C\xi^2 \, d\xi = K_x \int_{-\infty}^{\infty} \frac{\partial^2 C}{\partial \xi^2}\xi^2 \, d\xi. \tag{2.63}$$

The right hand side of (2.63) can be integrated by parts [3] such that K_x can be expressed as

$$K_x = \frac{1}{2}\frac{\partial}{\partial \tau}\left[\frac{\int_{-\infty}^{\infty} C\xi^2 \, d\xi}{\int_{-\infty}^{\infty} C \, d\xi}\right], \tag{2.64}$$

which, by analogy with (2.55) is

$$K_x = \frac{1}{2}\frac{\partial \sigma_\xi^2}{\partial \tau}. \tag{2.65}$$

Note, the term in (2.55) representing the center of mass vanishes, since the new co-ordinate system travels with the center of mass. Thus, transformation back to our original co-ordinate system yields the spreading-rate of a tracer cloud in the

longitudinal direction,

$$K_x = \frac{1}{2}\frac{\partial \sigma_x^2}{\partial t}. \tag{2.66}$$

If the variance of a concentration distribution in a channel is known at any time, t_1, then the variance at any subsequent time, t_2, can be estimated from

$$\sigma_x(t_2)^2 = \sigma_x(t_1)^2 + 2K_x(t_2 - t_1) \tag{2.67}$$

[33, pp. 42], provided that $K_x \neq f(t)$. In the event of a time-varying dispersion coefficient, (2.67) is also true if $(t_2 - t_1) \rightarrow 0$.

2.7 Fickian Time Scales

Some time after the release of a mass of tracer into a channel, σ_x^2 increases linearly with time, such that K_x is constant, from (2.66). Prior to this time, known as the Fickian limit, differential advection will dominate and the rate of increase in the variance will not be linear. Non-linear growth of variance is indicative of anomalous diffusion [50, 127]. At short times, variance growth in unbounded unidirectional shear flows is generally *superdiffusive* (i.e., $\sigma_x^2 \sim t^a$, where $a > 1$). The characteristic rate of variance growth for vegetated channels will be discussed later in Chapter 4.

Fischer [32] proposed that a "reasonable practical criterion" for the onset of a Fickian regime is that the dimensionless time scale for cross-sectional mixing,

$$\tilde{t} = t\frac{\left[\frac{1}{H}\int_0^H D_z\, dz\right]}{H^2}, \tag{2.68}$$

should be greater than 0.4. This is the standard and most widely accepted criterion. However, Chatwin and Allen [16] point out that this bulk estimate ignores the effects of reduced mixing in dead zones. The depth average $D_{z,a} = \frac{1}{H}\int_0^H D_z\, dz$ in (2.68) underestimates the contribution from zones of significantly reduced diffusivity (this is a resolution issue, as discussed by Thacker [108]). Chatwin [15] proposed that $\tilde{t} = 1.0$ is the minimum time scale for an accurate analysis.

Practical considerations often limit the number of sampling stations in experimental tracer studies. And, concentration measurements at a single location dictate the approximation of (2.66) by $\frac{\sigma_x^2}{2\mu}$ (where μ is the mean travel time of a tracer cloud over a particular reach), which will remain an inaccurate estimator of K_x until some time after the onset of a Fickian regime. Therefore, a more stringent criterion may be required for experimental work.

2.7.1 Péclet Number

In §2.2.2, we showed that the Navier-Stokes equations could be non-dimensionalized to generate important dimensionless parameters such as the Reynolds' number and Froude number. Similar methodology can be applied to the equations of mass transport, such as (2.41), to yield interesting and useful results. Again, we begin by introducing dimensionless variables,

$$x^* = \frac{x}{L}, \qquad u^* = \frac{U}{V}, \qquad C^* = \frac{C}{C_{ref}}, \qquad t^* = \frac{tL}{V}.$$

Substitution into (2.41) then yields

$$\frac{VC_{ref}}{L}\left(\frac{\partial C^*}{\partial t^*} + u^*\frac{\partial C^*}{\partial x^*}\right) = \frac{K_x C_{ref}}{L^2}\left(\frac{\partial^2 C^*}{\partial x^{*2}}\right). \tag{2.69}$$

If we multiply (2.69) by (L/VC_{ref}), we obtain

$$\frac{\partial C^*}{\partial t^*} + u^*\frac{\partial C^*}{\partial x^*} = \frac{1}{Pe}\left(\frac{\partial^2 C^*}{\partial x^{*2}}\right), \tag{2.70}$$

where

$$Pe = \frac{VL}{K_x}. \tag{2.71}$$

Pe is a dimensionless dispersion Péclet number. It is the ratio of the time scale for dispersion (L^2/K_x) to the time scale for advection (L/V). From the magnitude of Pe, we can determine the relative importance of advection and dispersion. For example, $Pe \gg 1$ implies an advection-dominated system. As with the Reynolds'

number, appropriate choices of velocity and length scales are critical to the Péclet number's usefulness. K_x may also be replaced by a molecular or turbulent diffusion coefficient, depending on the relevant Péclet number. The Péclet number is the mass transport analogy to the Reynolds' number, which describes the relative importance of advection and diffusion of momentum.

2.8 Dispersion in Vegetated Channels

Diminished velocity and turbulence in the canopy region of a vegetated channel make it distinct from the overflowing water. We therefore propose a two-zone model for the vegetated channel with a division at the top of the canopy ($z = h$), as shown in Figure 2-5. Constant velocities, U_1 and U_2, are assumed for the lower and upper zones, respectively. K_1 and K_2 are the independent dispersion constants in the slow and fast zones, respectively. Scalar transport between the two layers is again characterized by the layer exchange coefficient, b. Thus, from (2.51), the longitudinal dispersion coefficient for a vegetated channel at large times is given by

$$K_x = \frac{(\frac{h}{H})^2(\frac{H-h}{H})^2(U_2 - U_1)^2}{b} + \left(\frac{h}{H}\right) K_1 + \left(\frac{H-h}{H}\right) K_2. \tag{2.72}$$

This form highlights three different processes that contribute to dispersion in channels containing submerged vegetation. The first term of (2.72) represents dispersion that arises from inefficient exchange between the fast zone ($h < z < H$) and the slow zone ($0 < z < h$). In other words, scalars trapped in the slow zone are held up relative to those in the fast zone, increasing the spread in the longitudinal direction. For simplicity, we assume

$$(U_2 - U_1) = \beta_1 \Delta U, \tag{2.73}$$

where β_1 is an $O(1)$ scale constant. We test this assumption in Chapter 4, where we will also show that $\Delta U \sim u_{*H}$. The second and third terms in (2.72) represent the dispersion in the canopy layer and the overflow layer, respectively.

By definition, the exchange coefficient, b, is the inverse of the time scale for vertical

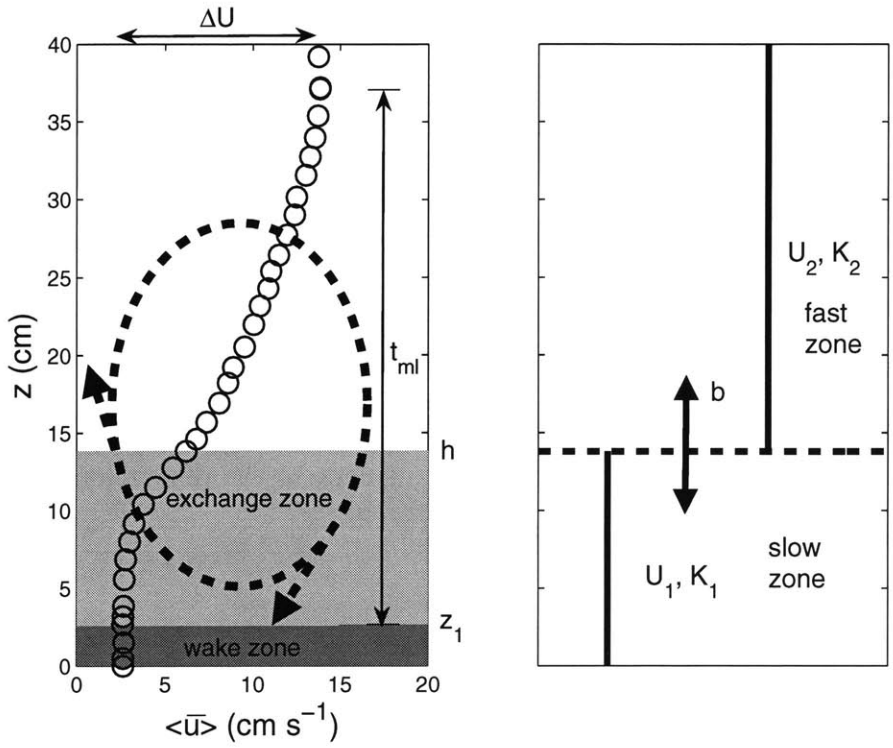

Figure 2-5: Slow zone model for a vegetated channel.

mixing across the two layers. Thus, we expect that

$$b^{-1} \simeq \frac{z_1^2}{D_w} + \frac{(h-z_1)}{k} + \frac{(H-h)^2}{\left[\frac{1}{H-h}\int_h^H D_z\, dz\right]}. \tag{2.74}$$

The first term in (2.74) represents the time scale for turbulent-diffusive transport across the wake zone. The second term represents the time scale for vortex-driven flushing of the exchange zone, for which Ghisalberti and Nepf [38] determined the exchange velocity, $k = \Delta U/40$. Finally, the last term in (2.74) is the time scale for transport across the fast zone. In the limit of a rough boundary layer where $H \gg h > z_1$, the first two terms of (2.74) are negligible and we are left with

$$b^{-1} \approx \frac{H^2}{\left[\frac{1}{H}\int_0^H D_z\, dz\right]} \tag{2.75}$$

which is the usual Fickian time scale for vertical mixing in an open channel, defined earlier in (2.68). As $H \rightarrow h$, and the vegetated region begins to occupy a significant

fraction of the flow depth, the boundary-layer approximation is less appropriate. Thus, for $H/h \sim O(1)$, mass transport across the unvegetated layer is so fast that the last term in (2.74) vanishes. §2.8.1 considers the regime where K-H vortices dominate exchange between the layers, such that the first and last terms on the right hand side of (2.74) are negligible. §2.8.2 deals with exchange that is limited by turbulent diffusion in the canopy, i.e., $b = D_w/z_1^2$.

The second term in (2.72) represents dispersion in the slow zone. K_1 is the dispersion coefficient that would be obtained for $0 < z < h$, if this region were detached from the flow above. If K_1 is assumed equivalent to the dispersion coefficient in an emergent canopy, it can be represented by

$$K_1 = K_{vs} + K_d, \tag{2.76}$$

where K_{vs} and K_d represent the in-canopy vertical shear [evaluated using (2.42)] and stem-scale contributions to dispersion, respectively. In sparse canopies ($ad < 0.1$), K_d results primarily from velocity heterogeneity due the presence of cylinders, and can be approximated by

$$K_d = \frac{1}{2} C_D^{1/3} U_1 d \tag{2.77}$$

[62, 122]. In denser canopies ($ad > 0.1$), stem-scale dispersion will be dominated by the trapping and release of mass within the boundary-layers and wakes of individual cylinders [122]. White and Nepf [122] found that the dispersion coefficient in an emergent random array of densely-packed cylinders is proportional to the volume of primary cylinder wakes, the wake residence times and the square of the velocity within the array. Thus, for a dense canopy,

$$K_d = \epsilon U_1^2 \bar{T}_{res}, \tag{2.78}$$

where

ϵ = the total fractional volume of primary cylinder wakes

and

$\bar{T}_{res}$ = the mean residence time within a primary wake.

As discussed in §2.2.2, the majority of field conditions exhibit stem-diameter Reynolds' numbers (Re_d) that are greater than 40, such that vortices are shed from the downstream side of the canopy elements [95, 122]. In this regime, engulfment by shed vortices, rather then diffusion, dominates the transport of scalars into and out of the primary wakes. Therefore, the residence time, $\bar{T}_{res}$, must be inversely proportional to the shedding frequency, f_s [122]. The shedding frequency for our canopy elements is given by $f_s = StU_1/d$, where the Strouhal number, St, is a function of Reynolds' number. For Reynolds' numbers of interest ($40 < Re_d < 10^4$), we find that $0.16<St<0.21$ [95, pp. 32], so we assume an approximate value of $St = 0.2$. It follows that $\bar{T}_{res} \sim 5\frac{d}{U_1}$. In addition, it is reasonable to assume that the fractional volume of primary wakes is proportional to the cylinder density [122], i.e., $\epsilon \sim ad$. Thus, we can approximate the stem-wake dispersion within a dense ($ad > 0.1$) canopy at $Re_d > 40$ by

$$K_d \cong 5adU_1 d. \tag{2.79}$$

Of course, this approximation will only hold in the Fickian limit, which is reached after all tracer particles have sampled a trapping wake at least once. The time to reach the Fickian limit is then given by

$$t \gg \frac{\bar{T}_{res}}{\epsilon} = \frac{5}{aU_1} \tag{2.80}$$

The third term in (2.72) contains K_2, which represents the longitudinal dispersion in the fast zone due to large-scale velocity shear in this region. Above the canopy, the velocity profile reverts to a logarithmic profile for $z > h$, with a virtual bottom boundary near $z = h$ [54, 74, 11]. Thus, Elder's simple analytical expression is expected to hold in the region $h < z < H$, yielding

$$K_2 = 5.9u_*(H - h) \tag{2.81}$$

where u_* is obtained from (2.22). Although the analysis of Nepf and Vivoni [74]

suggests that $z = z_1$ is a more appropriate choice for the lower limit to the logarithmic profile, simplicity and practical applicability of the model dictate the use of $z = h$.

It should be mentioned that (2.72) is consistent with established dispersion theory for boundary layers, as it reduces to (2.81), in the limit of $H/h \gg 1$. Similarly, in the limit of emergent vegetation ($H/h \rightarrow 1$), $K_x = K_1$.

2.8.1 Vortex-Driven Exchange

If $(z_1/h) \ll 1$, canopy exchange is driven by the K-H vortices, which penetrate almost to the bed. Scaling arguments and experiments by Ghisalberti and Nepf [38] show that vortex-driven exchange yields an exchange coefficient

$$b = \frac{\Delta U}{40h}. \tag{2.82}$$

Physical laboratory constraints, such as flume size, allowed a maximum experimental value of $z_1/h = 0.6$ to be obtained here, such that most of the experiments fall in this regime.

We can now begin to simplify the slow zone model, given by (2.72). When $z_1 \ll h$, the contribution of K_1 to the overall dispersion is expected to be small, so the second term in (2.72) is neglected for vortex-driven exchange. The exchange term is simplified by substitution of (2.82), (2.73) and the scaled constant $\beta_2 = \Delta U/u_{*H}$, to be determined by experiment. Finally, K_2 is replaced by the right hand side of (2.81), yielding

$$K_x = 40\beta_1^2\beta_2\left(\frac{h}{H}\right)^2\left(\frac{H-h}{H}\right)^2 hu_{*H} + 5.9\frac{(H-h)^2}{H}u_*. \tag{2.83}$$

For convenience, we combine the constants in the first term into a single parameter, β. Then, we divide through by $u_*(H-h)$ and rearrange, allowing us to obtain a nondimensional coefficient of longitudinal dispersion given by

$$\frac{K_x}{u_*(H-h)} = \beta\left(\frac{h}{H}\right)^3\left(\frac{H-h}{H}\right)^{1/2} + 5.9\left(\frac{H-h}{H}\right). \tag{2.84}$$

Alternatively, normalization by $u_{*H}H$ gives

$$\frac{K_x}{u_{*H}H} = \beta\left(\frac{h}{H}\right)^3\left(\frac{H-h}{H}\right)^2 + 5.9\left(\frac{H-h}{H}\right)^{5/2}, \tag{2.85}$$

which may be preferable for practical application.

2.8.2 Diffusion-Limited Exchange

In dense canopies $(z_1/h) \simeq 1$, and vortex penetration is so limited that in-canopy diffusion controls exchange between the layers, such that

$$b \simeq \frac{D_w}{h^2}. \tag{2.86}$$

This introduces the wake-zone vertical diffusivity, D_w. We assume that this is equivalent to the diffusivity in an emergent canopy and can be approximated by

$$D_w = \alpha\sqrt[3]{C_D a d}U_1 d, \tag{2.87}$$

where $\alpha = 0.1 - 0.2$ [62].

It is not obvious that stem-scale dispersion will be negligible in this regime. Initially therefore, we do not neglect K_1, as done in § 2.8.1. $(z_1/h) \to 1$ implies weak shear within a presumably dense canopy, such that K_{vs} can be neglected and $K_1 \simeq 5adU_1 d$ from (2.76) and (2.79).

Substituting these expressions for K_1 and D_w into (2.72) and applying similar simplifications to those in § 2.8.1, we obtain

$$\begin{aligned}\frac{K_x}{u_*(H-h)} =& \frac{1}{\alpha}\left(\frac{U_2-U_1}{u_{*H}}\right)^2 \frac{(\frac{h}{H})^4(H-h)^{1/2}H^{1/2}u_{*H}}{\sqrt[3]{C_D a d}U_1 d} \\ &+ \left(\frac{h}{H}\right)\frac{5ad^2U_1}{(H-h)u_*} \\ &+ 5.9(\frac{H-h}{H}).\end{aligned} \tag{2.88}$$

Following arguments made in §2.8.1, we expect $[(U_2 - U_1)/u_{*H}]$ to be constant.

From the momentum transport arguments that led to (2.23), we can deduce the following relationships between U_1 and the friction velocities:

$$\frac{u_{*H}}{U_1} = \left(\frac{C_D a h}{2}\right)^{1/2} \tag{2.89}$$

$$\frac{u_*}{U_1} = \left[\left(\frac{C_D a h}{2}\right)\left(\frac{H-h}{H}\right)\right]^{1/2}. \tag{2.90}$$

Substitution into (2.88) then yields

$$\begin{aligned}\frac{K_x}{u_*(H-h)} =& \zeta\left(\frac{h}{H}\right)^3\left(\frac{H-h}{H}\right)^{3/2}\left(\frac{h}{d}\right)^{4/3}(C_D a h)^{1/6} \\ &+ 5\sqrt{2}\left(\frac{h}{H}\right)^2\left(\frac{H}{H-h}\right)^{3/2}\left(\frac{d}{h}\right)\frac{(ad)}{(C_D a h)^{1/2}} \\ &+ 5.9\left(\frac{H-h}{H}\right)\end{aligned} \tag{2.91}$$

where

$$\zeta = \frac{1}{\sqrt{2}\alpha}\left(\frac{U_2 - U_1}{u_{*H}}\right)^2 \tag{2.92}$$

is a constant. Note that for $z_1/h \geq 0.9$ we would expect $C_D a h \geq 2$ from (2.29). Also, (2.91) only applies for dimensionless densities $ad > 0.1$ and $Re_d > 40$.

The ratio of the exchange coefficient in (2.82) to that given by (2.86) is

$$Pe_b = \frac{\Delta U/40h}{D_w/h^2} = \frac{\Delta U h}{40 D_w}. \tag{2.93}$$

This ratio has the form of a Péclet number and represents the relative magnitude of vertical advective (i.e., vortex-driven) and diffusive transport across the slow zone. Typically in the field, $\Delta U \sim O(1 - 10\text{cm/s})$, $h \sim O(1 - 100\text{cm})$, and $D_w \sim O(0.1\text{cm}^2/\text{s})$, such that $Pe_b > 1$. Thus, we anticipate that the exchange term is even more dominant in the diffusion-limited exchange regime. For consistency, it is then appropriate to neglect the slow-zone term in (2.91), as we did in §2.8.1 (although we recognize that in both regimes, K_1 will be important in the extreme limit of $H/h \to 1$). (2.91) then

simplifies to

$$\begin{aligned}\frac{K_x}{u_*(H-h)} =& \zeta\left(\frac{h}{H}\right)^3\left(\frac{H-h}{H}\right)^{3/2}\left(\frac{h}{d}\right)^{4/3}(C_D a h)^{1/6} \\ &+ 5.9\left(\frac{H-h}{H}\right),\end{aligned} \tag{2.94}$$

which is slightly preferable to (2.91), since it reduces the number of independent variables by one. Furthermore, there are no restrictions on ad or Re_d if (2.94) is used, in contrast to (2.91), which requires $ad > 0.1$ and $Re_d > 40$.

2.8.3 Random Walks

Often, it is not the concentration distribution of a scalar quantity that is of interest, but integrated properties such as residence time, or variance. Under such conditions, it is often prudent to adopt a Lagrangian approach, where transport processes are related directly to the behavior of individual particles [27]. This introduces the concept of a random walk, which can be used to provide an alternative to the Eulerian representation of mass transport given by (2.41).

Consider the hypothetical scenario of a single particle diffusing under the influence of stationary (not decaying in time), homogeneous turbulence. Although turbulent motion is not entirely random, it is sufficiently unpredictable at small scales that it can be viewed as such. The velocity of a particle undergoing the random walk is $\underline{u_p}(t)$, such that the position of the particle is given by $\underline{x_p}(t) = \int_0^t \underline{u_p}(t')dt'$ [55, pp. 571]. The variance of the particle's position is simply $\sigma_{x,p}^2 = \overline{\underline{x_p}(t)^2}$, where, for this section only, we use an overbar to denote an ensemble average instead of a temporal average. From (2.66), we can define a dispersion coefficient for the particle,

$$K_{x,p} = \frac{1}{2}\frac{\partial\left[\overline{\underline{x_p}(t)^2}\right]}{\partial t} = \overline{\underline{x_p}(t)\frac{\partial \underline{x_p}}{\partial t}}. \tag{2.95}$$

However, $\overline{\frac{\partial x_p}{\partial t}}$ is simply the particle's mean velocity, such that (2.95) becomes

$$K_{x,p} = \overline{\underline{u_p}(t) \int_0^t \underline{u_p}(t')dt'}. \tag{2.96}$$

Since turbulent velocities are correlated (a fact that gives rise to Reynolds' stress), we can define a normalized autocorrelation function that is a function of the time difference $\Im = t' - t$,

$$r(\Im) = \frac{\overline{\underline{u_p}(t)\underline{u_p}(t+\Im)}}{\overline{\underline{u_p}(t)^2}}. \tag{2.97}$$

Thus, (2.96) can be written as

$$K_{x,p} = \overline{\underline{u_p}(t)^2} \int_0^t r(\Im)d\Im. \tag{2.98}$$

This is a result of Taylor's (1921) theory (see e.g., [55, pp. 569]), which shows that the variance of particles in stationary, homogeneous turbulence increases linearly with time, after sufficient time has elapsed for the particles to lose memory of their initial velocities (or become uncorrelated). This time is known as the "Lagrangian time scale", $T_L = \int_0^t r(\Im)d\Im$. It should be obvious that this time scale is heuristically similar to the Fickian time scale that was discussed previously for an Eulerian framework, and much research has focused on relating the two time scales [52, 78]. The purpose of this exercise is to show that diffusion (and hence dispersion) can be approached from either an Eulerian or a Lagrangian perspective, and is analogous to a random walk.

The equation used to model transport of a particle as a random walk, is the Fokker-Planck equation,

$$\frac{\partial f}{\partial t} + \nabla\left(\underline{A}f\right) = \nabla^2\left(\frac{1}{2}\underline{\underline{B}}\underline{\underline{B}}^T f\right), \tag{2.99}$$

where $f(\underline{x}, t)$ is the probability density function of the particle's position, $\underline{A}$ is a vector of deterministic forces acting on the particle, and $\underline{\underline{B}}$ is a second order tensor (with transpose $\underline{\underline{B}}^T$) that characterizes the "random" forces due to turbulence [27, 75, 44]. A

time step, $\Delta t > T_L$, can be chosen such that the motions of a particle are uncorrelated in time. Then, (2.99) can be represented by the discrete Ito stochastic differential equation,

$$\Delta x = \underline{x}(t_i) - \underline{x}(t_{i-1}) = \underline{A}(\underline{x}(t_{i-1}), t_{i-1})\Delta t + \underline{\underline{B}}(\underline{x}(t_{i-1}), t_{i-1})R\sqrt{\Delta t} \tag{2.100}$$

[27], where R is a random number generated from a Gaussian probability distribution with zero mean and unit standard deviation [44]. (2.100) is an exact representation of (2.99) for $\Delta t \to 0$ and an infinite number of particles.

Now, for (2.99) to be equivalent to (2.41), we require

$$\begin{aligned} \underline{A} &= U \\ \underline{\underline{B}} &= \sqrt{2K_x} \\ f &= C, \end{aligned}$$

such that (2.100) becomes

$$\Delta x = U(\underline{x}(t_{i-1}), t_{i-1})\Delta t + R\sqrt{2K_x\Delta t} \tag{2.101}$$

The first term on the right hand side of (2.101) represents advection of the particles, and the second term represents longitudinal dispersion.

If we are interested in the dispersion of particles before full cross-sectional mixing is achieved, the sectionally averaged approach given by (2.101) is inappropriate. However, a similar analogy can be drawn between the Fokker-Planck and the 2-D (x and z) advective-diffusive equation. This generates additional deterministic terms such that the particle positions are given by[4]

$$\Delta x = \bar{u}\Delta t + \frac{dD_x}{dx}\Delta t + R\sqrt{2D_x\Delta t} \tag{2.102}$$

$$\Delta z = \bar{w}\Delta t + \frac{dD_z}{dz}\Delta t + R\sqrt{2D_z\Delta t}. \tag{2.103}$$

[4]For clarity, $\frac{d}{dt}$ is used to denote a total derivative here.

Utilizing Taylor's assumption that longitudinal diffusion is negligible, we can neglect terms containing D_x. We also assume that there is no mean flow in the vertical (i.e., $\bar{w} = 0$), yielding

$$\Delta x = \bar{u}\Delta t \tag{2.104}$$

$$\Delta z = \frac{dD_z}{dz}\Delta t + R\sqrt{2D_z\Delta t}. \tag{2.105}$$

In the absence of a gradient in the vertical diffusivity field, we see that (2.104) and (2.105) constitute transport of individual particles by longitudinal advection, with random vertical jumps superimposed to imitate transverse turbulent diffusion [119]. The attractiveness of this representation is illustrated by the fact that it concurs with Taylor's concept of longitudinal dispersion as a balance between differential advection and transverse diffusion.

In most situations there will be at least some gradient in the diffusivity field, such that the first term on the right hand side of (2.105) cannot be neglected. In the extreme case of a stepped D_z profile, $\frac{dD_z}{dz} \rightarrow \infty$ at the step, such that (2.105) breaks down. Thus, considerable care is necessary when using the random walk formulation close to boundaries and diffusivity interfaces [110]. This will be discussed in more detail in Chapter 3.

It is worth pointing out that the Lagrangian time scale for turbulent diffusion is likely to be much shorter than that for longitudinal dispersion. In other words, the time scales of turbulent fluctuations will be less than the time required for mixing across a channel cross-section. Thus, the constraint $\Delta t > T_L$ permits shorter time steps in (2.104) and (2.105) than in the cross-sectionally averaged example, since $T_L \sim t_{Fick} = 0.4H^2/D_{z,a}$ for (2.101).

Chapter 3

Materials and Methods

3.1 Experiments

Laboratory experiments were designed to evaluate the two-layer dispersion theory proposed for aquatic vegetation in Chapter 2. In particular, the experiments aimed to show the performance of the model across a broad range of vegetation densities, Reynolds' numbers and water depth-to-plant height ratios, corresponding to values observed in the field.

3.1.1 Laboratory Setup and Methods

Experiments were conducted in a 24-m-long x 38-cm-wide x 58-cm-deep, glass-walled recirculating flume (Figure 3-1). The flow rate in the flume was controlled by a Weinman 3G-30P14 pump, with a capacity that ranged from 600 cm^3/s to 15,000 cm^3/s. A Signet flow gauge, with ± 200 cm^3/s accuracy, provided estimates of flow rate. A number of measures were taken to ensure smooth inlet conditions. A dense, 0.5-m-long array of emergent wooden dowels was used to break up turbulence. A mat of rubberized coconut fiber extended throughout the cross-section of the flume, to further dampen the turbulent inlet jet. Honeycomb flow-straighteners eliminated swirl, providing unidirectional flow in the downstream direction.

The model plant canopy consisted of maple cylinders (diameter, $d = 6$mm), in-

Table 3.1: Summary of experimental conditions.

Run	Q, x 10^{-2} cm^3 s^{-1}	h, cm	H, cm	a, cm^{-1}	d, cm
A	48	14.0	46.7	0.025	0.6
B	17	14.0	46.7	0.025	0.6
C	74	14.0	46.7	0.034	0.6
D	48	14.0	46.7	0.034	0.6
E	143	14.0	46.7	0.040	0.6
G	48	14.0	46.7	0.040	0.6
H	143	14.0	46.7	0.080	0.6
I	94	14.0	46.7	0.080	0.6
A6	17	7.0	29.8	0.025	0.6
B6	94	7.0	29.8	0.025	0.6
C6	48	7.0	29.8	0.025	0.6
A1	17	7.0	23.6	0.025	0.6
B1	94	7.0	23.6	0.025	0.6
C1	48	7.0	23.6	0.025	0.6
A2	17	7.0	14.0	0.025	0.6
B2	94	7.0	14.0	0.025	0.6
C2	48	7.0	14.0	0.025	0.6
A3	17	7.0	10.5	0.025	0.6
C3	48	7.0	10.5	0.025	0.6
A5	17	7.0	8.8	0.025	0.6
C5	48	7.0	8.8	0.025	0.6
C6D	48	7.0	29.8	0.080	0.6
C2D	48	7.0	14.0	0.080	0.6
A2D	17	7.0	14.0	0.080	0.6
A3D	17	7.0	10.5	0.080	0.6
A4	17	7.0	5.0	0.025	0.6
X4D	17	7.0	5.0	0.080	0.6

serted in a random configuration into perforated Plexiglas boards, which covered the entire length of the flume (see Figure 3-2). Duct tape was fixed to the underside of the boards, so that a uniform depth of penetration could be achieved. Plastic cable ties were used to secure the boards to each other. The canopy density was varied between $ad = 0.015$ and $ad = 0.048$, within a range representative of dense aquatic meadows, as cited in [37]. Two canopy heights were employed, 7 cm and 14 cm.

Preliminary velocity profiles were taken by three acoustic Doppler velocimeter (ADV) probes at different transverse locations in the flume. The results confirmed that a single profile at mid-width approximated the lateral mean to within 10 %, provided that the probe was not positioned directly downstream of a dowel. Velocity profiles for runs A-I (see Table 3.1) were taken from laterally-averaged ADV measurements in [37]. For the remaining runs, velocity measurements were taken by a two-dimensional (2-D) laser Doppler velocimeter (LDV). This technology is described in §3.1.2. Vertical profiles, taken at mid-width in the flume, consisted of five-minute records at spacings of between 0.5 cm and 2 cm, depending on the water depth and the precision required. Previous testing by [34] and [61] showed that this record length was sufficiently long to obtain acceptable mean velocity and turbulence statistics. All measurements were taken sufficiently far downstream of the start of the canopy such that the flow was fully developed (i.e., $\partial/\partial x = 0$). The 60 mm-diameter LDV probe was positioned on an automated aluminium traverse outside the flume and the beams were directed perpendicularly towards through the glass sidewall. The refraction of the beams as they passed through the glass was taken into account when positioning the probe. Part of the attractiveness of the LDV system was that it was non-invasive, thereby preventing artificial disturbance of the velocity field. In addition, the positioning of the probe outside the flume allowed its movements to be motorized and controlled by Compumotor motion control software. The traverse system, which was connected to a processor, allowed precise maneuvering in the vertical and horizontal planes. A horizontal segment (approximately 10 cm wide) of dowels had to be removed to prevent obstruction of the laser beams as they entered the flume. However, since this segment length was on the order of the dowel spacing, it is unlikely that

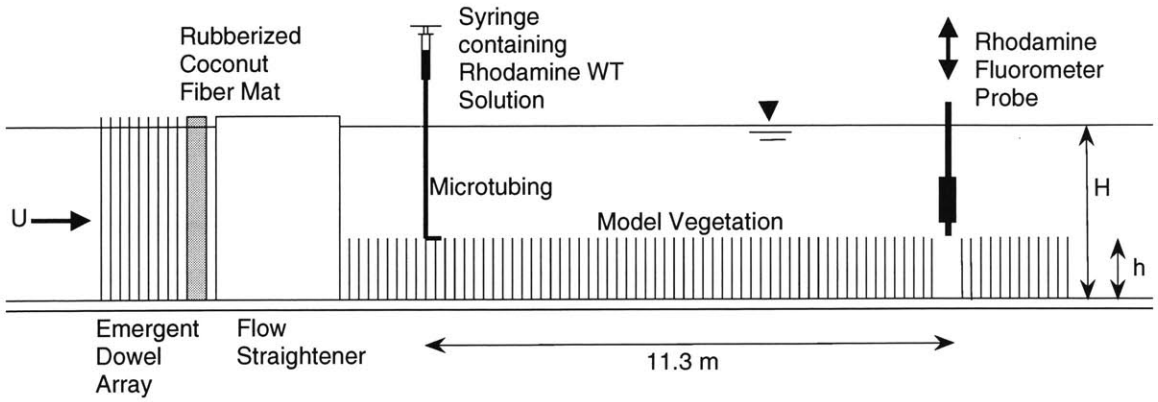

Figure 3-1: Experimental setup (not shown to scale).

Figure 3-2: Photographs of model canopy and flume setup ($h = 7$ cm and $ad = 0.048$).

the mean velocity and turbulent statistics were significantly affected [46, 37]. To help maintain optimal sampling rates, the flume was lightly seeded with 10 μm particles. Since the data rate is a function of the number of particles impinging on the fringe pattern, better sampling rates were achieved under higher velocity conditions. Data rates ranged from $\sim$ 5 Hz for slow flow near the bottom boundary to $>$ 100 Hz above the canopy in fast-flowing conditions. Efforts were made to optimize the voltage, validation and bandwidth settings on the FVA unit to achieve optimal data rates (see e.g., [34]).

Twenty-seven different flow scenarios were investigated (Table 3.1), with varying values of discharge, Q, and canopy density, ad. The water depth-to-canopy height ratio, H/h, was also varied between 1 and 4.25 to model vegetation conditions ranging from emergent to thoroughly submerged. The water-depth Reynolds number ($Re_H = UH/\nu$) was between $\sim$ 1,900 and 41,000 for the experiments. These values of Re_H are consistent with those observed in natural vegetated channels [58]. The stem-diameter Reynolds number ($Re_d = U_1 d/\nu$) defines dispersion in the slow zone, and values within the experimental range $Re_d \sim$ 20 - 580 correspond well to field conditions.

Tracer experiments were conducted by releasing a small pulse of fluorescent dye at the top of the canopy, 6 m downstream of the leading edge. This longitudinal position was observed to be well within the region of fully developed flow, determined by measured velocity profiles. The tracer consisted of a mixture of Rhodamine WT dye and isopropyl alcohol, with the latter added to render the solute neutrally buoyant in the flume. The dye was injected manually with a 60-ml syringe, through micro-tubing (1-mm inner diameter) that was glued to the top of a dowel at mid-width and oriented parallel to the mean flow. The micro-tubing extended approximately 2 cm downstream of the dowel, such that tracer was not introduced directly into the primary wake. Care was taken to match the injection speed with the local water velocity, to limit near-field mixing effects. The duration of the injection was minimized, to mimic a pulse, and subsequent leakage of tracer into the flow was eliminated by withdrawal of the syringe.

The depth-averaged concentration of dye was measured as a function of time, at

a location 11.3 m downstream of the injection point. This was done using a Seapoint Sensors Rhodamine fluorometer (see §3.1.2). In all cases, the travel time of the tracer cloud from its point of injection to the probe was much greater than the time taken to introduce the dye mixture. This confirmed that the initial condition closely resembled an instantaneous release. The fluorometer was mounted at mid-width in the flume on a pulley system that allowed smooth, precise maneuvering in the vertical plane (see Figure 3-3). As the tracer cloud advected by, the fluorometer was repeatedly raised and dropped at timed intervals, so that the entire water depth was sampled. The vertical transverse time was sufficiently short, compared to the time scale of tracer plume passage, that the vertical profile can be considered an instantaneous snapshot, and used directly to estimate the instantaneous depth-averaged concentration, C. Experimental runs were terminated when it was evident that tracer mass in the leading edge of the cloud had fully recirculated around the flume. This was indicated by steadily growing, elevated fluorometer voltage readings that greatly exceeded the normal fluctuations observed as the tail of the plume passed the measurement point for the first time. The recirculation times determined in this manner correlated well with rough estimates made using flow gauge and depth measurements. Each tracer experiment was repeated five times, to reduce random error.

For two runs (A4 and X4D), the dowels pierced the free surface (i.e., representing an emergent canopy). Because the dowels were only 7 cm long, the maximum flow depth that could be achieved was 5 cm. Since the dowels pierced the free surface, the dye injection was carried out at mid-depth ($z = 2.5$ cm), instead of at the top of the canopy. A short time after the recirculating pump was switched on, a pronounced free-surface oscillation was observed. The waves appeared to travel in the longitudinal and transverse directions, with periods of about 0.5 s and amplitudes of about 0.5 cm. The wavelength in the longitudinal direction was estimated to be ~ 1 m. It was postulated that the motion was a manifestation of vortex interaction due to periodic shedding from the downstream edge of the dowels, and resonant with a shallow water wave mode in the flume.

Figure 3-3: Photograph of fluorometer and pulley setup.

3.1.2 Instrumentation

Rhodamine WT Fluorometer

The Seapoint Sensors fluorometer uses modulated green LEDs to emit light, which is filtered to a narrow band, of wavelength around 540 nm. This wavelength excites Rhodamine WT particles that are passing through the opening in the fluorometer. The Rhodamine WT particles then re-emit fluorescent light at a different wavelength (about 610 nm). The intensity of the re-emitted light, which is detected by a silicon photodiode in the fluorometer, is proportional to the number of Rhodamine WT particles present (and is thus proportional to the dye concentration). This is output in the form of a low voltage signal.

The probe used in the experiments had a diameter of 6.4 cm and was 13 cm long. It had a sampling rate of 8 Hz and interfaced with a personal computer through an Ocean Sensors OS200 CTD. The "auto4.exe" program provided with the fluorometer

software was executed in MS-DOS and stored data in ASCII ("*.asc") files. Crucial output for this study included the recording time and corresponding voltage readings, which were tabulated in the ASCII files. These files were later imported to MATLAB [109] for processing.

The fluorometer was calibrated by Aaron Chow of Massachusetts Institute of Technology. The results were used to determine a relationship between voltage, V_c, and Rhodamine WT concentration, c, namely

$$c = 10.0^{1.54\log_{10}(V_c+0.03)} + 1.5. \qquad [\mu g/L \text{ if } V \text{ is in volts.}] \tag{3.1}$$

This relationship was only valid in the range $0.5\mu g/L < c < 320\mu g/L$, so this was taken into account when preparing the Rhodamine WT solutions. Trial and error was used to determine the initial concentrations of dye required to produce concentrations within the calibration limits at the point of measurement.

For a small number of the voltage-time records, pronounced voltage spikes (anomalously high or low readings) were observed at discrete points. Eventually, it was established that the reason for this was a faulty connection between the CTD and the personal computer. Normal behavior resumed when this was addressed. In any event, except for the small number of spikes (the durations of which were always less than a second), the records were consistent with other data. Therefore, a MATLAB code was written to remove anomalously high or low values (see Appendix B), such that the adjusted records could be deemed useful.

Laser Doppler Velocimeter (LDV)

The principle of the LDV is based on the phenomenon known as Doppler shift, named after the mathematician, Christian Doppler. He made the discovery that the wavelength of light emitted from stars appeared to be different, depending on whether they were moving towards or away from the observer.

Velocity measurements were made by a 300 mW blue-green argon-ion laser, used in conjunction with a Dantec 58N40 flow velocity analyzer (FVA) unit. Comprehensive

reviews of laser Doppler anemometry technology are given by [9] and [34]. However, the basic operational characteristics of the system used here are as follows. Light from the laser was split into two beams and a Bragg cell was used to shift one of the beams by 40 MHz [5]. Both the direct and the shifted beam were then split again into two beams of wavelength 488 nm and 514.5 nm, one for each velocity component (x and z). The four beams were focused onto fibre optic cables which eventually led to the probe, where they exited at 38-mm spacing (vertical and horizontal). The beams were focused to a single point by an optic lens with a focal length of 310 mm. The intersecting beams formed an ellipsoid sampling volume (of dimensions 74 μm $\times$ 610 μm), a geometry that was a result of the Gaussian light intensity profiles of the laser beams [5]. Particles flowing through this volume scattered the laser light and returned it to the lens, where it was fed back through fibre optic cables to a photomultiplier and a BSA F50 processor [5]. The intensity of the scattered light pulsated with a frequency proportional to the velocity of the particles moving through the intersection of the beams (known as the "fringe"). The purpose of the frequency shift induced by the Bragg cell is to resolve the directionality of the velocity components (or more specifically, to distinguish between positive and negative velocity readings).

Mean velocity measurements using the LDV were accurate to $\pm$1.4mm/s according to a previous analysis by [128]. Since only one vertical profile was taken for each run, this error was expected to be negligible in comparison with errors due to spatial variability in the mean velocity, particularly within the canopy region. The vertical separation of the beams exiting the probe prevented velocity measurements from being taken within 1 cm of the flume bed and free surface.

Acoustic Doppler Velocimeter (ADV)

Initially, a number of velocity profiles were taken using SonTek 3-D ADV probes. However, the configuration of the ADV probe was such that the top 4.5 cm of the flow depth could not be sampled[1]. Thus, velocity measurements using the ADV were

[1]The probe tip must be fully immersed in water to function, and the sampling volume is approximately 4.5 cm below the tip.

abandoned, in favor of the non-intrusive LDV. For that reason, a description of the ADV system is not included here, except to say that it is based on a similar principle as the LDV, the primary difference being that sound waves are transmitted by the probe and reflected by particles, instead of laser light. A thorough explanation of acoustic Doppler velocimetry is given by [35] and [34], and a comprehensive evaluation of accuracy is given by [117].

3.1.3 Data Analysis

The tabular ASCII files containing fluorometer output were processed in MATLAB, as mentioned in §3.1.2. MATLAB code was written to read in the columns of data (see Appendix B). The voltage-concentration relationship given by (3.1) was then used to develop curves of concentration versus time.

After subtracting out the background concentration (taken to be the mean of the first four values in the record), the temporal variance, ${\sigma_t}^2$, of the measured concentration-time distributions was calculated using the method of moments [3],

$${\sigma_t}^2 = \frac{M_2}{M_0} - \left(\frac{M_1}{M_0}\right)^2. \tag{3.2}$$

Here, M_i denotes the i^{th} *temporal* moment of the distribution, obtained from

$$M_i = \int_{-\infty}^{\infty} t^i c(t) dt. \tag{3.3}$$

The velocity, U_c, of the tracer center of mass can be expressed as

$$U_c = X/\mu \tag{3.4}$$

where X is the distance between the point of injection and the fluorometer (11.3 m), and μ, the mean arrival time of the solute cloud, is obtained from the relationship

$$\mu = M_1/M_0. \tag{3.5}$$

Combining results from five realizations of each experiment yielded ensemble-averaged values of U_c and σ_t. The "frozen cloud" approximation [33, pp. 137] was then applied, meaning that the tracer mass was assumed not to disperse appreciably as it passed the fluorometer. The spatial variance could then be inferred from the mean Lagrangian velocity of the tracer,

$$\sigma_x^2 = \sigma_t^2 U_c^2 \tag{3.6}$$

and longitudinal dispersion coefficients were estimated from $K_x = \frac{\sigma_x^2}{2\mu}$, an approximation of (2.66). Here, it was assumed *a priori* that X was sufficiently large, in all cases, for the solute to have reached a Fickian dispersive regime.

To allow comparison of the concentration-time curves, the time and concentration axes were normalized by μ and M_0 (the total recovered mass of the solute), respectively. Normalization of the concentration data eliminated, so far as was possible, non-uniformities across realizations caused by slight differences in the masses of tracer injected [122].

The LDV velocity data was output directly to text ("*.txt") files as a continuous (in the sense that vertical location was ignored) record. The files were imported to MATLAB for processing. A MATLAB code written by Brian L. White was modified and used to discretize the record by vertical measurement location. Velocity readings that were taken while the probe was being moved from one vertical position to the next were removed. This was done by considering a window of 30 data points around multiples of the duration of individual records (i.e., at 300 s, 600 s, 900 s, etc.). Anomalously high velocity data, corresponding to movements of the probe, was discarded. The same MATLAB code was then used to provide profiles of mean velocity (in x and z) and Reynolds' stress and output the data to text files for storage. The data was imported into Microsoft Excel for analysis and presentation.

Diffusivity profiles were required for input to the random walk particle-tracking model (described later in §3.2). Experimentally determined D_z profiles were available for runs A-I from [38]. For the remaining runs, vertical diffusivity profiles were estimated from mean flow and turbulence measurements. Within the wake zone

(i.e., $z < z_1$), D_z was assumed to take a constant value, obtained from Figure 7 of [73]. The extremities of the shear layer, $z = z_1$ and $z = (z_1 + t_{ml})$, were arbitrarily defined by the vertical locations where the Reynolds' stress was observed to go to zero. In cases where $-\overline{u'w'}$ did not reach a zero value, the uncertainty associated with the LDV measurements defined the lower limit of Reynolds' stress within the shear layer. If the Reynolds' stress did not drop below these levels in the range $h < z < H$, it was assumed that $(z_1 + t_{ml}) = H$. Similarly, $z_1 = 0$ was assumed if non-zero Reynolds' stress persisted to the bed. In the lower 80% of the shear layer (i.e., $z_1 < z < [z_1 + 0.8t_{ml}]$), the diffusivity was computed from (2.37), after ν_{tz} was determined from (2.36). The turbulent Schmidt number, Sc_t, was taken to be 0.49 in accordance with observations for vegetated shear layers (see §2.3.2). In the upper water column (specifically, $z > [z_1 + 0.8t_{ml}]$), where weak shear made (2.36) unstable, we assume $D_z = 0.013\Delta U t_{ml}$ as in [38].

In general, the surface slope was too small to be practically measured using displacement transducers. Therefore, S was estimated using equation (10) in Ghisalberti and Nepf [37], i.e.,

$$S = \frac{1}{g}\left(\frac{\partial \overline{u'w'}}{\partial z}\right), \qquad h < z < (z_1 + t_{ml}). \tag{3.7}$$

Estimates of the bulk drag coefficient, C_D, were then obtained from (2.23), i.e.,

$$C_D = \frac{2gSH}{a\int_0^h \langle \bar{u} \rangle \, dz}. \tag{3.8}$$

3.2 Numerical Model

Results from the tracer experiments suggested that the Fickian limit was *not* reached in all of the runs (as previously assumed in §3.1.3), due to the constraint imposed by the length of the flume. For this reason, and to investigate the error introduced by the approximation of (2.66), a random walk particle-tracking model (RWPT) was developed.

3.2.1 Model Description

The starting point was a two-dimensional (x and z) particle-tracking model for flow in an open channel. This was developed by Brian L. White, at Massachusetts Institute of Technology, in the Netlogo programming environment [124]. The model was modified to incorporate the hydrodynamics of vegetated flows, which differ significantly from those of bare open channels.

First, a rectangular Eulerian grid was initialized, the elements of which were assigned longitudinal flow velocities $\bar{u}(z)$, and vertical diffusivities, $D_z(z)$ (vertical velocities were assumed negligible). In the Netlogo programming language, the immobile elements of the domain are referred to as "patches". The particles that are tracked as they move throughout the grid are "turtles" which can be introduced to this domain as required, and can occupy any position within a patch. The number of particles per unit area of the domain essentially represents the concentration of a tracer or pollutant.

In the RWPT model, particles are advected with the mean longitudinal velocity field [according to Equation (2.104)] and random jumps in the vertical simulate turbulent diffusion [Equation (2.105)]. Longitudinal diffusion is neglected, as it is small compared to longitudinal dispersion.

For simplicity, a stepped $D_z(z)$ profile was used in the model to represent actual diffusivity conditions. For $z < z_1$, D_z was assumed to have a constant value, obtained from Figure 7 of [73]. The depth average vertical diffusivity for the shear layer, $D_{z,sl}$, was calculated from the D_z profiles estimated in §3.1.3, specifically

$$D_{z,sl} = \frac{1}{H - z_1} \int_{z_1}^{H} D_z \, dz \tag{3.9}$$

and was input to the model for $z > z_1$.

3.2.2 Corrections for Discontinuous Diffusivity Profiles

In RWPT models, a discontinuous diffusivity profile can result in artificial particle accumulation in regions of low diffusivity [110, 44, 94]. In fact, to correctly apply

(2.104) and (2.105), $D_z(z)$ and $D'_z(z)$ should be continuous and differentiable [94]. In our model, the first term in (2.105) vanishes over most of the domain. However, the diffusivity gradient is undefined at the bottom boundary, the free surface, and the step in the diffusivity profile ($z = z_1$). The first two issues were dealt with by implementing a fully reflecting boundary condition. A different correction was required at $z = z_1$, where the diffusivity discontinuity interface was treated as a semi-reflecting boundary (see e.g., [94]).

Zero Flux Boundaries

Boundaries in random walk models, such as at the bed or the free surface, may be treated as absorbing or reflecting [94]. Here, we adopted the latter approach, such that the new vertical position of a particle encountering a boundary was given by

$$\underline{z}(t_i) = \underline{z}(t_{i-1}) + \Delta z \rightarrow \begin{cases} -\underline{z}(t_i) & \text{, if } \underline{z}(t_i) < 0 \quad \text{(bottom boundary)} \\ 2H - \underline{z}(t_i) & \text{, if } \underline{z}(t_i) > H \quad \text{(free surface)} \end{cases}$$

(see Figure 3-4).

Diffusivity Step at $z = z_1$

There are two reasons why discontinuities in the vertical diffusivity profile result in particle accumulation in the region of lower vertical diffusivity: (i) More particles approach the discontinuity from a region of high diffusivity than from a region of low diffusivity, since the distances traveled by individual particles are proportional to the local diffusivity [i.e., $\Delta z \sim D_z^{1/2}$ from (2.105)], and (ii), particles that cross the discontinuity move at velocities[2] corresponding to the local diffusivity at t_{i-1} (i.e., the velocity of an individual particle is not updated in response to large changes in the local diffusivity field, which it experiences at the instant it crosses the discontinuity). The latter reason implies that a correction must be made to ensure that particle

[2]Strictly speaking, particle "velocities" are dependent on the time step, Δt and therefore have no physical meaning [110]. However, based on (2.105), it is clear that we can regard the particles as having velocities governed by a Gaussian distribution [110].

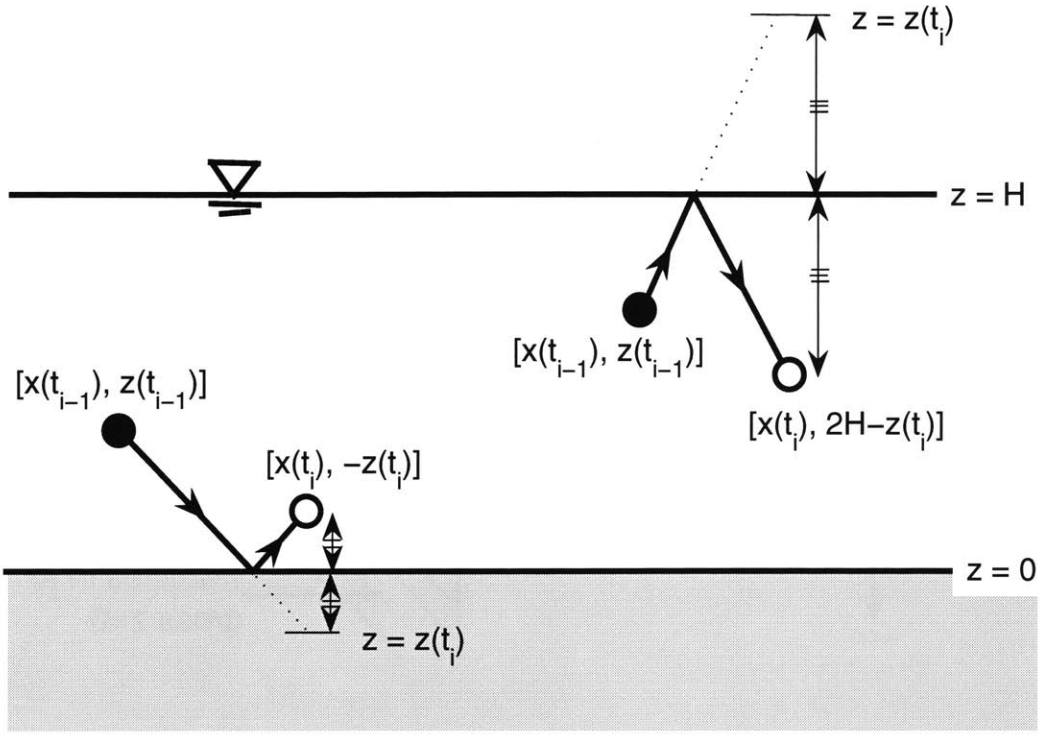

Figure 3-4: RWPT model treatment of the no flux boundaries. (a) The bottom boundary condition. (b) The free surface boundary condition.

velocities are representative of the instantaneous local diffusivity field. From here on, the terms "interface" and "discontinuity" will be used to describe the plane at $z = z_1$ where the jump in diffusivity occurs.

A simple criterion to show whether diffusivity interfaces are implemented correctly in a random walk model is that a uniform distribution of particles should remain uniform with time [110]. Thus, "mass" flux of particles in the vertical must be conserved, on average (statistically speaking). Applying this concept, we first imagine a horizontal slice of infinitesimal thickness δz, located at $z = z_o$ in an infinite domain. The domain contains a well-mixed concentration of particles, c_p (see Figure 3-5). If all of the particles were to diffuse out of the slice in a single time step, Δt, we could

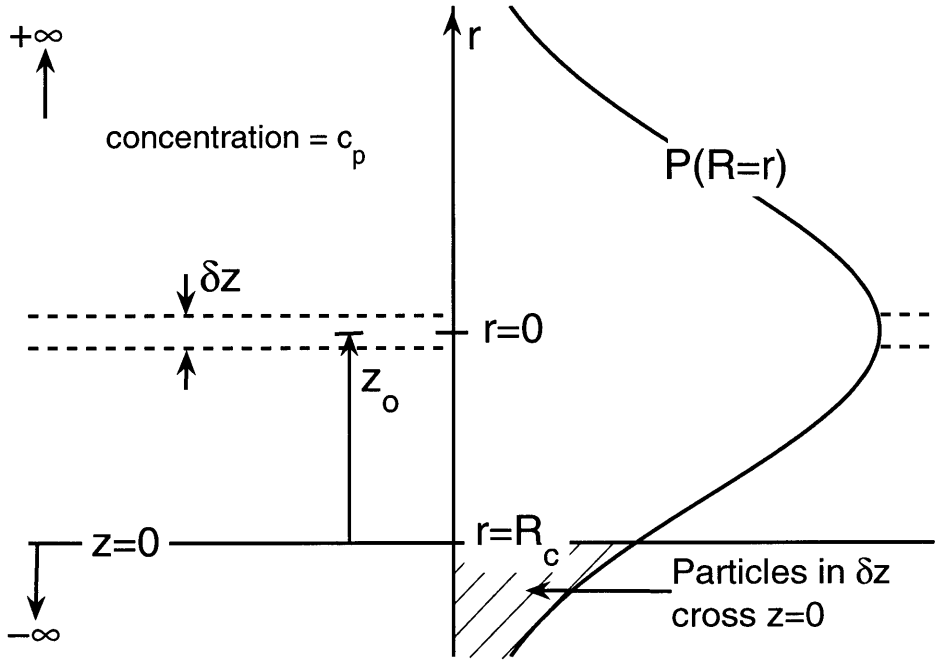

Figure 3-5: The probability distribution of particles crossing $z = 0$, for a slice of particles in an infinite, well-mixed domain.

define the flux per unit area as

$$\dot{m}_s = \frac{c_p\, \delta z}{\Delta t}. \tag{3.10}$$

However, many of the particles may not leave the slice during a single time step, since the vertical distance they travel is governed by a probability distribution [see Equation (2.105)]. If $P(-z_o \geq \Delta z)$ is the probability of a particle originating in the slice at $z = z_o$ crossing $z = 0$, we can then define the flux per area of particles from the slice across $z = 0$ by

$$\dot{m}_{s,0} = \frac{c_p\, \delta z}{\Delta t} P(-z_o \geq \Delta z). \tag{3.11}$$

If we integrate (3.11) over all slices in the range $0 < z < \infty$, we obtain an expression for the flux per area of particles across $z = 0$ from the region $z > 0$ for a single time step:

$$\dot{m} = \frac{c_p}{\Delta t} \int_{z_o=0}^{\infty} P(-z_o \geq \Delta z)\, dz_o, \tag{3.12}$$

or the number of particles per unit area that cross the boundary,

$$N^+ = c_p \int_{z_o=0}^{\infty} P(-z_o \geq \Delta z)\, dz_o. \tag{3.13}$$

From (2.105), it is clear that $P(-z_o \geq \Delta z) = f(R)$ is governed by a Gaussian probability distribution with zero mean and unit standard deviation. Specifically, it implies that whenever R is less than some critical (negative) value, R_c, for a given particle at a particular location in $z > 0$, the particle will cross $z = 0$ (Figure 3-5). R_c can be determined by imposing $\Delta_z = -z_o$ on Equation (2.105), yielding

$$R_c = \frac{-z_o}{\sqrt{2D_z^+ \Delta t}}, \tag{3.14}$$

where D_z^+ is the constant vertical diffusivity in $z > 0$. Therefore, we can integrate the Gaussian probability distribution from negative infinity to R_c, to determine $P(-z_o \geq \Delta z)$, such that (3.13) becomes

$$N^+ = \frac{c_p}{\sqrt{2\pi}} \int_{z_o=0}^{\infty} \int_{R=-\infty}^{R_c} e^{-R^2/2}\, dR\, dz_o. \tag{3.15}$$

If we evaluate this integral and ignore higher order corrections due the fact that real flows will not be unbounded, we arrive at the simple expression,

$$N^+ = c_p \left(\frac{D_z^+ \Delta t}{\pi} \right)^{1/2} \tag{3.16}$$

(Peter Israelsson, personal correspondence). Even if the flow is bounded at $z = Z_B$, (3.16) will remain accurate provided that $Z_B \gg \sqrt{2D_z^+ \Delta t}$. A small enough time step can usually be chosen such that this is the case. Shifting our focus back to the infinite domain, we can derive an expression similar to (3.16) for the number of particles (N^-) that cross $z = 0$ from the region $z < 0$, such that the ratio of the fluxes from either side is

$$\varphi = \frac{N^-}{N^+} = \left(\frac{D_z^-}{D_z^+} \right)^{1/2}. \tag{3.17}$$

Thus, it is clear that if no corrections are applied, particle fluxes will not be con-

served at a step change in diffusivity, as required. If $D_z^- < D_z^+$ (i.e., $\varphi < 1$), excess particle accumulation will occur in $z < 0$. To avoid this artifact of the random walk formulation, $(1-\varphi)N^+$ particles approaching $z = 0$ from $z > 0$ need to be prevented from entering $z < 0$. Since [110] points out that a solid boundary is simply a step discontinuity in the diffusivity profile, a similar treatment to the one employed for zero flux boundaries will be applied here to account for internal discontinuities in the diffusivity field. In other words, the diffusivity interface will be treated as a semi-reflecting boundary, with particles from the zone of highest diffusivity being reflected to conserve flux.

The semi-reflecting boundary at $z = z_1$ is implemented by the following procedure. First, any particle in the region $z > z_1$ for which $[\underline{z}(t_{i-1}) + \Delta z] < z_1$, is assigned a randomly generated number, $0 \leq R_d \leq 1$, from a uniform probability distribution. The new vertical position of the particle is then given by

$$\underline{z}(t_i) = \underline{z}(t_{i-1}) + \Delta z \rightarrow \begin{cases} 2z_1 - \underline{z}(t_i) & \text{, if } R_d < 1-\varphi \quad \text{(reflection)} \\ \underline{z}(t_i) & \text{, if } R_d > 1-\varphi \quad \text{(transmission).} \end{cases}$$

$\underline{z}(t_i)$ is not modified for particles in the region $z < z_1$, since all particles with $\Delta z > [z_1 - \underline{z}(t_{i-1})]$ are required to cross the interface from the zone of lower diffusivity.

This addresses the problem of conserving flux at a diffusivity interface. However, as previously mentioned, another problem is that the "velocity" of a particle transmitted from $z > z_1$ to $z < z_1$ (and vice versa) does not change instantaneously upon crossing of the interface. Corrections for this can be implemented in a number of different ways, some of which involve applying different time steps in the regions $z > z_1$ and $z < z_1$ (Israelsson, personal communication). However, the method chosen here is to perform an adjustment midway through the time step.

If a particle is to be transmitted through the diffusivity discontinuity, the time

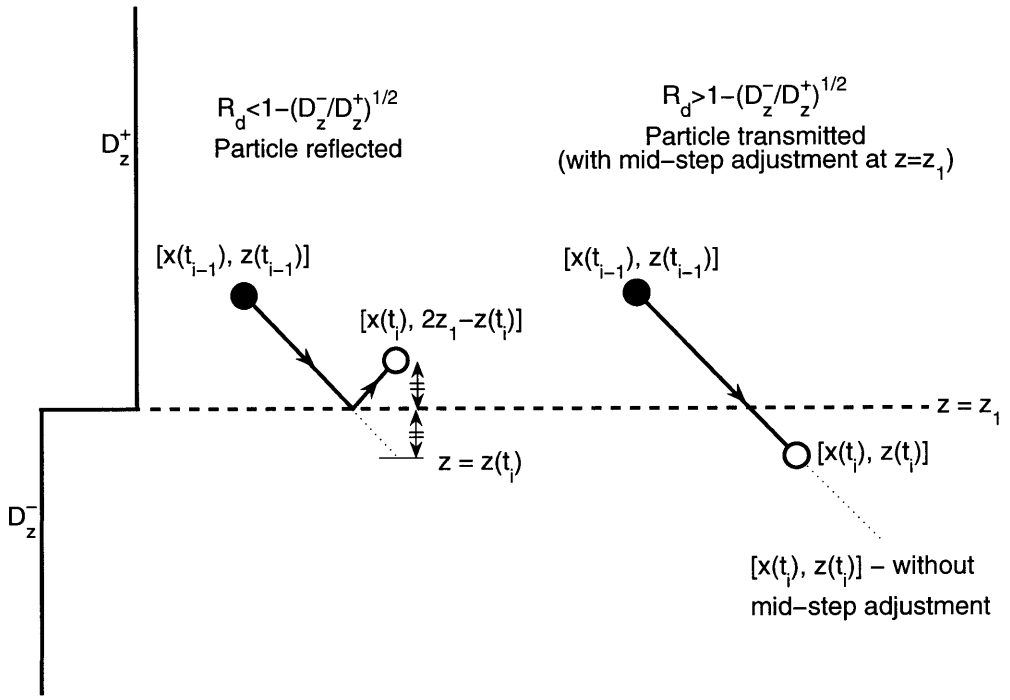

Figure 3-6: Corrections to particle positions at a diffusivity discontinuity.

step is split into two components

$$\Delta t^+ = \frac{z_1 - \underline{z}(t_{i-1})}{w^+} \tag{3.18}$$

$$\Delta t^- = \Delta t - \Delta t^+ = \frac{\underline{z}(t_i) - z_1}{w^-}, \tag{3.19}$$

where w^+ and w^- are the particle's "velocities" in the regions $z > z_1$ and $z < z_1$, respectively, and are given by

$$w^+ = \frac{R\sqrt{2D_z^+ \Delta t}}{\Delta t} \tag{3.20}$$

$$w^- = \frac{R\sqrt{2D_z^- \Delta t}}{\Delta t}. \tag{3.21}$$

The new, corrected position of a transmitted particle is then obtained from

$$\underline{z}(t_i) = \underline{z}(t_{i-1}) + \Delta z \tag{3.22}$$

$$= \underline{z}(t_{i-1}) + \left[\left(w^+\Delta t^+\right) + \left(w^-\Delta t^-\right)\right]. \tag{3.23}$$

Figure 3-6 illustrates the corrections that apply to a particle approaching z_1 from a region of higher diffusivity. While the semi-reflecting boundary correction only affects particles in the region $z > z_1$, (3.23) applies to particles approaching the diffusivity interface from either side.

3.2.3 Testing and Validation

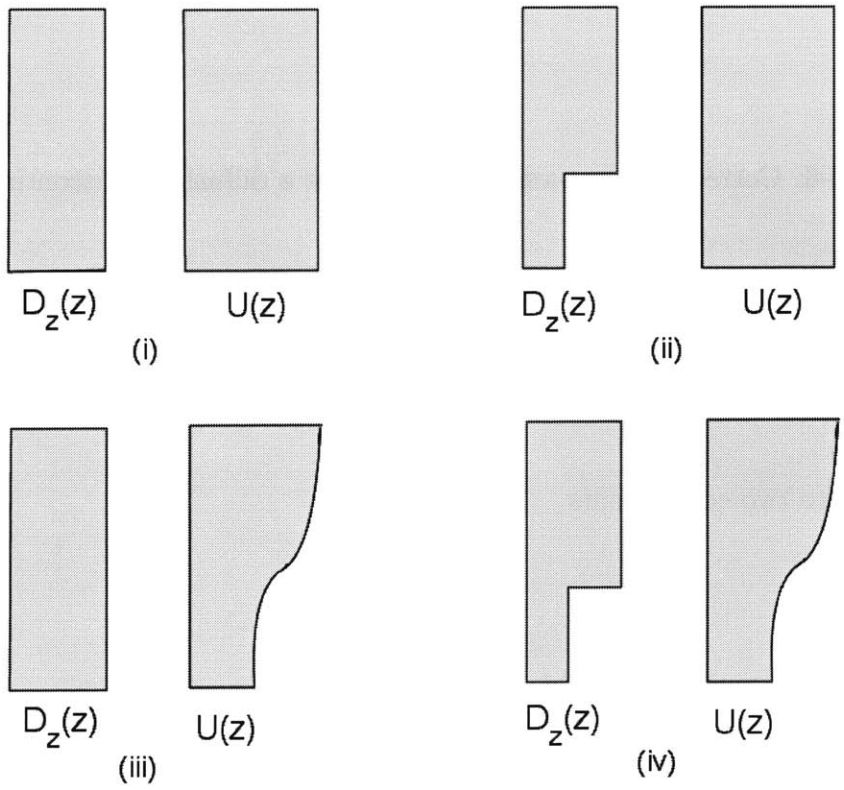

Figure 3-7: Diffusivity and mean velocity profiles used to test model performance.

The corrections for diffusivity discontinuities discussed in the previous section were tested by tracking 1000 particles, uniformly distributed over the depth of the model domain, which was chosen to be 46.7 cm for comparison with some of the experimen-

tal runs. Four different base cases with various diffusivity and velocity profiles were chosen, as shown in Figure 3-7: (i) Constant velocity profile, constant diffusivity profile; (ii) Constant velocity profile, stepped diffusivity profile; (iii) Hyperbolic tangent velocity profile, constant diffusivity profile; (iv) Hyperbolic tangent velocity profile, stepped diffusivity profile. These cases were chosen, so that bugs in the Netlogo code could be isolated, based on whether they were linked to the implementation of a particular velocity or diffusivity profile type. Each diagnostic simulation ran for a period of 310 s, with $\Delta t = 1\,\mathrm{s}$. The results were compared to those obtained from identical simulations using a particle-tracking model developed in Fortran by Peter Israelsson at MIT (unpublished). A comparison of the results of the simulations is shown in Table 3.2. There are some discrepancies, so further investigation was needed before the model could be validated.

Another test was devised to count the number of particles approaching the diffusivity discontinuity from above and below side (N^+ and N^-). This was done both for a single time step and for an extended duration of run time. Of the N^+ particles, cumulative fractions $(1-\varphi)$ and φ were observed to be reflected and transmitted, respectively, after an initial period. Statistically (i.e., after multiple time steps), all N^- particles were transmitted from below. These results suggested that the corrections for the discontinuous diffusivity profile were performing as expected. However, exactly $(1-\varphi)N^+$ particles were not always reflected during a single time step, meaning that 1000 particles were insufficient for statistical convergence. The error for a single time step decreased when the number of particles was increased from 1000 to 5000, such that any biased particle migration was attributed to artificial noise created by the finite number of particles and the fact that R is actually "pseudo"-random in the model, since numbers are generated in a deterministic fashion by the Netlogo code.

Table 3.2: Comparison of statistics from Netlogo simulations to Israelsson's model simulations. χ_x and χ_z are the mean horizontal and vertical particle locations, respectively. σ_x^2 and σ_z^2 are the variances in the longitudinal and vertical directions. Simulations ran for 310 s with time steps, $\Delta t = 1$ s. 1000 particles were used in each simulation.

Inputs		**Netlogo Model**				**Israelsson Model**			
Velocity	**Diffusivity**	χ_x **(cm)**	σ_x^2 (cm^2)	χ_z **(cm)**	σ_z^2 (cm^2)	χ_x **(cm)**	σ_x^2 (cm^2)	χ_z **(cm)**	σ_z^2 (cm^2)
constant	constant	900.0	0.0	24.7	86.3	899.5	0.0	23.2	105.3
shear	constant	1,289.0	38,912.8	25.1	89.6	1,292.0	36,110.8	23.6	105.3
constant	stepped	900.0	0.0	22.5	202.8	899.5	0.0	23.5	177.9
shear	stepped	1,089.0	88,165.4	22.7	203.3	1,143.7	59,631.4	23.6	105.3

Another reason why perfect (statistical) agreement is not observed between the model results in Table 3.2 may be that Israelsson's model utilized a multiple-time-step approach (i.e., a different time step in the regions $z > z_1$ and $z < z_1$) to account for the diffusivity discontinuity, which differs from the mid-step adjustment method chosen here. This approach is more computationally expensive (Israelsson, personal communication) and was not considered.

In any event, the model was also validated by comparing the predictions to experimental results. Each of the experimental runs were simulated by the RWPT model, by introducing 10,000 particles at the top of the canopy and by running the model with $\Delta t = 1$ s. The only constraints on the time step were: (i) it had to be greater than the Lagrangian time scale and (ii) it had to be small enough that boundary effects were unimportant (i.e., $\Delta t \ll (H - z_1)^2/2D_{z,sl}$ from section 3.2.2). Although greater accuracy is expected as $\Delta t \rightarrow T_L$, time steps less than 1 s generally resulted in excessive model run times, due to the high levels of computation required. Predictions of observed dispersion coefficients were made for each of the experimental runs, at times corresponding to the experimental μ. These values were compared to the experimentally determined values of K_x. Reasonable agreement was found, as shown in Figure 3-8 and Table 3.3.

3.2.4 Data Processing

For each of the numerical simulations (corresponding to the experimental runs), 10,000 particles (sufficient to provide statistical convergence) were released at $z = h$ and tracked for 3000 seconds, or until $K_x = 0.5\sigma_x^2/t$ became approximately constant with time. The following outputs were written directly to text ("*.txt") files:

t = time (discretized into increments of Δt),

$U_c(t)$ = the mean "velocity" of the particles in the longitudinal direction (i.e., the mean particle x-coordinate divided by t),

$\sigma_x^2(t)$ = the variance in the longitudinal direction,

Table 3.3: Agreement of K_x values predicted by the RWPT model with experimentally determined values.

Run	$K_{x,observed}$, cm^2/s	$K_{x,predicted}$ (Netlogo), cm^2/s
A6	32.4	33.7
B6	102.7	51.7
C6	60.3	87.5
A1	35.2	16.8
B1	119.5	40.4
C1	63.7	69.8
A2	40.6	16.8
B2	100.3	89.3
C2	57.7	81.7
A3	42.4	61.1
C3	67.6	116.0
A5	31.6	16.5
C5	64.6	58.7
A	85.3	91.4
B	18.7	42.0
C	136.2	154.8
D	91.0	101.4
E	287.7	294.2
G	75.3	97.4
H	421.2	379.9
I	212.0	278.9
C6D	102.7	130.3
C2D	109.7	112.1
A2D	50.7	56.2
A3D	59.2	54.7

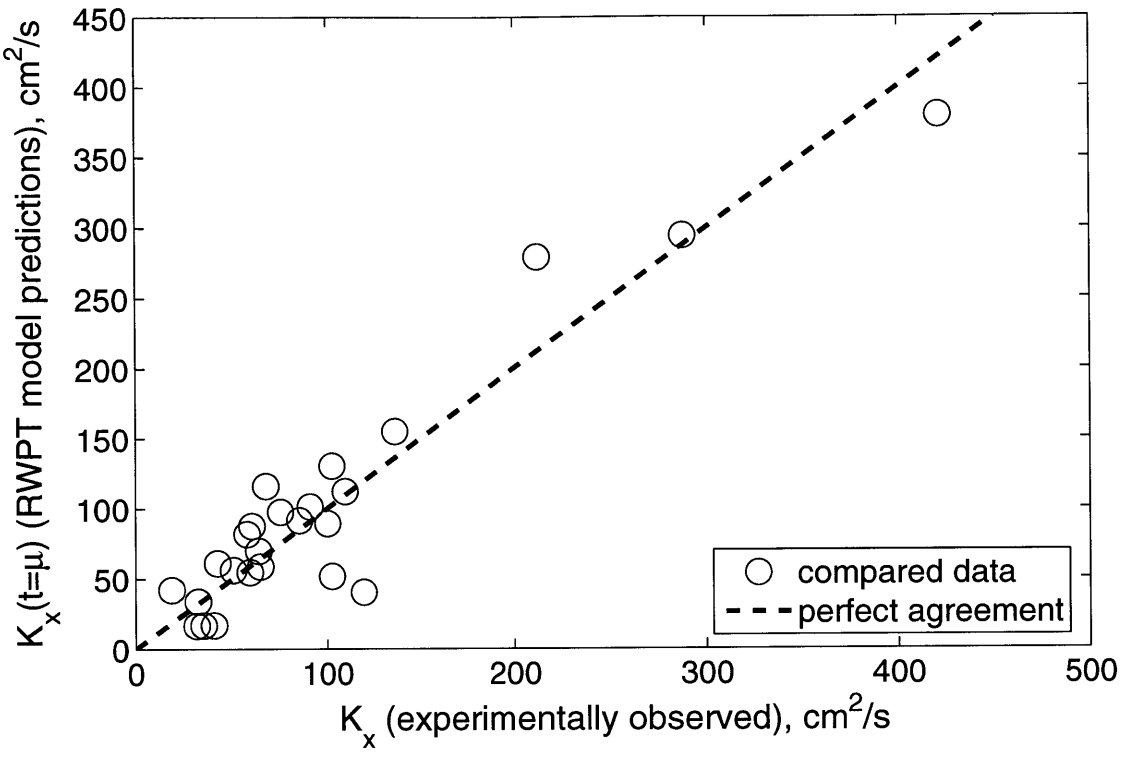

Figure 3-8: Agreement of K_x values predicted by the RWPT model with experimentally determined values.

$G(t)$ = the skewness of the particle distribution,

$\kappa(t)$ = the kurtosis of the particle distribution,

$A(x, z, t_{end})$ = a matrix containing the spatial co-ordinates of all 10,000 particles at the end of the simulation, $t = t_{end}$.

These files were then imported to MATLAB [109], where the data was batch-processed (see Appendix B for "*.m" files containing code that was written to do this). A histogram of the x-coordinates provided a depth-average "concentration" distribution of particles. This was normalized by the number of particles (10,000) for comparison to the experimentally obtained tracer concentration profiles.

Chapter 4

Results and Discussion

Table 4.1: Summary of experimental conditions and flow parameters.

Run	h, cm	H, cm	a, cm^{-1}	S, $x10^5$	U_1, cm/s	U_2, cm/s	ΔU, cm/s	$h - z_1$, cm	Re_d	Re_H $x10^{-4}$	C_D
A	14.0	46.7	0.025	0.99	1.6	3.7	3.2	12.7	78	1.5	1.0
B	14.0	46.7	0.025	0.18	0.5	1.5	1.3	9.1	30	0.6	1.9
C	14.0	46.7	0.034	2.50	2.0	5.5	4.9	10.9	102	2.1	1.2
D	14.0	46.7	0.034	1.20	1.4	3.8	3.5	12.3	66	1.4	1.2
E	14.0	46.7	0.040	7.50	4.2	10.6	9.5	11.6	210	4.1	0.7
G	14.0	46.7	0.040	1.30	1.4	3.7	3.3	10.3	66	1.4	1.1
H	14.0	46.7	0.080	10.00	3.3	11.1	11.0	11.2	162	4.1	0.7
I	14.0	46.7	0.080	3.40	2.1	7.2	7.4	9.8	102	2.7	0.6
A6	7.0	29.8	0.025	0.30	0.6	1.6	1.6	5.8	17	0.4	2.6
B6	7.0	29.8	0.025	8.04	3.3	8.4	7.0	7.0	152	2.2	2.5
C6	7.0	29.8	0.025	2.42	1.7	4.4	3.7	3.4	83	1.1	2.7
A1	7.0	23.6	0.025	1.06	0.7	1.6	1.4	7.0	30	0.3	5.5
B1	7.0	23.6	0.025	11.57	4.3	10.2	9.1	7.0	207	2.0	1.7
C1	7.0	23.6	0.025	4.27	2.2	5.1	4.8	5.1	111	1.0	2.4
A2	7.0	14.0	0.025	1.73	1.3	2.9	2.4	7.0	75	0.3	1.5
B2	7.0	14.0	0.025	48.66	7.8	15.5	11.8	7.0	461	1.7	1.3
C2	7.0	14.0	0.025	30.05	5.0	10.6	7.8	7.0	283	1.1	1.9
A3	7.0	10.5	0.025	12.44	2.5	5.4	5.5	2.9	136	0.4	2.3
C3	7.0	10.5	0.025	66.61	6.9	14.7	14.6	7.0	395	1.0	1.7
A5	7.0	8.8	0.025	28.35	2.8	5.3	3.2	3.9	163	0.3	3.6
C5	7.0	8.8	0.025	134.04	9.9	18.7	12.6	7.0	582	1.1	1.4
C6D	7.0	29.8	0.080	2.03	0.8	4.6	5.3	7.0	26	1.1	3.2
C2D	7.0	14.0	0.080	36.64	3.0	9.3	9.5	7.0	142	0.9	2.0
A2D	7.0	14.0	0.080	4.74	1.0	3.4	3.4	5.3	46	0.3	2.2
A3D	7.0	10.5	0.080	23.19	2.0	5.2	4.6	5.4	101	0.3	2.1

4.1 Experimental Results

Flow parameters for the twenty-five experiments that modeled submerged vegetated flows are listed in Table 4.1. The first eight rows in the table correspond to runs of the same letter in [37].

Bulk drag coefficients obtained from (2.23), and reported in Table 4.1, show fair agreement with White's [123] expression for the drag coefficient due to flow around an isolated cylinder (see Figure 4-1). The scatter at $Re_d < 200$ is likely to be due to estimation of S, the uncertainty of which increased as $H/h \rightarrow 1$, since less data points were available above $z = h$.

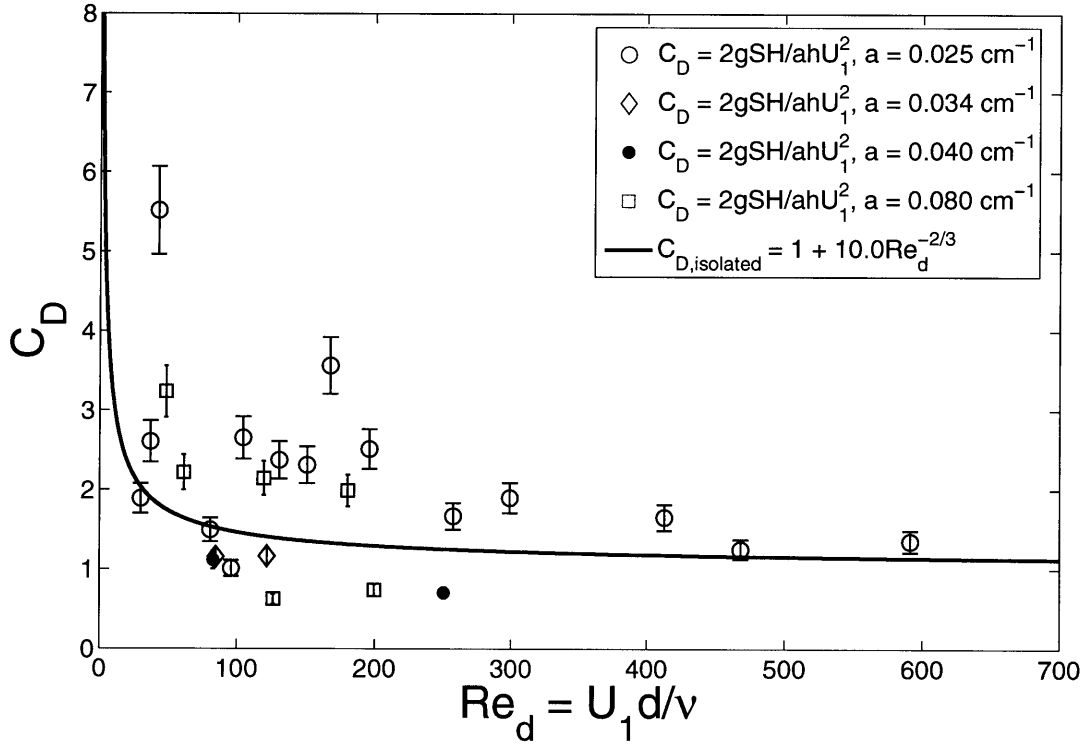

Figure 4-1: The bulk drag coefficient determined from (3.8) compared to C_D for an infinitely long, isolated cylinder. Different markers indicate the different dowel densities used in the experiments. The vertical bars represent the uncertainty in C_D, which was estimated to be approximately 10 % based on values of uncertainty in S and U_1 from [35]. In some instances, the vertical bar is smaller than the marker.

Figure 4-2 shows that $u_* = \sqrt{gS(H-h)} \simeq \sqrt{-\overline{u'w'}|_h}$ for the entire range of H/h. This is not surprising, given that the very definition of a shear velocity is $u_* \equiv \sqrt{\tau_o/\rho}$,

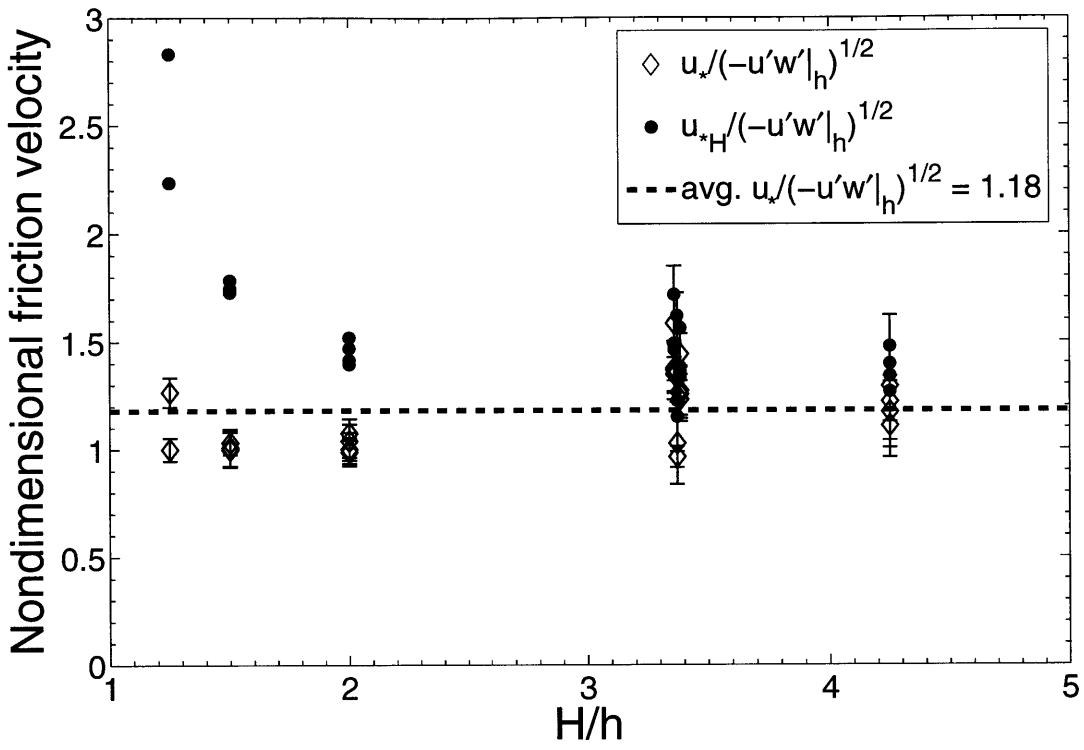

Figure 4-2: The ratio of the friction velocities, $u_* = \sqrt{gS(H-h)}$ (diamonds) and $u_{*H} = \sqrt{gSH}$ (open circles) to the square root of the Reynolds stress evaluated at the top of the canopy. Vertical bars represent the estimated uncertainty in $u_*/\sqrt{-\overline{u'w'}\,|_h}$.

where τ_o is the shear stress at the bottom of a logarithmic layer (see e.g., [55, pp. 552]). As such, this confirms the suitability of the choice of u_* as the characteristic velocity scale for dispersion in the fast zone, rather than u_{*H}, which is seen to vary considerably over a range of H/h conditions (Figure 4-2). For thoroughly submerged vegetation ($H/h > 5$), the flow approaches a rough boundary layer, and u_* and u_{*H} are equally valid velocity scales for dispersion.

Further, as anticipated in §2.8.1 the scaled ratio $\Delta U/u_{*H}$ is reasonably constant over the range of H/h (see Figure 4-3). The same data shows that $\Delta U \simeq 6.3u_*$ has the same statistical accuracy over the entire range of data. However, we see that in the transition from $H/h = 2$ to $H/h = 1$, the region in which the two zone model is most sensitive to the exchange term of (2.72), $\Delta U/u_*$ increases significantly. Thus, u_{*H} is the more consistent scale for ΔU. This is because u_{*H} captures the total shear

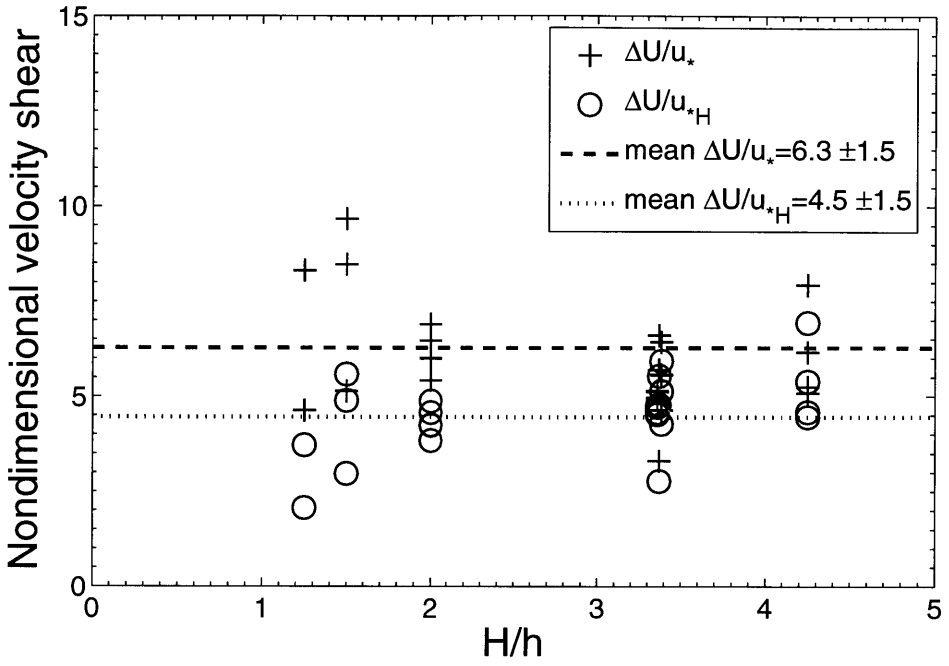

Figure 4-3: The ratio of total shear to friction velocity and best fit averages ± standard deviations.

across the mixing layer, including the contribution from the region $z < h$, which is not necessarily negligible.

Figure 4-4 shows the estimated depth average vertical diffusivity ($D_{z,sl}$, see §3.2.1) for the region $z > z_1$, plotted versus the $\Delta U t_{ml}$ scaling proposed by [38]. Aside from three anomalous values, a fairly linear relationship is observed, and the proportionality constant, $D_{z,sl}/\Delta U t_{ml} = 0.016$, agrees with observations for vegetated shear layers [38]. A more practical scaling, $D_{z,sl}/\Delta U H$, provides a statistical fit that is almost as good (Figure 4-5). However, the latter relationship ($D_{z,sl} = 0.013 \Delta U H$) is for experimental values of $t_{ml}/H \geq 0.6$ only. It may not apply in conditions where the shear layer is confined to a small portion of the flow ($t_{ml} \ll H$). No explanation for the behavior of the three anomalous data points (corresponding to Runs B1, B6 and C1 - see Table 4.2) could be found. Noise in the velocity measurements was ruled out as a possible contributor, since in all three cases, the majority of $-\overline{u'w'}$ values far exceeded the associated uncertainties.

[21] suggest that the ratio of the tracer velocity to the depth-average fluid velocity

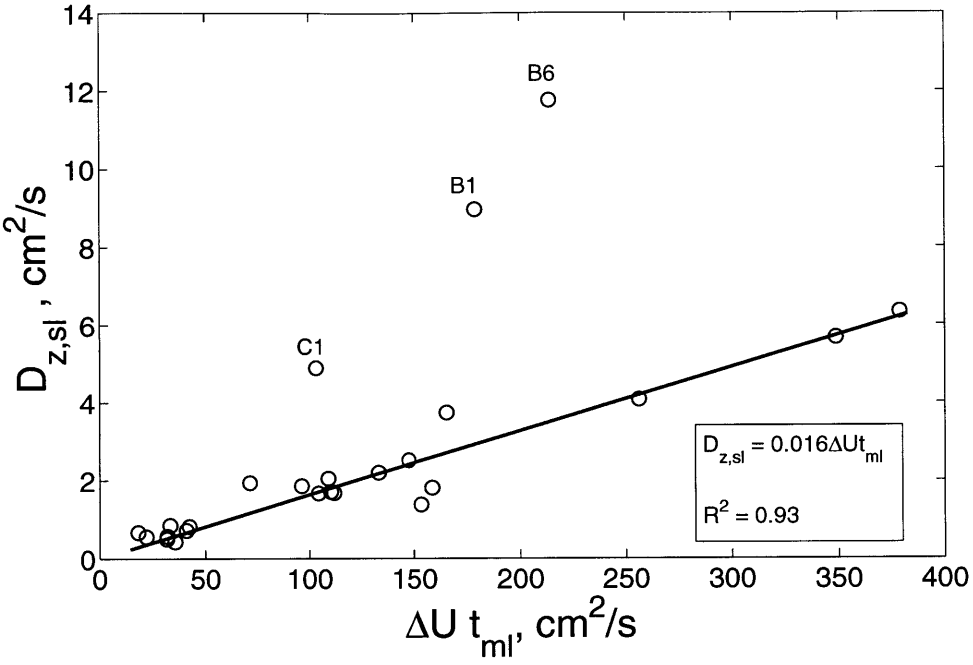

Figure 4-4: Estimates of mean vertical diffusivity in the region $z > z_1$ versus $\Delta U t_{ml}$.

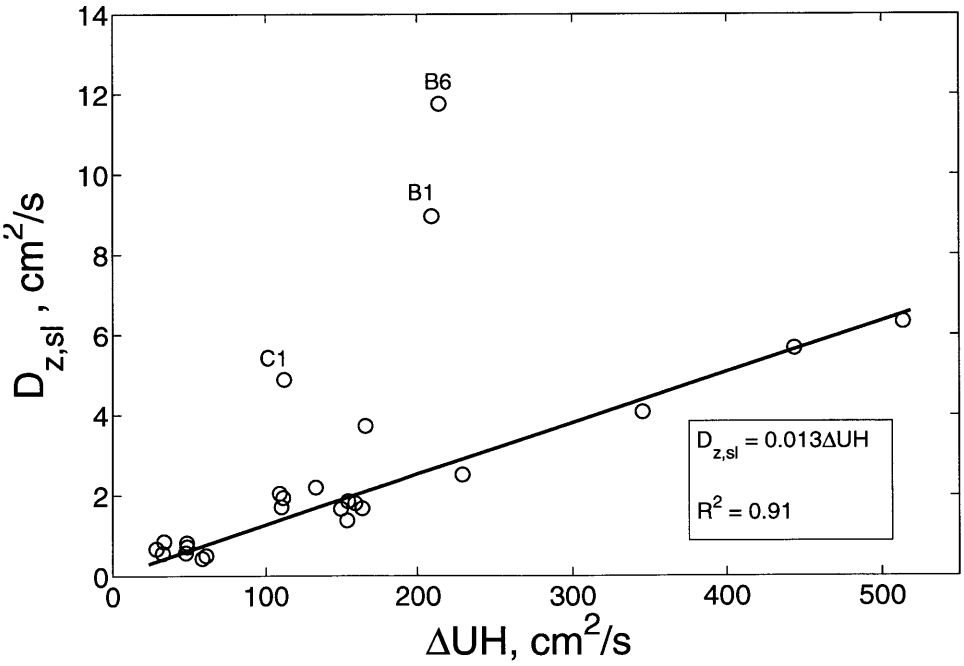

Figure 4-5: Estimates of mean vertical diffusivity in the region $z > z_1$ versus $\Delta U H$.

Table 4.2: Estimated mean vertical diffusivities for the region $z > z_1$, and relevant velocity and length scales.

Run	$D_{v,sl}$, cm^2/s	ΔU, cm/s	t_{ml}, cm	H, cm	h, cm	z_1, cm
A	1.67	3.2	32.6	46.7	13.9	1.2
B	0.50	1.3	24.4	46.7	13.9	4.8
C	2.52	4.9	30.1	46.7	13.9	3.0
D	1.68	3.5	31.9	46.7	13.9	1.6
E	5.67	9.5	36.7	46.7	13.8	2.2
G	1.86	3.3	29.2	46.7	13.8	3.5
H	6.33	11.0	34.4	46.7	13.8	2.6
I	4.08	7.4	34.6	46.7	13.8	4.0
A6	0.57	1.6	20.0	29.75	7	1.2
B6	8.96	7.0	25.4	29.75	7	0.0
C6	1.94	3.7	19.1	29.75	7	3.6
A1	0.56	1.4	16.1	23.6	7	0.0
B1	11.8	9.1	23.6	23.6	7	0.0
C1	4.89	4.8	21.7	23.6	7	1.9
A2	0.85	2.4	14.0	14	7	0.0
B2	3.74	11.8	14.0	14	7	0.0
C2	2.05	7.8	14.0	14	7	0.0
A3	0.43	5.5	6.4	10.5	7	4.1
C3	1.38	14.6	10.5	10.5	7	0.0
A5	0.67	3.2	5.6	8.75	7	3.1
C5	1.71	12.6	8.8	8.75	7	0.0
C6D	1.81	5.3	29.8	29.75	7	0.0
C2D	2.20	9.5	14.0	14	7	0.0
A2D	0.82	3.4	12.3	14	7	1.7
A3D	0.72	4.6	8.9	10.5	7	1.6

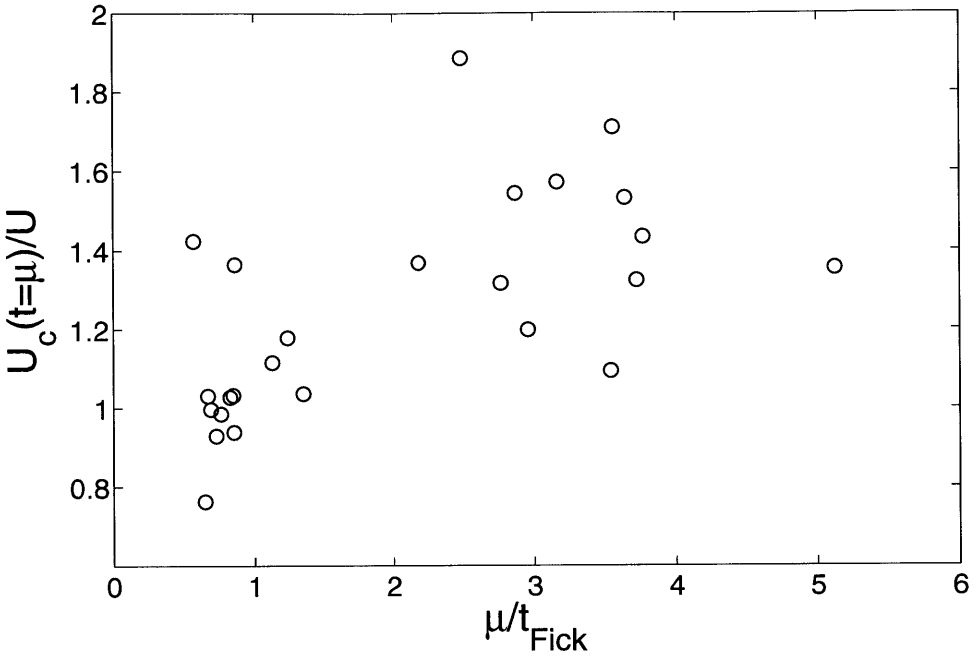

Figure 4-6: The ratio of mean longitudinal tracer velocity, $U_c(t = \mu)$, to the depth-average fluid velocity, U, versus the ratio of the mean passage time of the tracer, μ, to the Fickian time scale, $t_{Fick} = 0.4\,H^3 / \int_0^H D_z\,dz$.

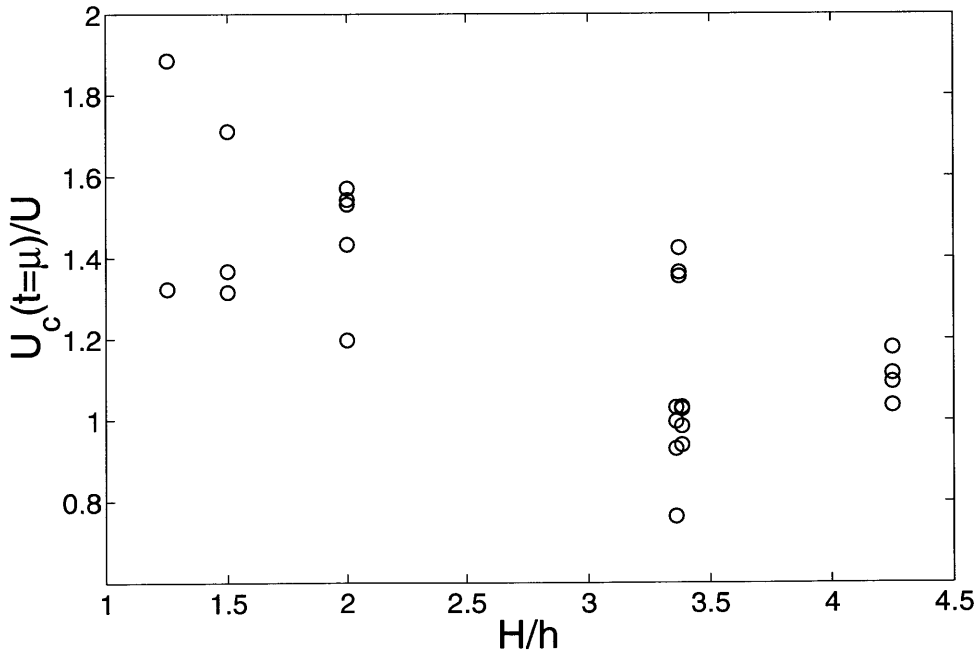

Figure 4-7: The ratio of mean longitudinal tracer velocity to depth-average fluid velocity over the range $1 < H/h < 4.5$.

is a good indicator of whether the Fickian limit has been reached. This is an intuitively valid argument, since we would expect a well-mixed contaminant to travel with the mean fluid speed. However, this is not borne out by Figure 4-6, which suggests that the mean travel time of the tracer plume, μ, relative to the Fickian time scale, $t_{Fick} = 0.4\,H^3/\int_0^H D_z\,dz$, is not well correlated with the ratio of the mean tracer velocity to the fluid velocity, $U_c(t = \mu)/U$. Instead, Figure 4-7 shows a trend of increasing $U_c(t = \mu)/U$ with decreasing H/h, in the range $H/h \lesssim 2$. This may be explained by a difference between the initial tracer conditions in this study, and those in [21]. Whereas we injected at a single point, the tracer releases in [21] resembled well-mixed line sources. Since all of our injections were at $z = h$, we expect higher velocities to be sampled more frequently in the near-field for experiments where the canopy is not deeply submerged. Mixing occurs preferentially in the fast zone, such that higher velocities are sampled first. This tendency increases as $H/h \rightarrow 1$ and the K-H vortices become confined by the free surface [74]. Vortex penetration is reduced (i.e., $z_1 \rightarrow h$), thus preventing mixing to regions of low velocity. Thus, $U_c(t = \mu)/U > 1$ for $H/h \lesssim 2$ (Figure 4-7), since the tracer is more rapidly exposed to the fast-flowing fluid above the canopy than to the slow-flowing fluid below z_1. The same trend is not observed for $H/h > 2$, since the K-H vortices are unconfined, and thus control mixing across the majority of the cross section (i.e., $t_{ml} \approx H$) such that regions of lower velocity are more readily sampled.

The concentration-time distribution for run $A5$ is shown in Figure 4-8. Note that individual realizations are consistent with the average, implying that five repetitions adequately describe each experiment[1]. A non-zero skewness coefficient (also shown in Figure 4-8) reveals a slight deviation from Gaussian form that agrees with observations in natural channels [77]. The statistics of all temporal concentration distributions are presented in Table 4.3, along with the dispersion coefficients obtained from the approximation of (2.66), $K_x = \frac{\sigma_x^2}{2\mu}$. In all cases, $Pe = U_c X/K_x \gg 1$, where Pe is the longitudinal dispersion Péclet number. This confirms the prevalence of advection-dominated flow [60], validating the frozen cloud assumption, made in §3.1.3.

[1]See Appendix A for concentration-time distributions for all the experimental runs

Table 4.3: Statistics derived from temporal moment analysis of concentration distributions, adjusted dispersion coefficients, and estimated time scales for experimental accuracy from RWPT simulations.

Run	μ, s	σ_t, s	Pe	K_x, $cm^2\,s^{-1}$	$\varepsilon_{Kx}{}^*$, $cm^2\,s^{-1}$	$K_{x,NL}{}^*$, $cm^2\,s^{-1}$	$\tilde{t}_\mu = \mu\frac{D_{z,a}}{H^2}$	$\tilde{t}_{10\%}{}^{**}$
A	390	89.1	39	85	±10	130	0.3	1.0
B	1220	231	58	19	±3	26	0.3	0.7
C	252	58.4	37	140	±10	210	0.3	0.9
D	356	80.3	40	90	±10	150	0.3	1.2
E	137	34.1	32	290	±20	440	0.3	0.9
G	382	81.0	45	75	±5	120	0.3	1.3
H	123	35.2	25	420	±30	690	0.3	2.2
I	192	48.6	31	210	±25	380	0.3	1.6
A6	729	140	55	32	±2	43	0.5	1.0
B6	141	21.1	89	100	±10	110	1.4	0.9
C6	252	38.9	84	60	±3	110	0.5	2.2
A1	567	100	65	35	±3	44	0.2	0.4
B1	96.8	13.0	111	120	±5	130	2.0	1.5
C1	192	26.6	104	64	±4	75	0.3	0.5
A2	332	48.3	95	41	±5	46	1.5	1.6
B2	60.7	5.9	210	100	±20	110	1.1	1.6
C2	117	12.1	189	58	±1	66	1.2	1.7
A3	234	29.2	129	42	±3	60	0.9	2.0
C3	89.4	8.7	211	68	±1	75	1.1	1.2
A5	172	15.8	236	32	±1	41	1.0	1.8
C5	70	5.9	281	65	±4	70	1.5	1.1
C6D	289	62.2	43	103	±5	130	0.5	1.1
C2D	128	19.0	91	110	±5	120	1.5	1.4
A2D	326	52.3	77	51	±4	61	1.3	2.4
A3D	231	33.8	93	60	±1	65	1.4	1.3

* ε_{Kx} is the uncertainty in K_x, corresponding to the standard error of the observed values. This estimate of uncertainty does not contain any information about the closeness of the approximation, $K_x = 0.5\frac{\partial\sigma_x^2}{\partial t} \approx \frac{\sigma_x^2}{2\mu}$, discussed in Chapter 3. This is accounted for by $K_{x,NL}$, which represents subsequently adjusted values of the experimentally observed K_x, based on RWPT simulation results (discussed later in § 4.2).

**$\tilde{t}_{10\%} = t_{10\%}\frac{D_{z,a}}{H^2}$ and is estimated from RWPT model results (see § 4.2).

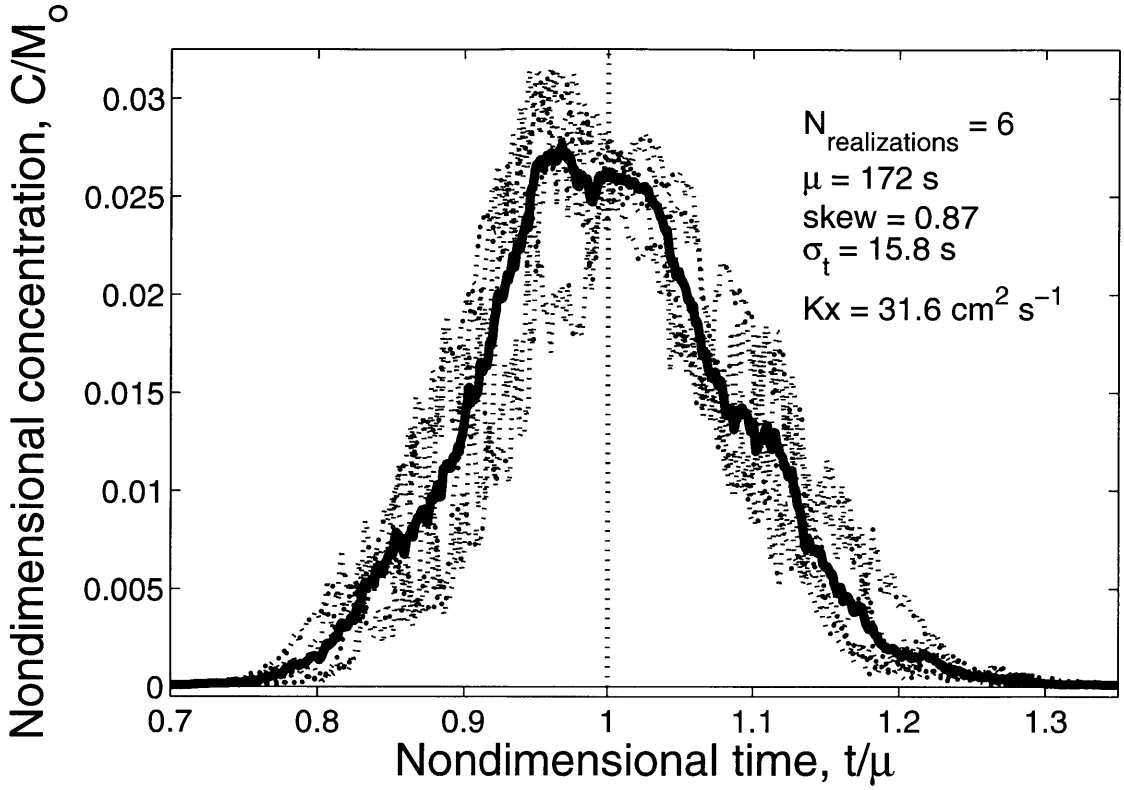

Figure 4-8: The collapse of the concentration-time curves for run A5. The ensemble average (solid line) is superimposed on the individual realizations (dotted curves). The time and concentration axes have been normalized by the mean arrival time (μ) and the total recovered mass of the solute (M_0), respectively. Normalization of the concentration data eliminates, so far as is possible, non-uniformities across realizations caused by slight differences in the masses of tracer injected [122].

The results from runs A4 and X4D were compared with predictions of the dispersion coefficient for emergent vegetation from (2.76). The comparisons are shown in Table 4.4, which also shows the predicted relative contributions to total dispersion by vertical shear (K_{vs}) and stem-scale processes (K_d). Since $ad < 0.1$ for both experiments, K_d was assumed to result only from velocity heterogeneity within the cylinder array. Agreement is reasonably good, although the predicted dispersion rates are slight underestimates of the observed values. It is possible that this may be partially due to trapping of tracer within empty holes in the Plexiglas boards at the bed. Although trapping in primary cylinder wakes is expected to be insignificant for $ad < 0.1$, and is therefore not included in (2.76), Table 1 of [122] shows that this process may contribute to some extent for $ad < 0.1$. The resonant motion of the free

surface described in §3.1.1, may have enhanced dispersion in the flume, such that the predictions were too low. In addition, values of K_{vs} are sensitive to the predicted vertical diffusivity within the array. Here, a value of $0.17Ud$ was used, based on field measurements made by [62]. However, the key point is still clear, i.e., both the predicted and observed dispersion coefficients are generally an order of magnitude smaller than those for runs with submerged vegetation (Table 4.3). This validates the assumption made in Chapter 2 that K_1 is negligible.

Table 4.4: Comparison of predicted with observed dispersion coefficients for emergent canopies.

Run	Re_d	U, cm/s	C_D *	a, cm^{-1}	H, cm	K_x, cm^2/s (observed)	K_d, cm^2/s	K_{vs}, cm^2/s	$K_x = K_d + K_{vs}$, cm^2/s (predicted)
A4	367	6.1	1.20	0.025	5	7.43	2.40	4.63	7.02
X4D	310	5.2	1.22	0.080	5	6.75	2.09	3.99	6.08

* Calculated from $C_D = 1 + 10.0Re_d^{-2/3}$[123], see § 2.2.3.

4.1.1 Dispersion with Vortex-Driven Exchange

The velocity measurements in Table 4.1 show that $\beta_1 = (U_2 - U_1)/\Delta U = 0.68 \pm 0.05$ is not a function of H/h. Furthermore, Figure 4-3 shows that $\beta_2 = \Delta U/u_{*H} \simeq 4.5$. Given these values, $\beta = 40\beta_1^2\beta_2 \simeq 83$. In Figure 4-9 the normalized dispersion coefficient, $K_x/[u_*(H-h)]$, is plotted versus H/h. The theoretical prediction, (2.84), is fit to the experimental data using the single parameter β. This yields (with 95% confidence) a value of $\beta = 93 \pm 11$, which agrees with our expectations, within uncertainty. The dashed and dash-dot lines in Figure 4-9 represent the contributions of the exchange and logarithmic-shear dispersion terms, respectively. For low values of H/h (< 2.5), inefficient exchange is the primary mechanism for dispersion, with fast-zone shear playing a relatively insignificant role. The overall normalized dispersion peaks at around $H/h = 1.2$ where the contribution of the exchange term is at a maximum, before dropping off rapidly as $H/h = 1$. Realistically of course, K_x will not go to zero at H/h but will assume a finite value of K_1 as the limit of emergent vegetation is

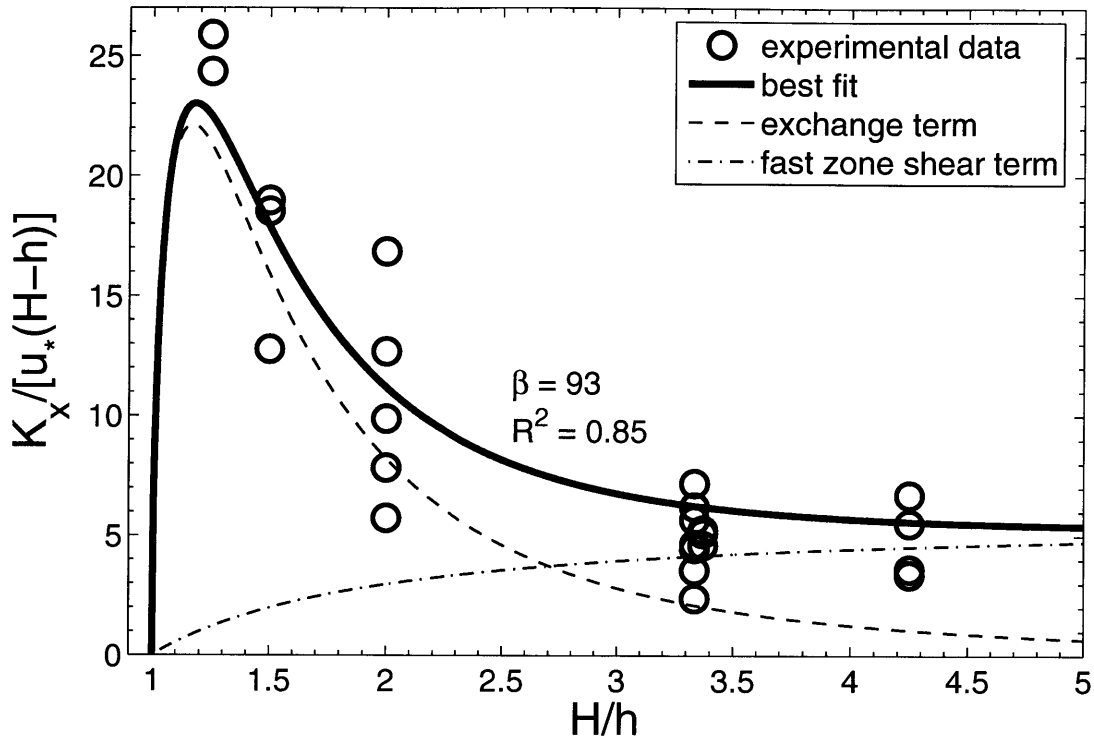

Figure 4-9: Least squares fit of equation (2.84) to experimental dispersion coefficient data. The contributions of the first (dash curve) and second (dash dot curve) terms in (2.51) are shown. The solid curve represents their sum.

approached and stem-scale mixing controls dispersion. Conversely, as H/h increases, logarithmic-shear dispersion in the fast zone grows in importance and inhibited exchange is not as influential. A transition occurs at $H/h \approx 2.7$, beyond which the nondimensional dispersion coefficient asymptotes to the rough boundary layer value, as anticipated. The contribution of the exchange term to the dimensionless dispersion is negligible (less than 10 % of the total) for $H/h \gtrsim 5.5$. Since the total depth average velocity scales on u_{*H} (see Figure 4-10), it is useful to note that the practical scaling, K_x/UH, is approximately constant (0.97 ± 0.03) over the range $1.5 < H/h < 5$.

Also, over the range $H/h \lesssim 5$, $K_x/[u_{*H}H]$ is roughly constant (see Figure 4-11) at about half the value for a logarithmic boundary layer. That is, in flows dominated by vegetation, the longitudinal dispersion is decreased, compared to a bare bed. For these experiments, the normalized depth average diffusivity $D_{z,a}/u_{*H}H = 0.073$, which is comparable to $D_{z,a}/u_{*H}H = 0.067$ for logarithmic boundary layers [33, pp. 93].

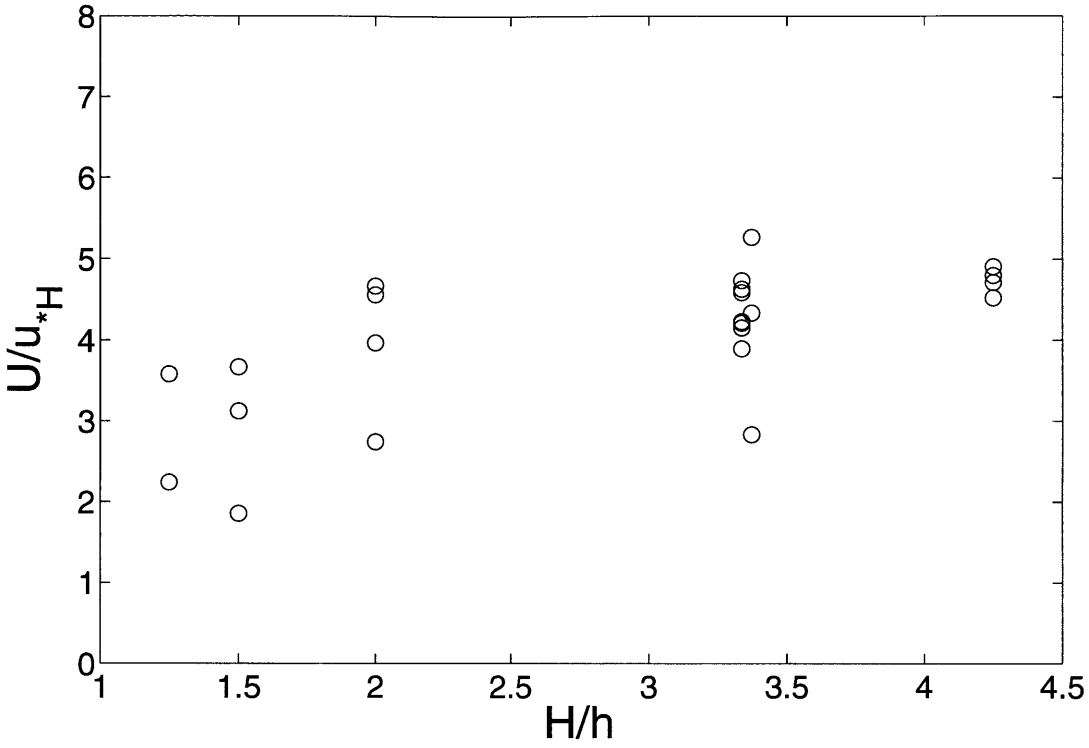

Figure 4-10: Experimental data showing the approximately constant relationship between the depth-averaged velocity, U, and the friction velocity, u_{*H}.

This implies that vertical mixing rates are practically equivalent, and the difference between K_x for a bare channel and the value for a vegetated channel of the same depth must be attributed to the different velocity profiles. From (2.42), the contribution of the shape of the velocity profile to dispersion can be expressed as

$$I = -\frac{1}{H}\int_0^H \langle\bar{u}\rangle'' \int_0^z \int_0^z \langle\bar{u}\rangle'' dz\, dz\, dz \quad \sim \quad u_{*H}^2 H^2. \tag{4.1}$$

For logarithmic layers, $I = I_{bl} = 0.40 u_{*H}^2 H^2$, from multiplication of the mean diffusivity and longitudinal dispersion constants. For a representative vegetated channel, we consider a velocity profile with a step at mid-depth, i.e. $H/h = 2$, with velocities U_2 and U_1 in the upper and lower layers, respectively (e.g., see Figure 2-5). For this profile,

$$I = \frac{1}{48}\left(U_2 - U_1\right)^2 H^2 \tag{4.2}$$

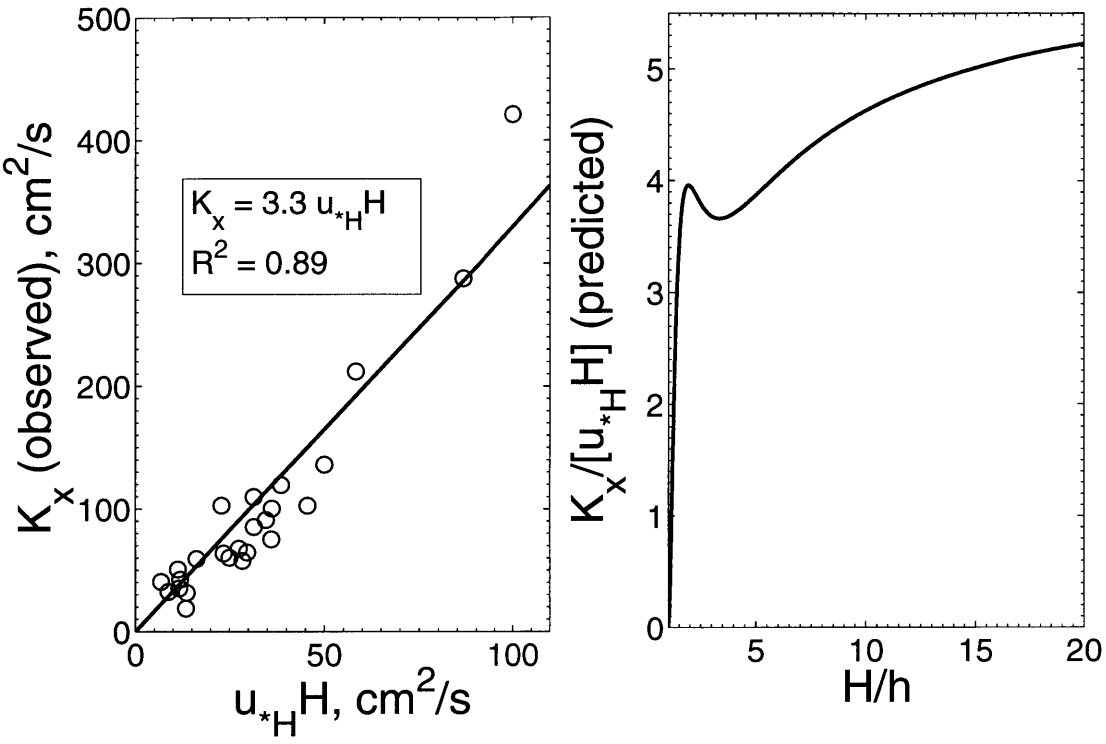

Figure 4-11: (a) Linear fit to experimental data showing $K_x/u_{*H}H \approx 3.3$ over the range of H/h in this study. (b) Variation of $K_x/u_{*H}H$ predicted by theoretical model over a range of H/h.

(after [33, pp. 93]). Substitution of the experimentally determined relationship $(U_2 - U_1) = 3.09u_{*H}$ into (4.2) yields $I = I_{vc} = 0.21u_{*H}^2H^2$ for a vegetated channel. Thus, $I_{bl}/I_{vc} = 1.9$. This indicates that for a fixed potential gradient, i.e. $u_{*H} = \sqrt{gSH}$, the logarithmic profile has nearly twice the velocity heterogeneity, directly explaining why the dispersion is twice as high. The greater velocity heterogeneity is largely due to the far greater mean velocity that may occur in the comparatively lower drag, bare channel.

4.1.2 Dispersion with Diffusion-Limited Exchange

Now we consider the regime of turbulent diffusion-dominated exchange (i.e., $2 < C_Dah$, as discussed in §2.8.2). No experimental data on longitudinal dispersion coefficients for submerged, dense ($ad > 0.1$) canopies are available for comparison to

(2.91). Therefore, we will examine (2.91) for typical field conditions. Vegetation densities are usually greatest in mangrove forests[2] (see e.g., [67]), so we assume $ad = 0.4$ as a reasonable upper limit. Since vortex-driven exchange is expected to dominate in sparse canopies ($ad \lesssim 0.1$), we consider a range $0.1 < ad < 0.4$ for the regime of diffusion-limited exchange. We assume a constant aspect ratio, $d/h = 0.05$, based on geometric similitude observed among aquatic plants [76]. It is also reasonable to assume $C_D \simeq 1$. Data from the vortex-driven exchange regime (Table 4.1) imply that $[(U_2 - U_1)/u_{*H}]^2 \simeq 9.96 \pm 4.38$ and we use this as an approximation for the case of diffusion-dominated exchange. This is a reasonable extrapolation because for a fixed potential gradient (i.e., $u_{*H} = \sqrt{gSH}$), denser vegetation will require a lower mean velocity U, offsetting the increased velocity difference due to additional drag. Finally, we take the proportionality constant for the vertical diffusivity in the slow zone $\alpha = 0.15$, and evaluate (2.91). The nondimensional dispersion coefficients for $ad = 0.1$ and $ad = 0.4$ are shown over a range of H/h in Figure 4-12 (solid lines), for the typical field conditions mentioned above. Also shown are the contributions of the two terms in (2.91) for the case of $ad = 0.1$. As expected, logarithmic dispersion in the fast zone dominates in the limit of $H/h \to \infty$ but the contribution of the exchange term persists for higher values of H/h than in the case of vortex-driven exchange. In fact, the exchange term does not become negligible (i.e., less than 10 % of the total dispersion) until $H/h \gtrsim 16$ for $ad = 0.1$ and $H/h \gtrsim 17.5$ for $ad = 0.4$.

We have seen that trapping in the slow zone through inefficient exchange is the dominant dispersion process, except in the limits as $H/h \to 1$ and $H/h \to \infty$. This is the case regardless of the exchange mechanism. However, a comparison of Figure 4-9 and Figure 4-12 reveals that the maximum dimensionless dispersion rate for is an order of magnitude higher in regimes of diffusion-limited layer exchange than in the case of vortex-driven exchange. This point is clearly illustrated in Figure 4-13, which expresses the total dispersion rates for the two regimes in terms of the traditional boundary layer scaling. Because $Pe_b > 1$, as discussed in §2.8.2, much higher rates of

[2]Although vegetation in mangrove forests usually emergent, they arguably represent a potential extreme upper density limit for submerged vegetation.

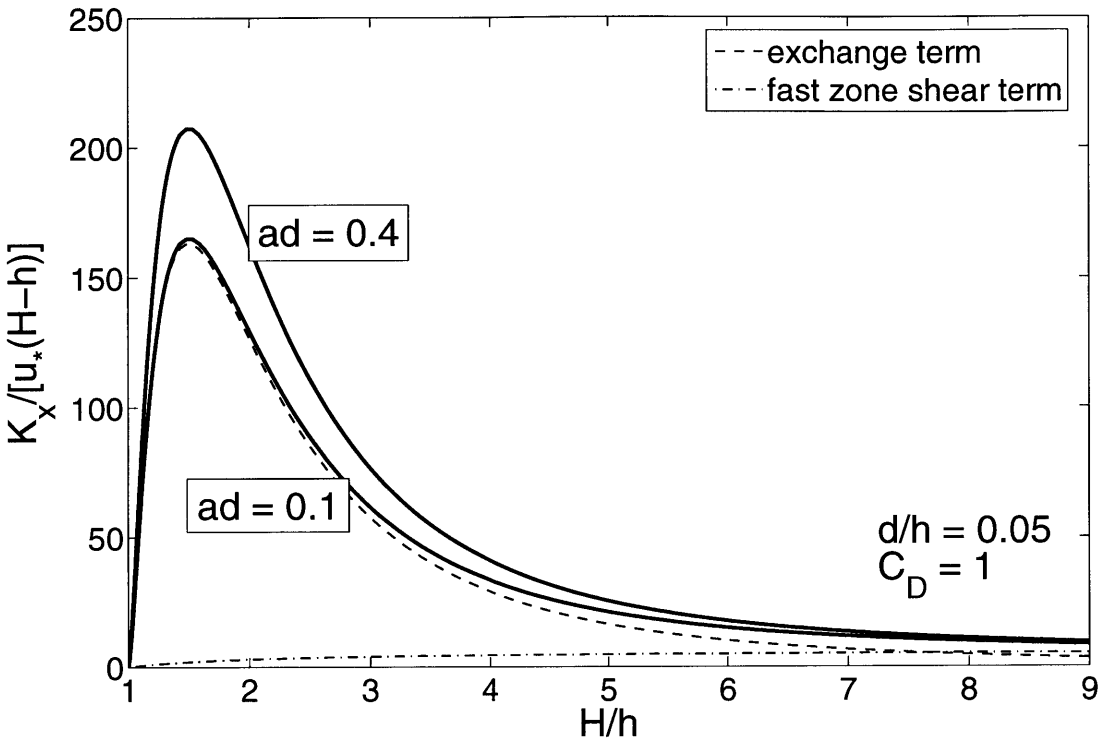

Figure 4-12: Nondimensional dispersion in the regime of diffusion-limited exchange, from (2.91), for typical field conditions. Solid lines represent the total dimensionless dispersion for $ad = 0.1$ and $ad = 0.4$. Broken lines represent the relative contributions of the two terms in (2.91) to the total dispersion for $ad = 0.1$.

dispersion occur in systems where inter-zonal transport is limited to diffusion, causing significant trapping of fluid in the slow zone.

In Figure 4-13, the broken lines represent the dimensionless dispersion when canopy exchange with the overflow is limited to diffusion alone, and the solid line represents the limit of entirely vortex-driven dispersion. In reality, a combination of these exchange mechanisms is likely to occur, such that real dispersion rates will lie in the region bounded by the broken and solid lines. In other words, it will often be the case that neither of the first two terms in (2.74) are negligible.

Since the exchange coefficient is the inverse of the time scale for cross-sectional mixing, $Pe_b = \Delta U h / 40 D_w$ also represents the comparative magnitude of this time scale in the two regimes. $Pe_b > 1$ implies much shorter mixing times for the vortex-driven exchange regime. This point is supported by Figure 4-14, which shows that the

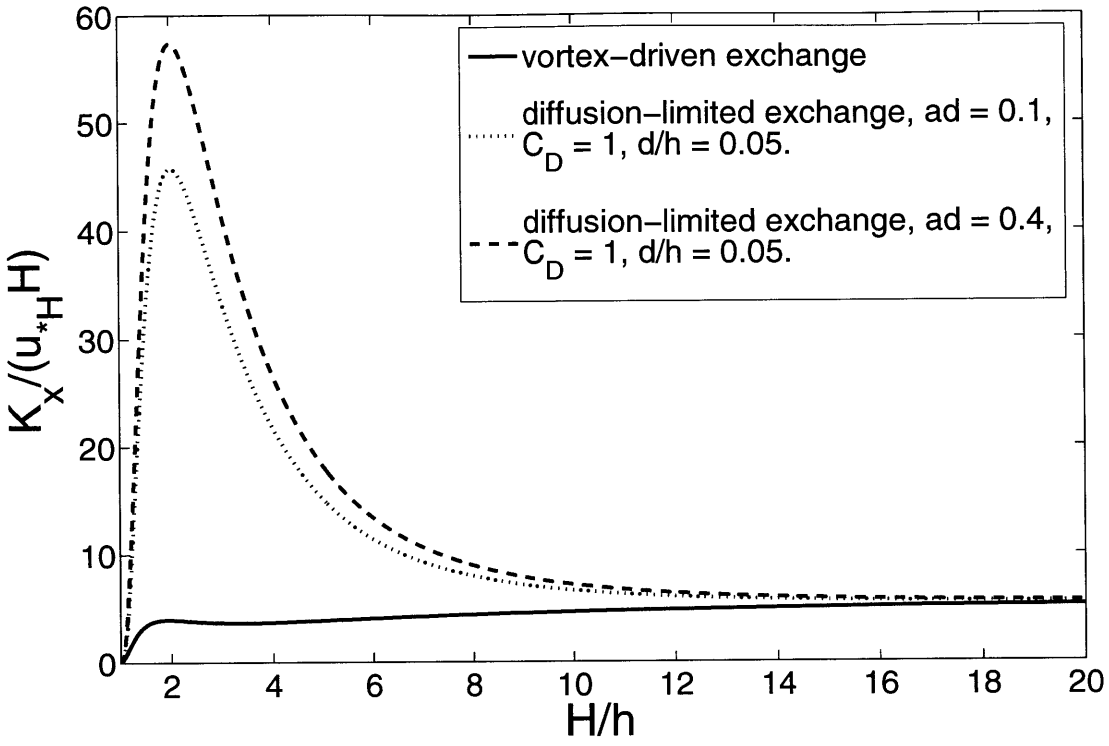

Figure 4-13: Nondimensional dispersion coefficient (with boundary-layer scaling) versus degree of submergence, illustrating enhanced dispersion rates in the regime of diffusion-limited exchange.

Fickian time scale decreases with vortex penetration into the canopy, as the exchange zone occupies more of the flow depth. Thus, even though we expect higher rates of dispersion when vertical exchange is controlled by diffusion, it takes much longer for this dispersive regime to take effect.

4.2 Numerical Model Results

The results of the RWPT model simulations suggest that a more stringent criterion than $t \geq t_{Fick} = 0.4H^2/D_{z,a}$ is required to experimentally determine K_x in vegetated channels. Figure 4-15 shows a model prediction of how the instantaneous dispersion coefficient, $K_x = 0.5\partial\sigma_x^2/\partial t$, is expected to evolve with time for Run I (the solid black line). The dashed line represents the dispersion coefficient that would be obtained from the approximation, $K_x = \frac{\sigma_x^2}{2t}$. At $t = \mu$, this represents the value of

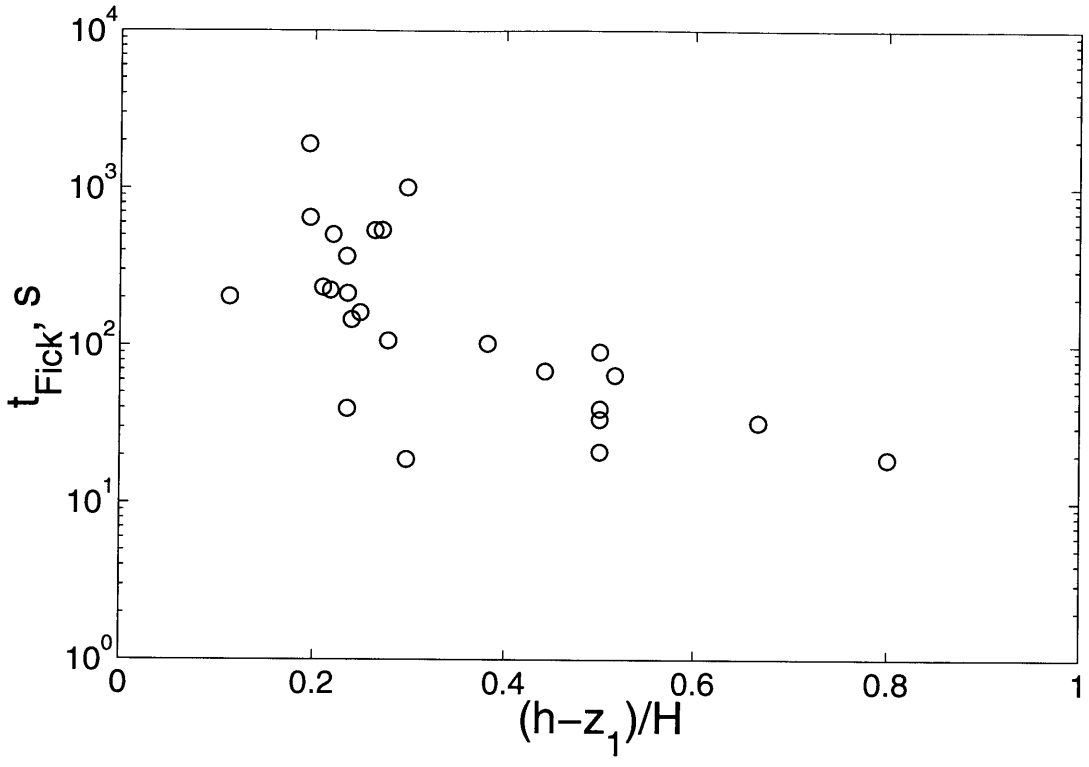

Figure 4-14: The relationship between the Fickian time scale, $t_{Fick} = 0.4H^2/D_{z,a}$, and the proportion of the flow taken up by the exchange zone.

K_x that would be determined from our tracer experiments. We see that the solid line begins to stabilize at $t \simeq t_{Fick}$, indicating that a constant value of K_x has been reached. However, it is not until $t = t_{10\%} \approx 4t_{Fick}$ that the single-point approximation, $K_x = \sigma_x^2/2t$, catches up to the final Fickian value (within 10 % of $K_{x,a}$). This is consistent with Chatwin's [15] proposal that $t = 1.0H^2/D_{z,a}$ is the minimum time scale for an accurate analysis.There are potentially two reasons for this: (i) the depth average D_z in (2.68) underestimates the contribution from zones of significantly reduced diffusivity (this is a resolution issue, as discussed by Thacker [108]), and (ii), concentration measurements at a single location dictate the approximation of (2.66) by $\frac{\sigma_x^2}{2\mu}$, which will remain an inaccurate predictor of K_x until some time after the onset of a Fickian regime. We propose that $t_{10\%}$, the time when the approximation of K_x becomes accurate to 10% (see Figure 4-15), is an appropriate value. Under flow conditions where cross-sectional mixing occurs rapidly (i.e., when $\frac{D_{z,a}}{H^2}$ is rela-

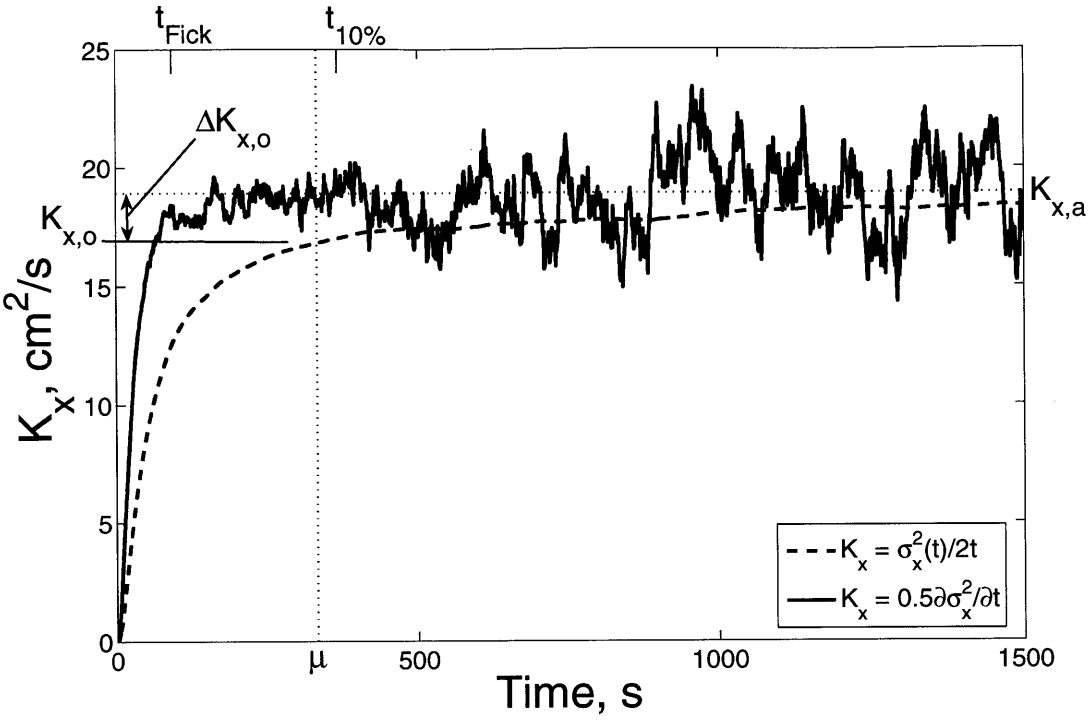

Figure 4-15: Results from the RWPT model simulation of Run A2. At $t = \mu$, the approximation $K_x = K_{x,o} = \frac{\sigma_x^2}{2\mu}$ underestimates the asymptotic value of $K_x = K_{x,a}$. Although the regime is Fickian at this point (i.e., $\mu > t_{Fick} = 0.4\frac{H^2}{D_{z,a}}$ such that the solid line, $K_x = 0.5\partial\sigma_x^2/\partial t$, has reached an approximately constant value of $K_{x,a}$), insufficient time has elapsed for $K_x = K_{x,o}$ to be an accurate approximation. For this particular run, $\Delta K_{x,o} = 2\text{cm}^2/\text{s}$, such that the experimentally determined dispersion coefficient is expected to underestimate the final Fickian value by 11%.

tively large), $t_{10\%} \gg t_{Fick} = 0.4\frac{H^2}{D_{z,a}}$. This corresponds to large $\partial K_x/\partial t$ at short times, and a sharp transition to linear growth of variance at about $t = t_{Fick}$. Such rapid growth in the near-field variance does not immediately propagate to the single-point approximation (the dashed line in Figure 4-15). A delayed response means that the single-point approximation does not become accurate until much later, such that $t_{10\%}$ is significantly different from t_{Fick}. However, for very low vertical mixing rates, early growth in K_x is so slow that the single-point approximation keeps up and $t_{10\%} \approx t_{Fick}$. This conceptual argument supports the empirical relationship between the two time scales, shown in Figure 4-16.

Because $\mu < t_{10\%}$ for many of the experimental runs (see Table 4.3), it is likely

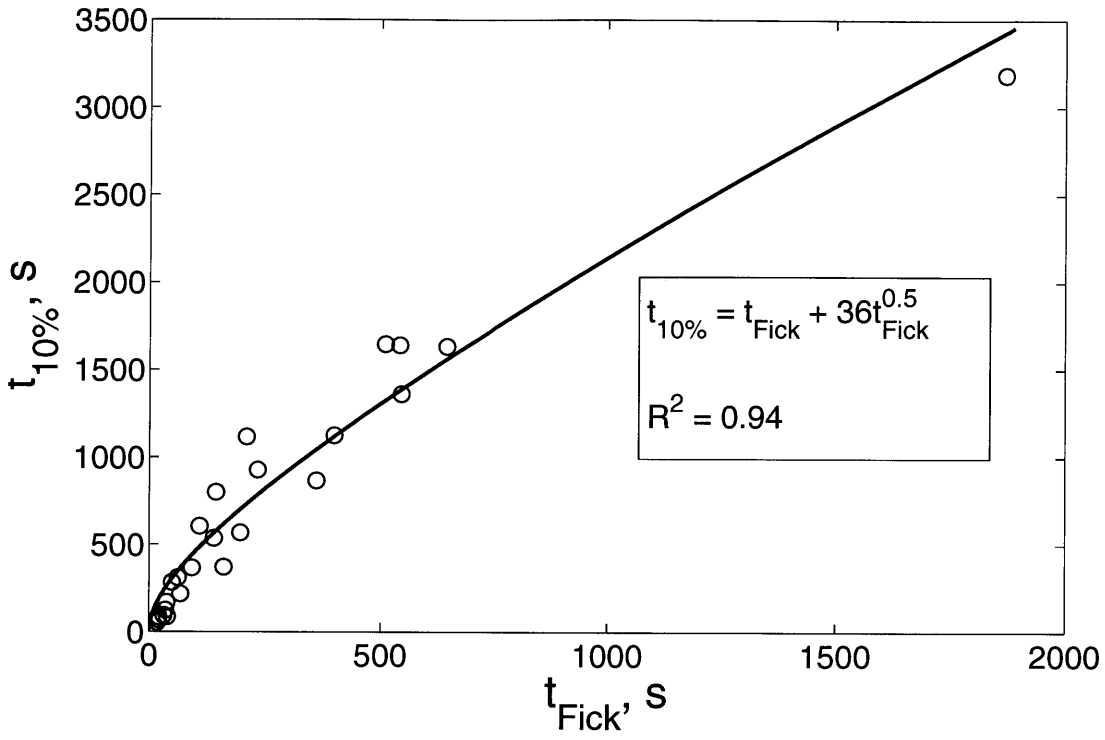

Figure 4-16: Regression and statistics of the fit relating $t_{10\%}$ to the Fickian time scale, $t_{Fick} = 0.4H^2/D_{z,a}$.

that K_x values obtained from $\frac{\sigma_x^2}{2\mu}$ are underestimates of the final Fickian values. Based on a single RWPT model simulation for each run, we expect underestimations of 5% to, in a few cases, as much as 45%. If the experimental values of K_x are adjusted upwards accordingly ($K_{x,NL}$ in Table 4.3), the best fit of (2.84) yields $\beta = 116 \pm 15$ with 95% confidence. If no fitting parameter is used, and dispersion coefficients for the experimental runs are calculated directly by substituting measured values of U_1, U_2, and $b = \Delta U/40h$ into (2.72), we see that the values obtained are higher than those observed (pluses in Figure 4-17). However, upward adjustment of the observed K_x values results in much better agreement, by which we mean that the line of equivalence runs through the data (circles) in Figure 4-17.

The RWPT simulations were used to assess the suitability of the mean tracer velocity, the skewness coefficient and the kurtosis excess as indicators of proximity to the Fickian limit. Figure 4-18 shows the evolution of particle distributions in the

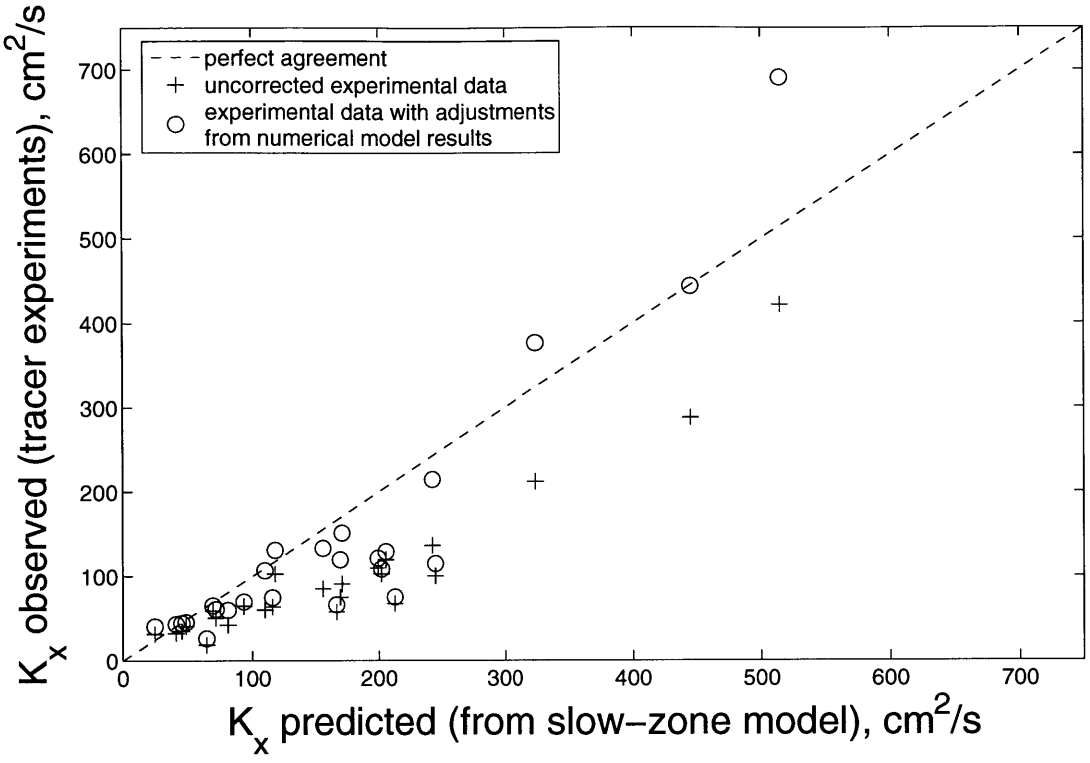

Figure 4-17: Agreement between dispersion coefficients obtained from the two-zone model and experimental results, before and after adjustment with RWPT model results. Two-zone model estimates are made using measured velocity profiles.

RWPT simulation of run B6 (corresponding to the experimental run of the same label). All length scales have been normalized by the depth, $H = 29.75$ cm. For this particular run, $z_1/H = 0$, such that the diffusivity was constant with depth. 10,000 particles were introduced at $z/H = h/H = 0.24$ (point A in Figure 4-18a) at $t = 0$. Figure 4-18b and c show that at $x/H = 3.5$, the particles are not well-mixed over depth but accumulate close to the bed in regions of low velocity. This is simply a result of the position of the source below mid-depth at $t = 0$. The depth-average distribution is clearly not Gaussian at this point. There are two peaks in the longitudinal particle density: The first, closest to $x/H = 0$ represents the majority of the particles in low velocities close to $z/H = 0$; The second peak represents the faster-moving particles close to $z/H = 1$. As shown by Figure 4-18c, the particles become well-mixed over depth with an increasing number of time steps and the depth-average particle density looks more Gaussian (Figure 4-18b).

The fluorometer location in the corresponding tracer experiment was at $x/H = 38$, where one would expect to sample a reasonably well-mixed concentration distribution based on this RWPT simulation. However, the traditional Fickian limit prediction based on $\tilde{t} = 0.4$ predicts a well-mixed cloud at $x/H = 10$. The RWPT shows that a Gaussian distribution is unlikely at this early stage. The evolution of typical indicators of Fickian behavior are shown in Figure 4-19. Although the mean velocity of the particles is within 10 % of the channel velocity at $x/H = 10$, deviations greater than 25 % are never observed even at very early stages in the evolution of the particle plume. This supports the argument made in §4.1, that U_c/U is most indicative of the source location, and is not a good metric for establishing Fickian behavior unless the initial condition is a well-mixed distribution. Both the skewness coefficient, G (Figure 4-19b), and kurtosis excess, κ_e (Figure 4-19c), approach zero at $x/H \rightarrow \infty$ as expected. However, the convergence is so slow that they too are unlikely to provide useful practical measures of Fickian conditions. Even at $x/H = 100$ (or 10 times the distance of the Fickian limit that we would predict), $G < -2$ and $\kappa_e > 2$. In field conditions, this will be compounded by the fact that G and κ are sensitive to outlying concentrations. Dead-zone residence times are likely to be too long for all tracer mass to be recovered in real situations, resulting in underestimations of the mass in the tails of distributions. This will impact significantly on observed higher order moments, rendering G and κ_e inaccurate.

Figures 4-20 and 4-21 show the results of the simulation of run A3. In this simulation, $H = 10.5$ cm, $z_1/H = 0.4$, and $h/H = 0.7$ (point A in Figure 4-20a). The diffusivity profile was a step, with $D_z = 0.43\,\mathrm{cm}^2/\mathrm{s}$ over $z_1 < z < H$ and $D_z = 0.14\,\mathrm{cm}^2/\mathrm{s}$ for $0 < z < z_1$. Figure 4-20c shows that at $x/H = 3.5$, the particles are not mixed uniformly over the total depth. The majority reside in $z/H > z_1/H$, since they were introduced at $z/H = 0.7$ and rapid mixing has caused them to become uniformly distributed over the upper portion of the flow. The depth-average particle distribution exhibits a distinct double peak, as with run B6 previously. With progressive time steps, the particles in the faster-flowing region slowly diffuse down into the zone of lower diffusivity ($z/H < z_1/H$), as evident from Figure 4-20c at

$x/H = 35$ and $x/H = 105$. A spike in the particle density is observed just below $z/H = z_1/H$ at these longitudinal distances. This corresponds to particles that have just arrived in the zone of lower diffusivity and have not had sufficient time to mix fully over $0 < z < z_1$. This spike becomes less pronounced at greater distances downstream as the particle density approaches uniformity with depth.

The Fickian criterion $\tilde{t} = 0.4$ would predict a Gaussian distribution of well-mixed particles at $x/H \simeq 46$ for this simulation. However, even at $x/H = 105$ (corresponding to $\tilde{t} \simeq 0.9$), the distribution is negatively skewed and not quite uniform over depth (Figures 4-21b and 4-20c, respectively). Also, because of the asymptotic approach of G to zero, skewnesses of $O(1)$ are likely to be observed for very large values of x/H. Therefore, G is of no real practical use as an indicator of Fickian conditions. κ_e on the other hand, approaches zero quite sharply in this case (Figure 4-21c) and could have practical applications, were it not for the sensitivity to outliers discussed previously. As for run B6, the mean tracer velocity in run A3 provides little useful information about the Fickian limit, due to a very gradual approach to the mean channel velocity. The interesting point to note is that $U_c/U \rightarrow 1$ from $U_c/U > 1$ (see Figure 4-21a). This is the exact opposite to the behavior in run B6, where U_c/U converges to 1 from below. This rules out the use of U_c/U as a Fickian criterion, as suggested by [21], when point sources are being considered. As the authors suggest, however, this parameter does give an indication of how much time the tracer has spent in dead zones versus fast zones. For example, regardless of the injection location, a tracer plume with $U_c/U > 1$ must have spent the majority of its time in faster regions of the flow field. Similarly, $U_c/U < 1$ implies a bias towards dead zones.

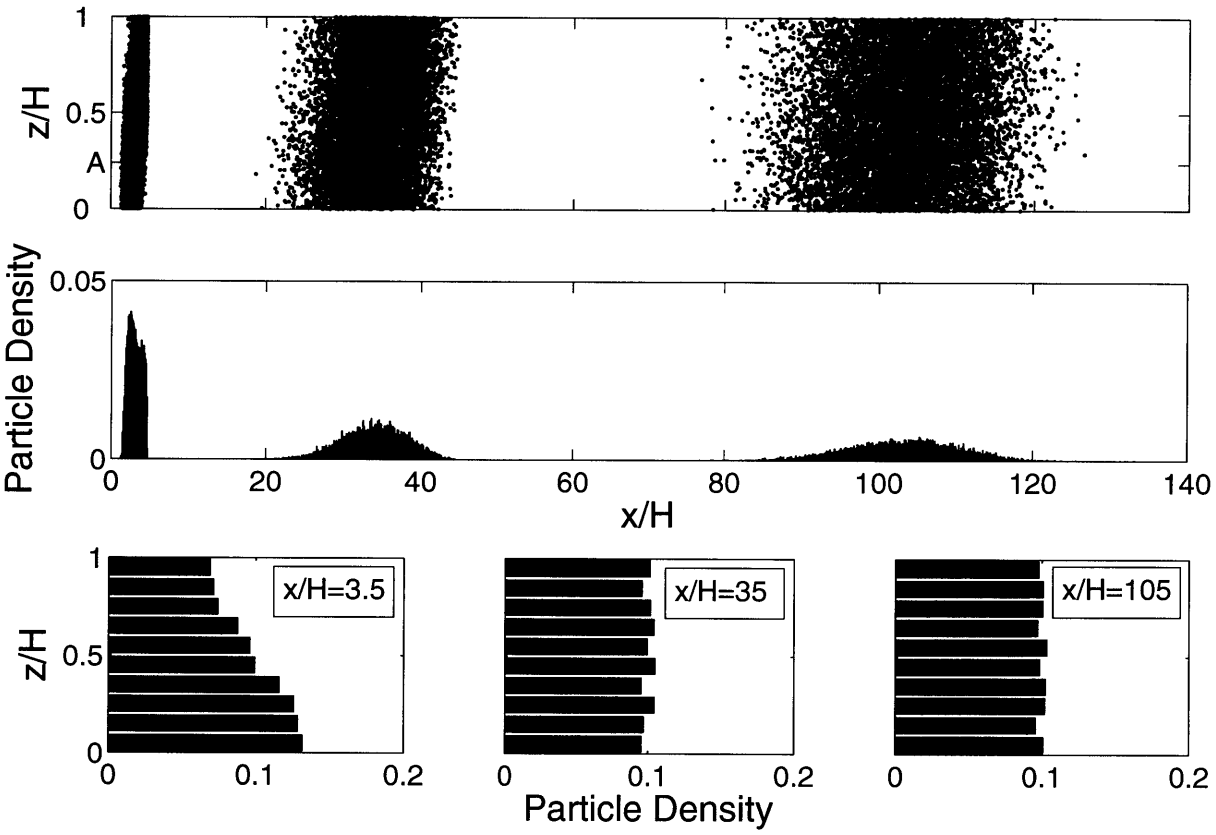

Figure 4-18: RWPT simulation results for run B6 after 14, 141 and 423 time steps (i.e., at $\tilde{t} = 0.35$, 3.5, and 10). (a) Particle positions - point A shows the location of the particle source at $t = 0$; (b) Particle density in the longitudinal direction; (c) Particle density in the vertical direction. Fickian conditions would be expected at $x/H = 10$ based on $t_{Fick} = 0.4H^2/D_{z,a}$.

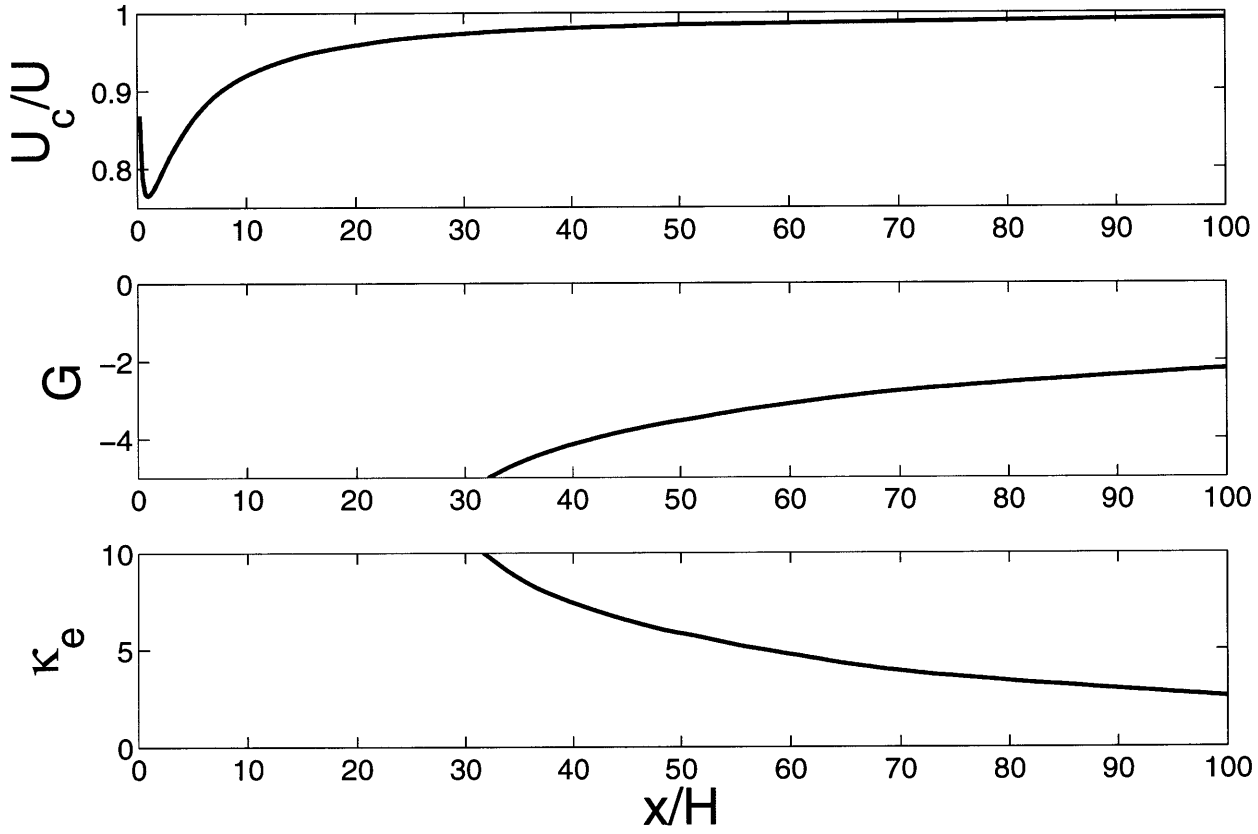

Figure 4-19: Evolution of particle statistics in the RWPT simulation of run B6. (a) Mean transport velocity of particles U_c, normalized by the mean channel velocity, U; (b) Skewness coefficient, G; (c) Kurtosis excess, κ_e. Fickian conditions would be expected at $x/H = 10$ based on $x/H = 10$ based on $t_{Fick} = 0.4H^2/D_{z,a}$.

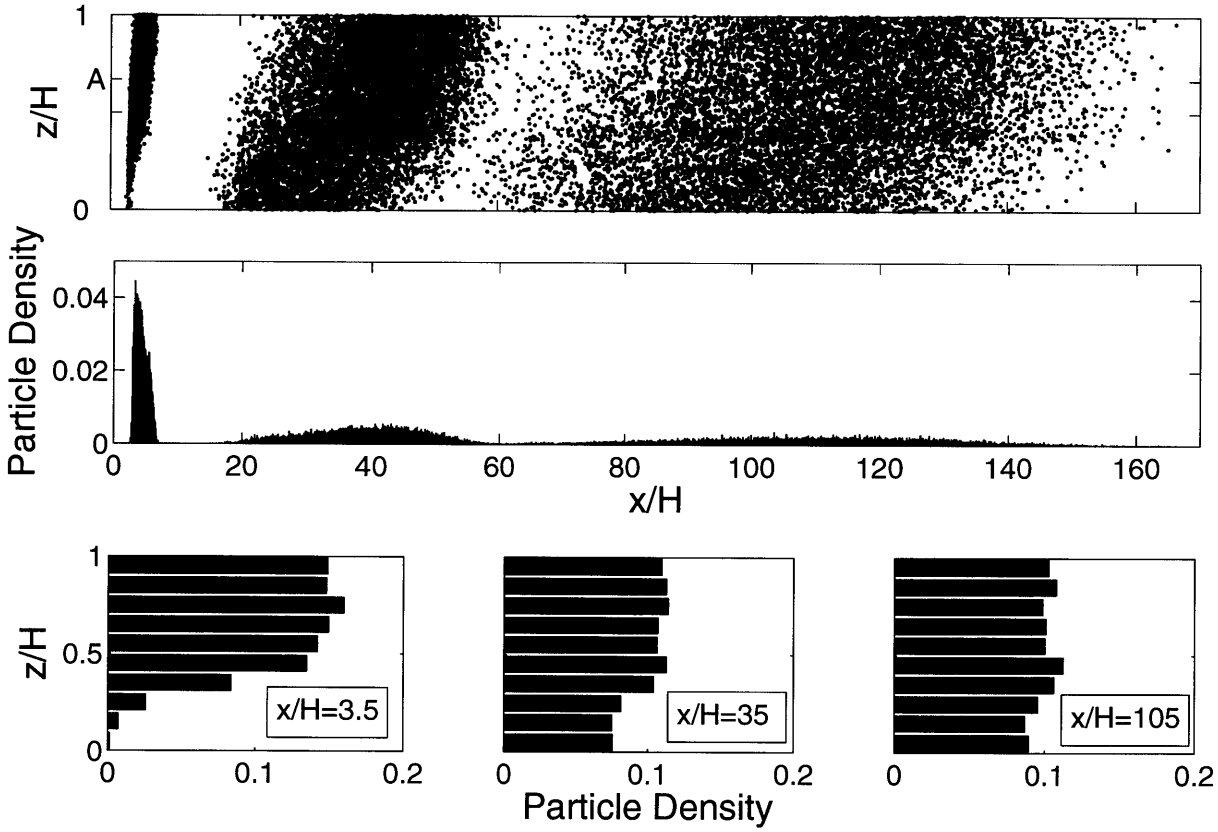

Figure 4-20: RWPT simulation results for run A3 after 10, 104 and 312 time steps (i.e., at $\tilde{t} = 0.1$, 0.7, and 2.2). (a) Particle positions - point A shows the location of the particle source at $t = 0$; (b) Particle density in the longitudinal direction; (c) Particle density in the vertical direction. Fickian conditions would be expected at $x/H = 46$ based on $t_{Fick} = 0.4H^2/D_{z,a}$.

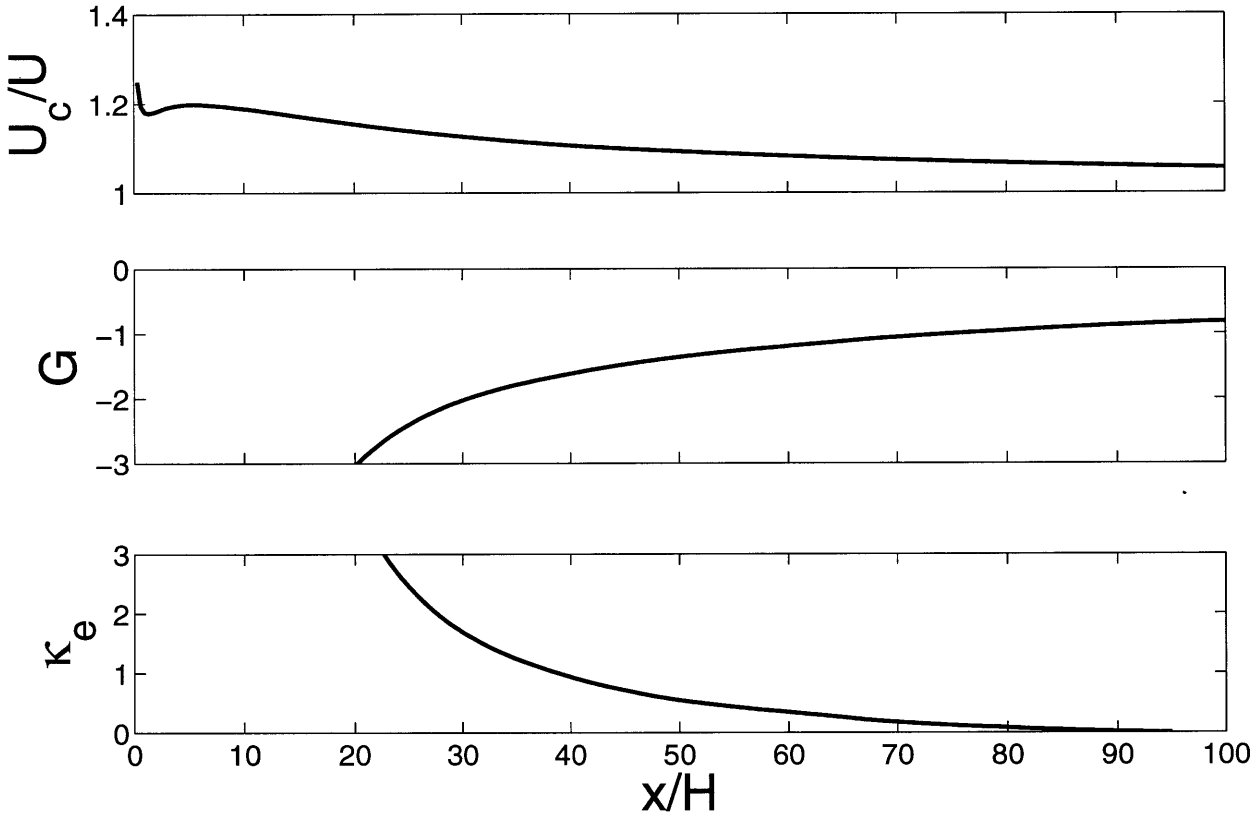

Figure 4-21: Evolution of particle statistics in the RWPT simulation of run A3. (a) Mean transport velocity of particles U_c, normalized by the mean channel velocity, U; (b) Skewness coefficient, G; (c) Kurtosis excess, κ_e. Fickian conditions would be expected at $x/H = 46$ based on $t_{Fick} = 0.4H^2/D_{z,a}$.

Chapter 5

Conclusion

A theoretical framework for evaluating the longitudinal dispersion coefficient in vegetated flows is proposed. A two-zone model is presented, which identifies three contributory processes: large-scale shear dispersion above the canopy, inefficient exchange between the vegetated layer and the overflow, and stem-scale dispersion within the vegetation. Exchange between the zones is governed by K-H vortices for $C_D ah \ll 2$, and by in-canopy turbulent diffusion for $2 < C_D ah$.

For vortex-driven exchange, the dispersion coefficient is expressed in terms of easily measured parameters, such as the water depth, the overflow friction velocity, u_*, and the height of the vegetation. Inefficient exchange between the zones and logarithmic shear in the fast zone dominate dispersion in this regime. A transition from exchange-driven dispersion to logarithmic-shear dispersion is observed at $H/h \simeq 3$.

When vortex penetration is limited and canopy exchange is dominated by wake-zone diffusion, prediction of K_x requires additional knowledge of canopy morphology parameters, such as a, C_D and d. Delayed exchange between the layers is again the primary mechanism for dispersion, except in the extreme limits of $H/h \to \infty$ and $H/h \to 1$. Logarithmic dispersion in the fast zone does not become the dominant dispersive process until approximately $H/h > 8$. The overall dispersion is an order of magnitude greater than in the case of vortex-driven exchange. Further work and additional experiments are required to validate the two-zone model in this regime.

The traditional expression for the Fickian time scale is shown by a numerical

model to be reasonably accurate in predicting cross-sectional mixing. However, this time scale is not long enough to allow K_x to be accurately determined from tracer studies. A new time scale is proposed here.

A random walk, particle-tracking (RWPT) model was developed in Netlogo to simulate dispersion in vegetated flows. This will be a useful tool in the future for investigating residence times, sedimentation, and solute uptake in channels containing submerged vegetation.

Appendix A

Concentration-Time Distributions

Plots of normalized concentration versus time for all twenty-eight tracer experiments. As discussed in Chapter 4, the time and concentration axes have been normalized by the mean arrival time (μ) and the total recovered mass of the solute (M_0), respectively.

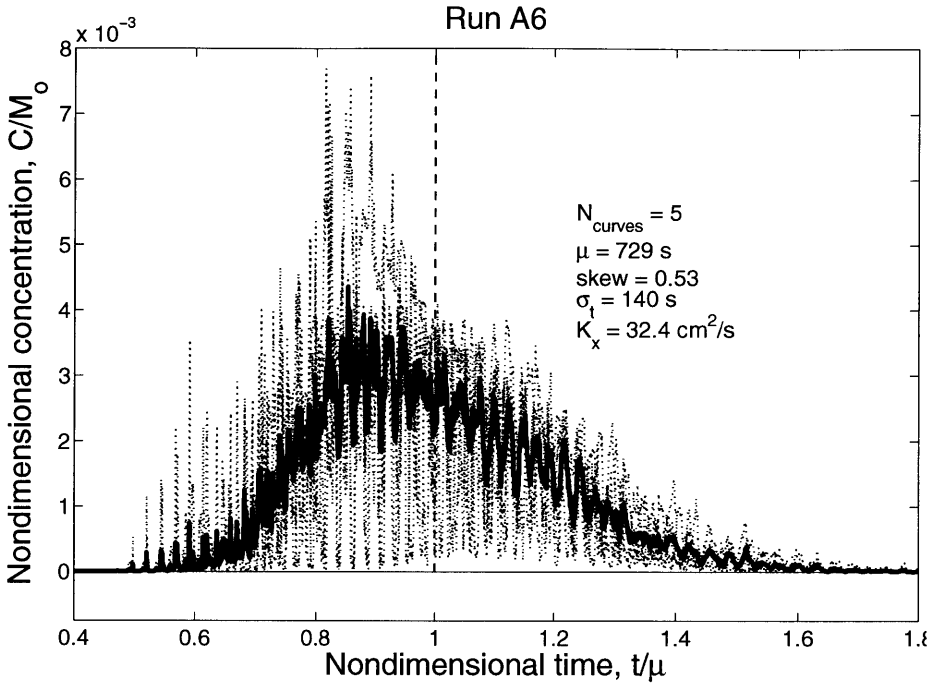
Run A6
x 10^-3
Nondimensional concentration, C/M_o
N_curves = 5
μ = 729 s
skew = 0.53
σ_t = 140 s
K_x = 32.4 cm^2/s
Nondimensional time, t/μ

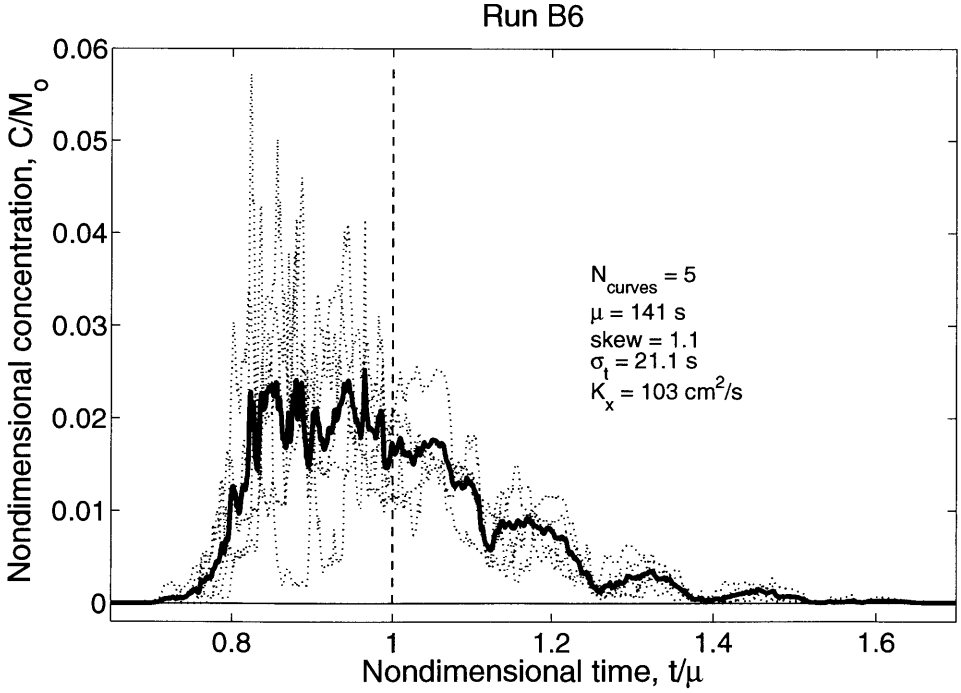
Run B6
Nondimensional concentration, C/M_o
N_curves = 5
μ = 141 s
skew = 1.1
σ_t = 21.1 s
K_x = 103 cm^2/s
Nondimensional time, t/μ

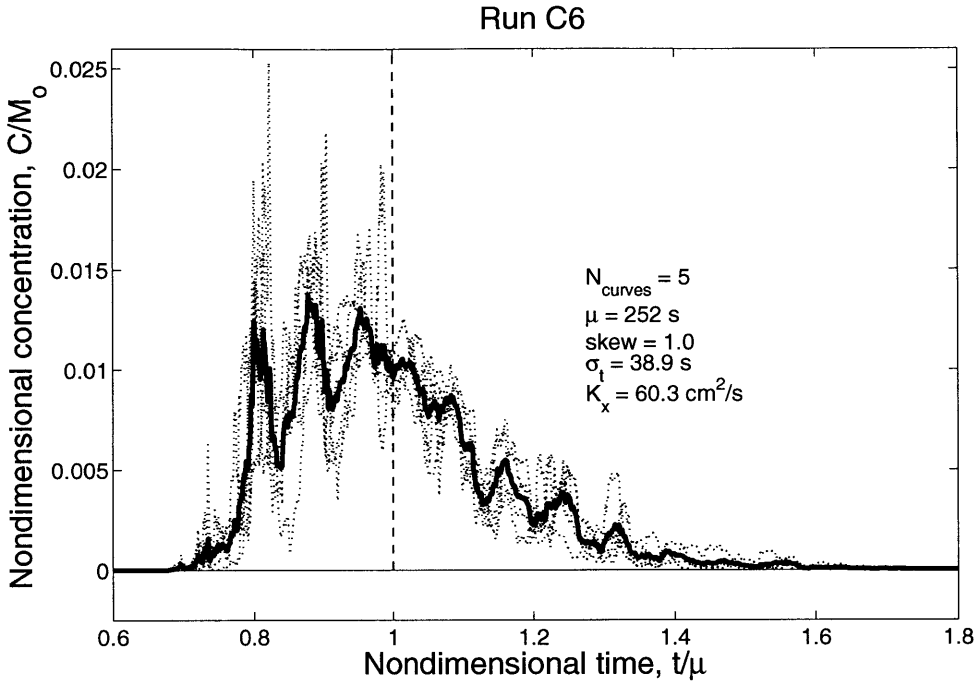
Run C6
Nondimensional concentration, C/M$_o$
0.025
0.02
0.015
0.01
0.005
0
N$_{curves}$ = 5
μ = 252 s
skew = 1.0
σ$_t$ = 38.9 s
K$_x$ = 60.3 cm^2/s
0.6
0.8
1
1.2
1.4
1.6
1.8
Nondimensional time, t/μ

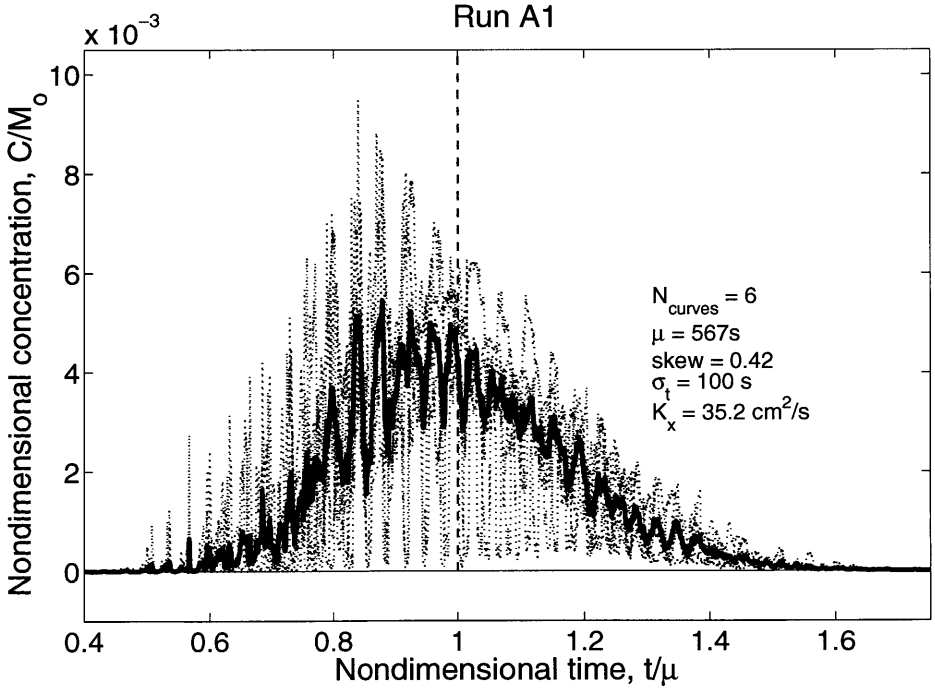
Run A1
x 10^{-3}
Nondimensional concentration, C/M$_o$
10
8
6
4
2
0
N$_{curves}$ = 6
μ = 567s
skew = 0.42
σ$_t$ = 100 s
K$_x$ = 35.2 cm^2/s
0.4
0.6
0.8
1
1.2
1.4
1.6
Nondimensional time, t/μ

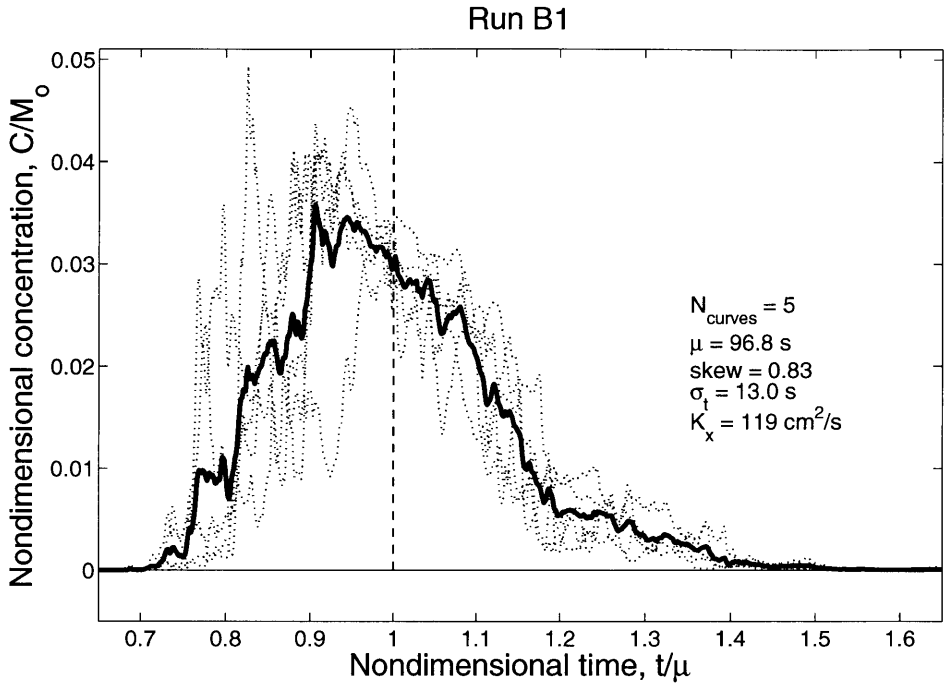
Run B1
Nondimensional concentration, C/M$_o$
0.05
0.04
0.03
0.02
0.01
0
0.7
0.8
0.9
1
1.1
1.2
1.3
1.4
1.5
1.6
Nondimensional time, t/μ
N$_{curves}$ = 5
μ = 96.8 s
skew = 0.83
σ$_t$ = 13.0 s
K$_x$ = 119 cm^2/s

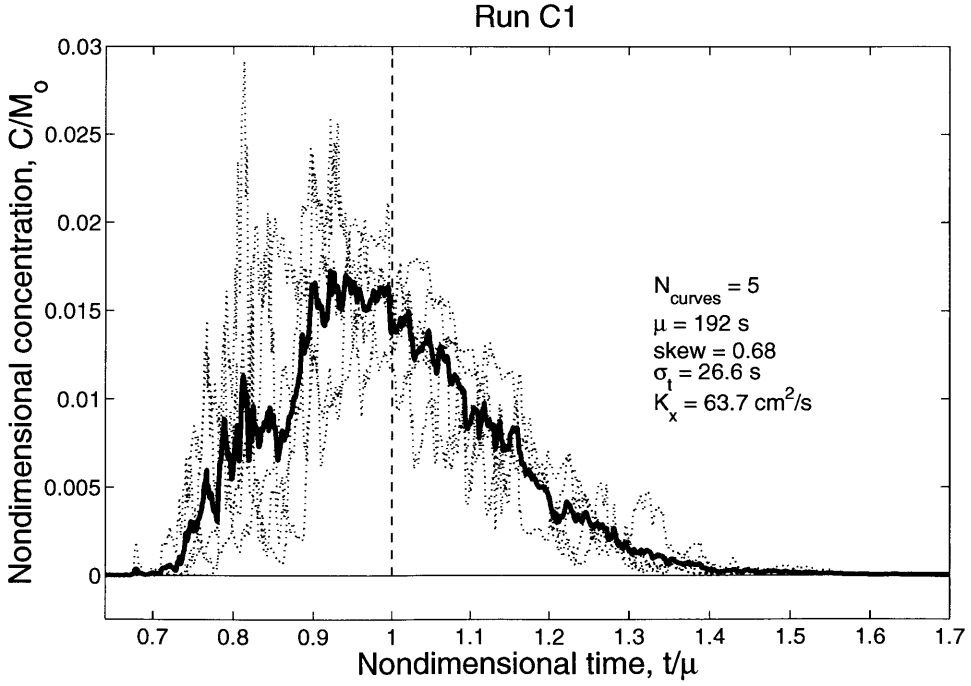
Run C1
Nondimensional concentration, C/M$_o$
0.03
0.025
0.02
0.015
0.01
0.005
0
0.7
0.8
0.9
1
1.1
1.2
1.3
1.4
1.5
1.6
1.7
Nondimensional time, t/μ
N$_{curves}$ = 5
μ = 192 s
skew = 0.68
σ$_t$ = 26.6 s
K$_x$ = 63.7 cm^2/s

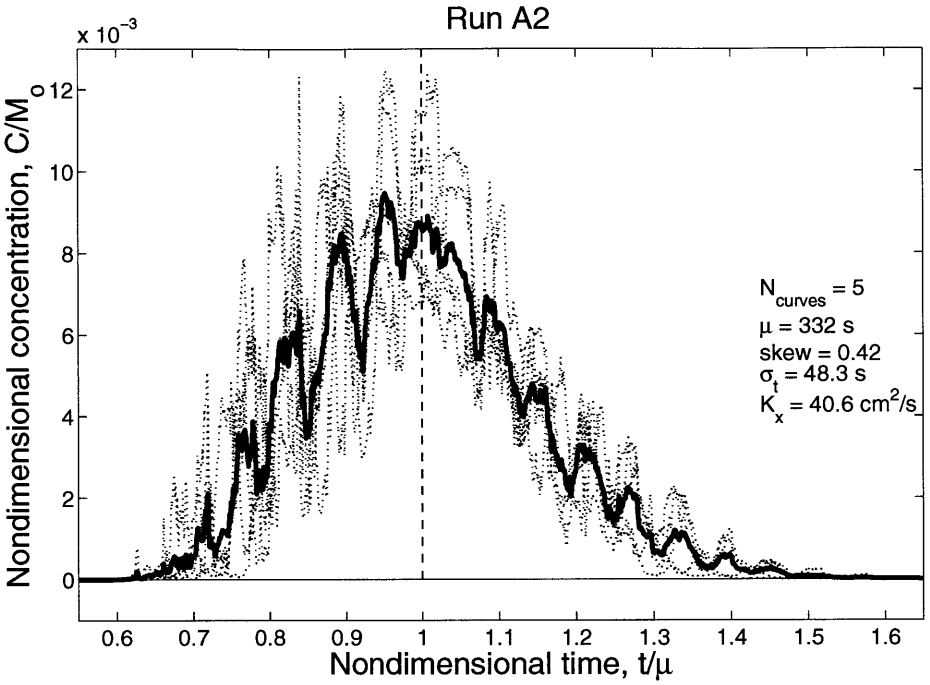
Run A2
x 10^-3
Nondimensional concentration, C/M_o
Nondimensional time, t/μ
N_curves = 5
μ = 332 s
skew = 0.42
σ_t = 48.3 s
K_x = 40.6 cm^2/s

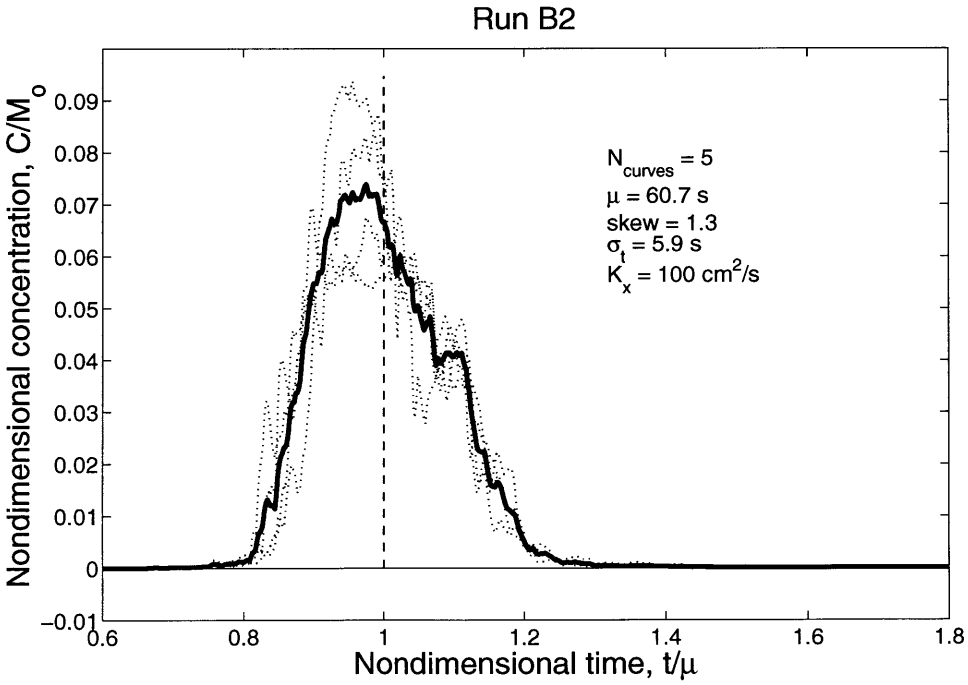
Run B2
Nondimensional concentration, C/M_o
Nondimensional time, t/μ
N_curves = 5
μ = 60.7 s
skew = 1.3
σ_t = 5.9 s
K_x = 100 cm^2/s

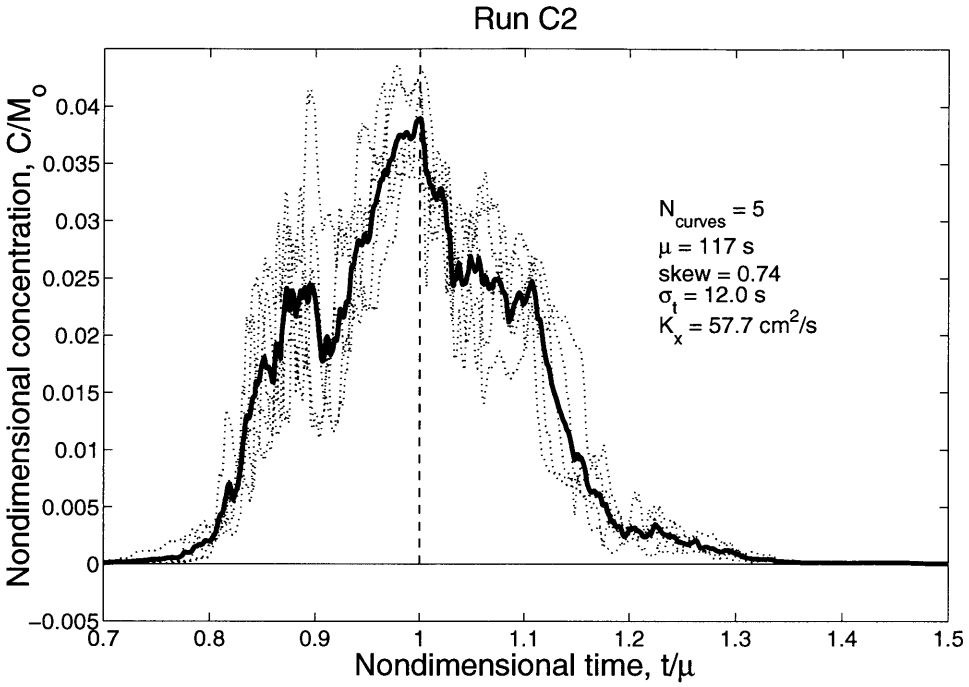
Run C2
Nondimensional concentration, C/M$_o$
0.04
0.035
0.03
0.025
0.02
0.015
0.01
0.005
0
−0.005
0.7
0.8
0.9
1
1.1
1.2
1.3
1.4
1.5
Nondimensional time, t/μ
N$_{curves}$ = 5
μ = 117 s
skew = 0.74
σ$_t$ = 12.0 s
K$_x$ = 57.7 cm^2/s

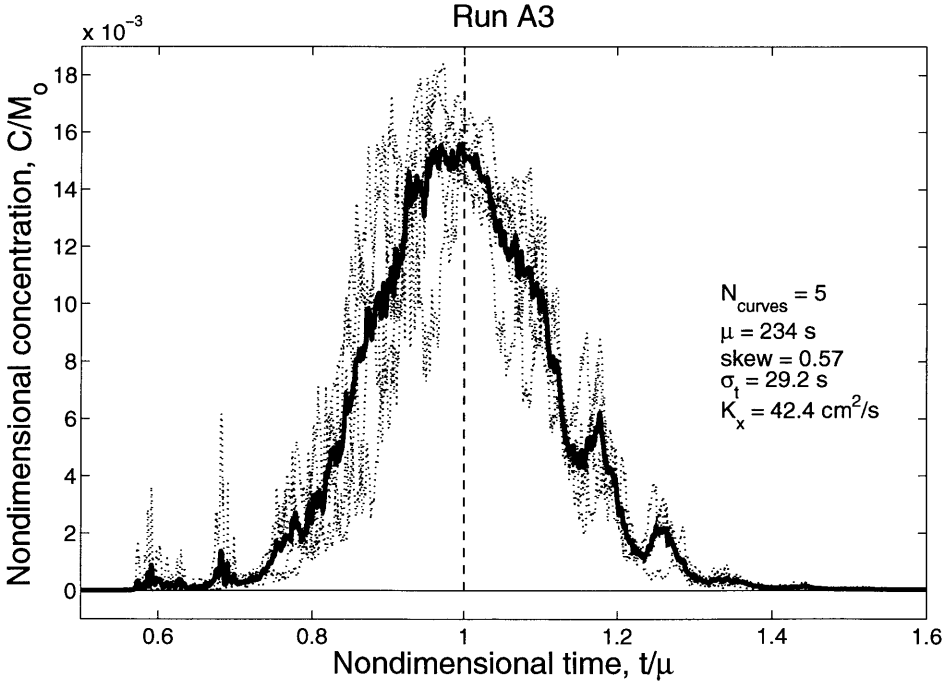
Run A3
x 10^{-3}
Nondimensional concentration, C/M$_o$
18
16
14
12
10
8
6
4
2
0
0.6
0.8
1
1.2
1.4
1.6
Nondimensional time, t/μ
N$_{curves}$ = 5
μ = 234 s
skew = 0.57
σ$_t$ = 29.2 s
K$_x$ = 42.4 cm^2/s

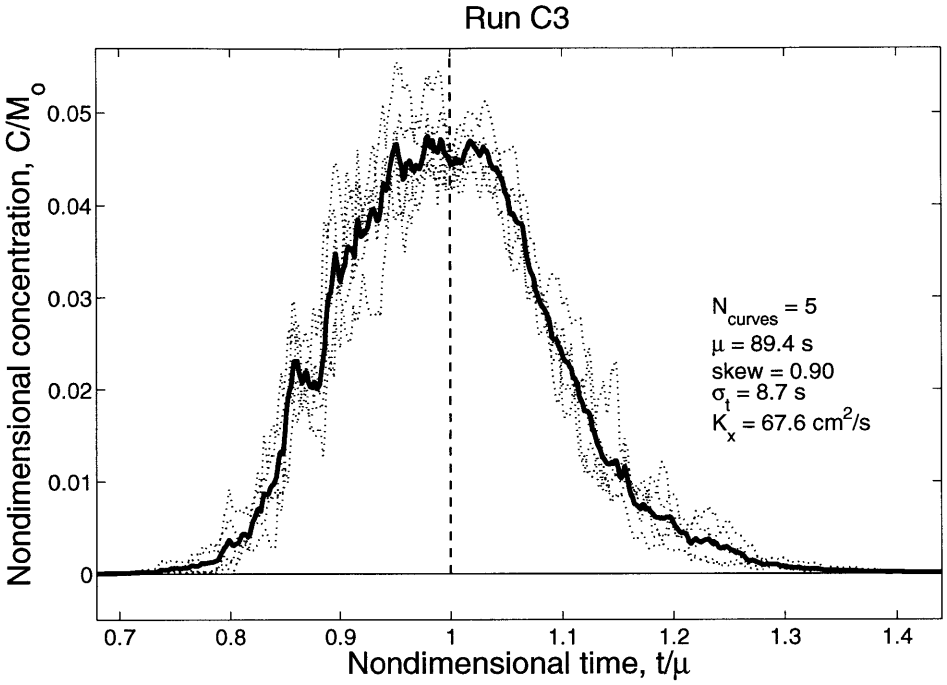
Run C3
Nondimensional concentration, C/M$_o$
0.05
0.04
0.03
0.02
0.01
0
0.7
0.8
0.9
1
1.1
1.2
1.3
1.4
Nondimensional time, t/μ
N$_{curves}$ = 5
μ = 89.4 s
skew = 0.90
σ$_t$ = 8.7 s
K$_x$ = 67.6 cm^2/s

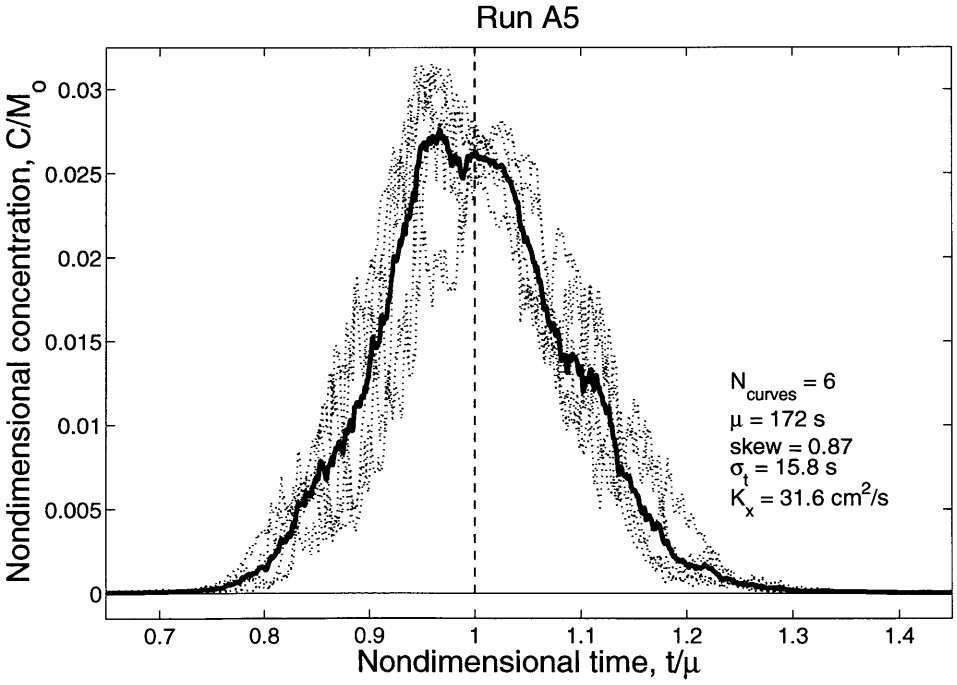
Run A5
Nondimensional concentration, C/M$_o$
0.03
0.025
0.02
0.015
0.01
0.005
0
0.7
0.8
0.9
1
1.1
1.2
1.3
1.4
Nondimensional time, t/μ
N$_{curves}$ = 6
μ = 172 s
skew = 0.87
σ$_t$ = 15.8 s
K$_x$ = 31.6 cm^2/s

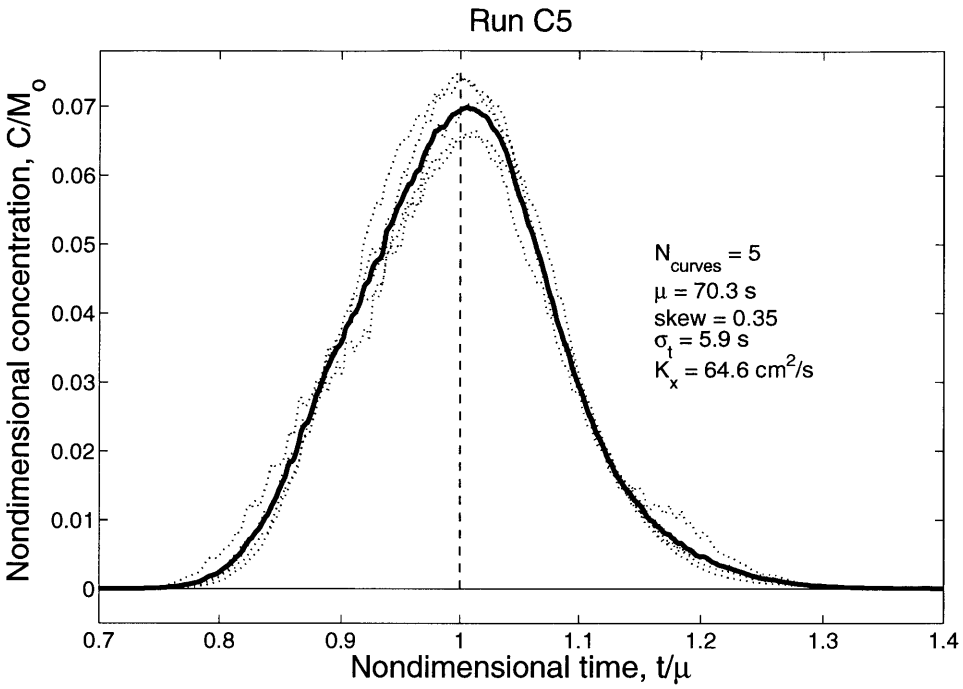
Run C5
Nondimensional concentration, C/M$_o$
0.07
0.06
0.05
0.04
0.03
0.02
0.01
0
0.7
0.8
0.9
1
1.1
1.2
1.3
1.4
Nondimensional time, t/μ
N$_{curves}$ = 5
μ = 70.3 s
skew = 0.35
σ$_t$ = 5.9 s
K$_x$ = 64.6 cm^2/s

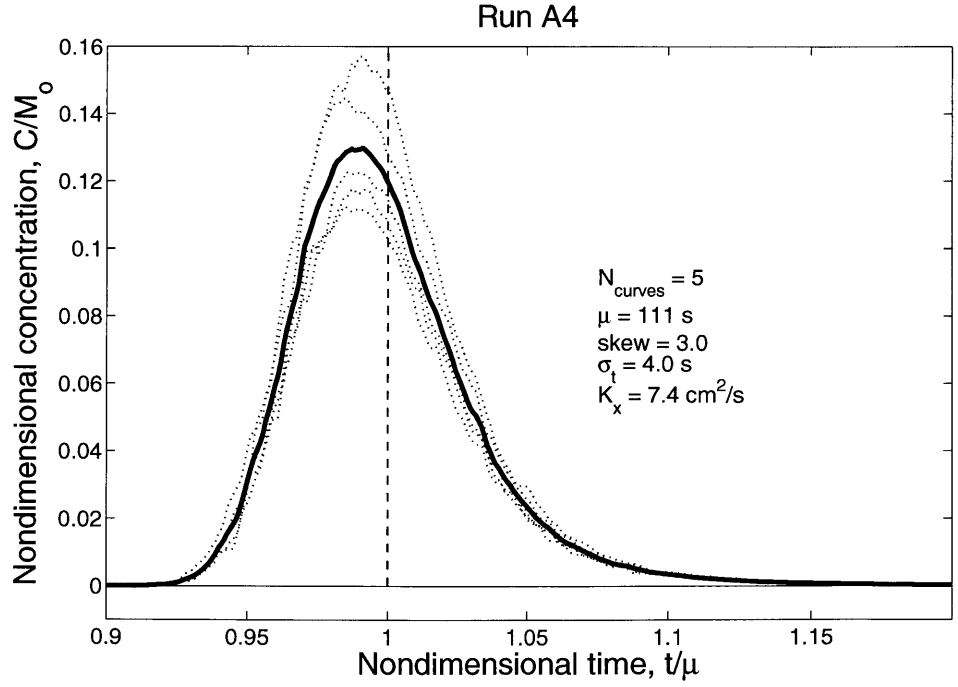
Run A4
Nondimensional concentration, C/M$_o$
0.16
0.14
0.12
0.1
0.08
0.06
0.04
0.02
0
0.9
0.95
1
1.05
1.1
1.15
Nondimensional time, t/μ
N$_{curves}$ = 5
μ = 111 s
skew = 3.0
σ$_t$ = 4.0 s
K$_x$ = 7.4 cm^2/s

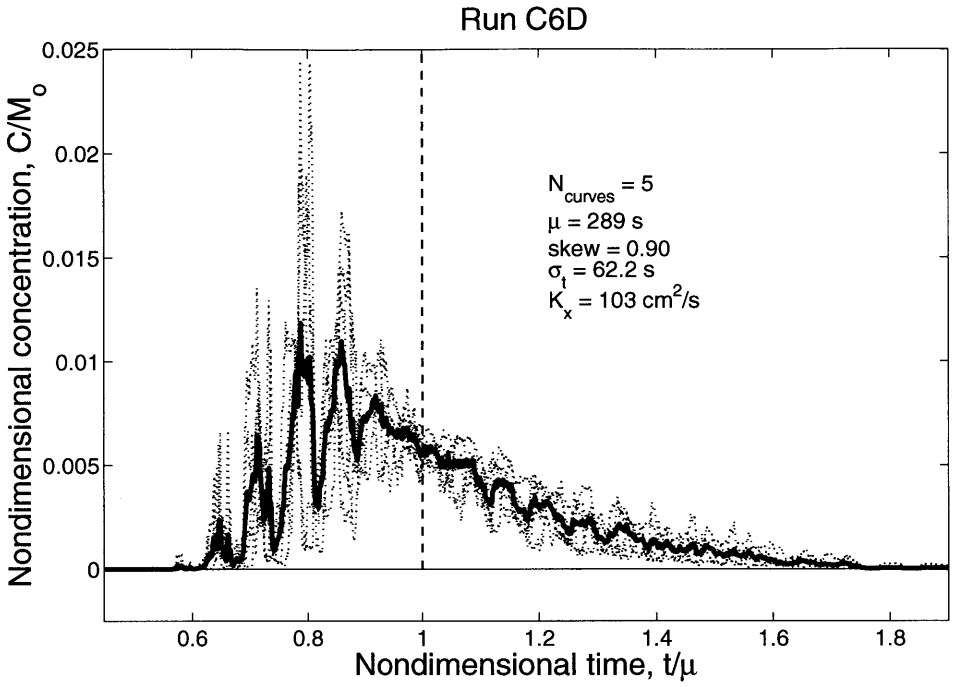
Run C6D
Nondimensional concentration, C/M$_o$
0.025
0.02
0.015
0.01
0.005
0
N$_{curves}$ = 5
μ = 289 s
skew = 0.90
σ$_t$ = 62.2 s
K$_x$ = 103 cm^2/s
0.6
0.8
1
1.2
1.4
1.6
1.8
Nondimensional time, t/μ

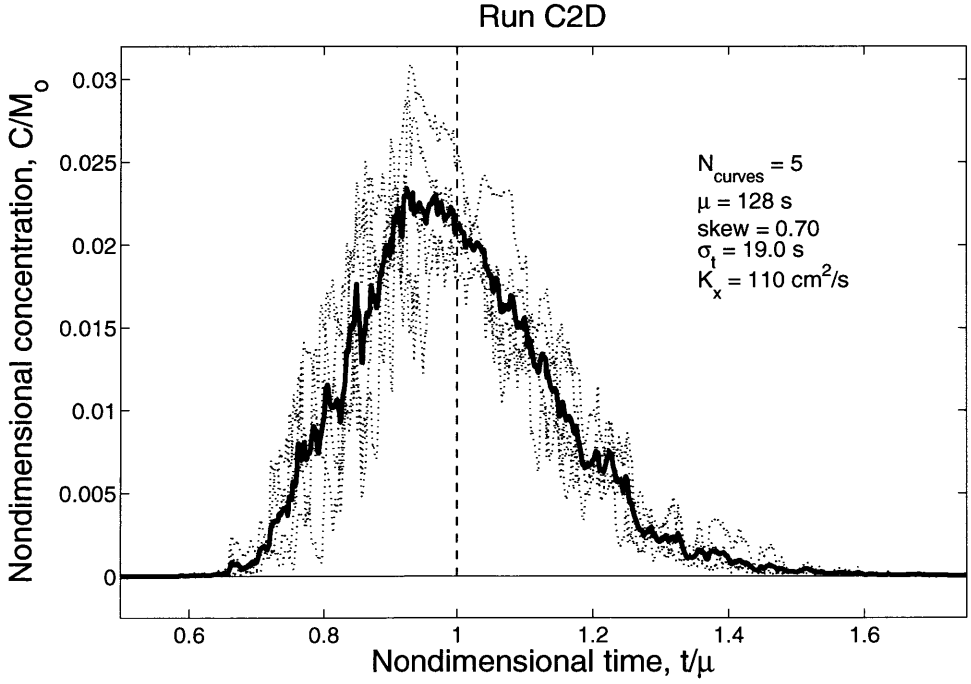
Run C2D
Nondimensional concentration, C/M$_o$
0.03
0.025
0.02
0.015
0.01
0.005
0
N$_{curves}$ = 5
μ = 128 s
skew = 0.70
σ$_t$ = 19.0 s
K$_x$ = 110 cm^2/s
0.6
0.8
1
1.2
1.4
1.6
Nondimensional time, t/μ

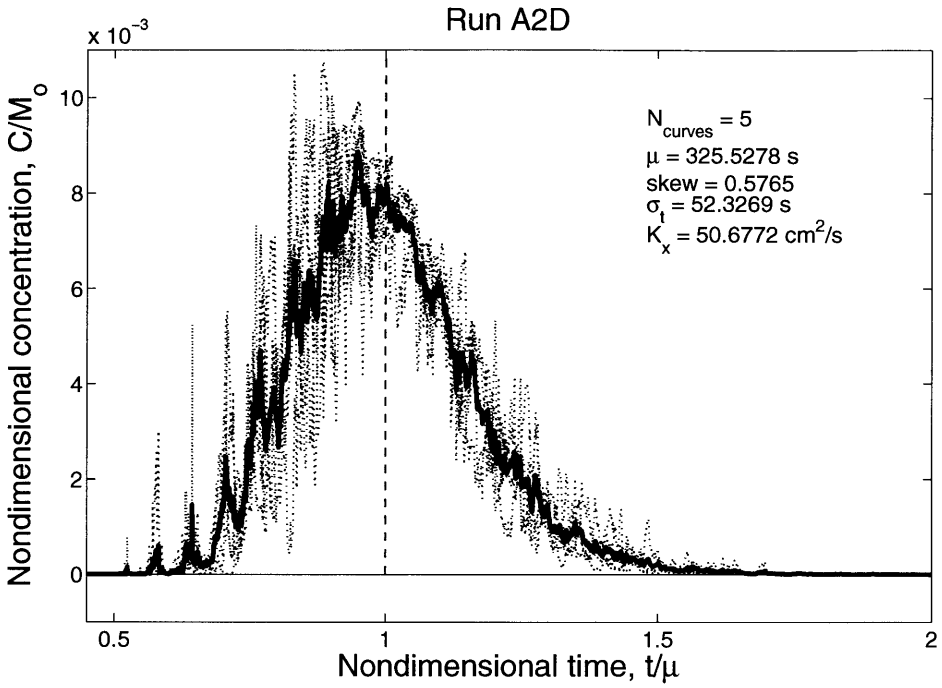
Run A2D
x 10^-3
Nondimensional concentration, C/M_o
N_curves = 5
μ = 325.5278 s
skew = 0.5765
σ_t = 52.3269 s
K_x = 50.6772 cm^2/s
Nondimensional time, t/μ

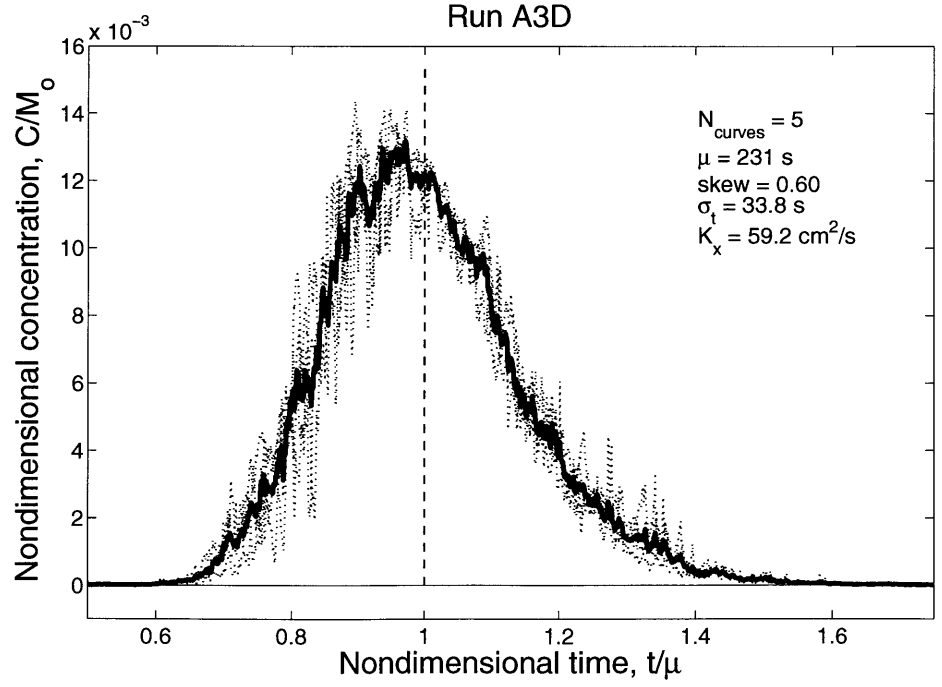
Run A3D
x 10^-3
Nondimensional concentration, C/M_o
N_curves = 5
μ = 231 s
skew = 0.60
σ_t = 33.8 s
K_x = 59.2 cm^2/s
Nondimensional time, t/μ

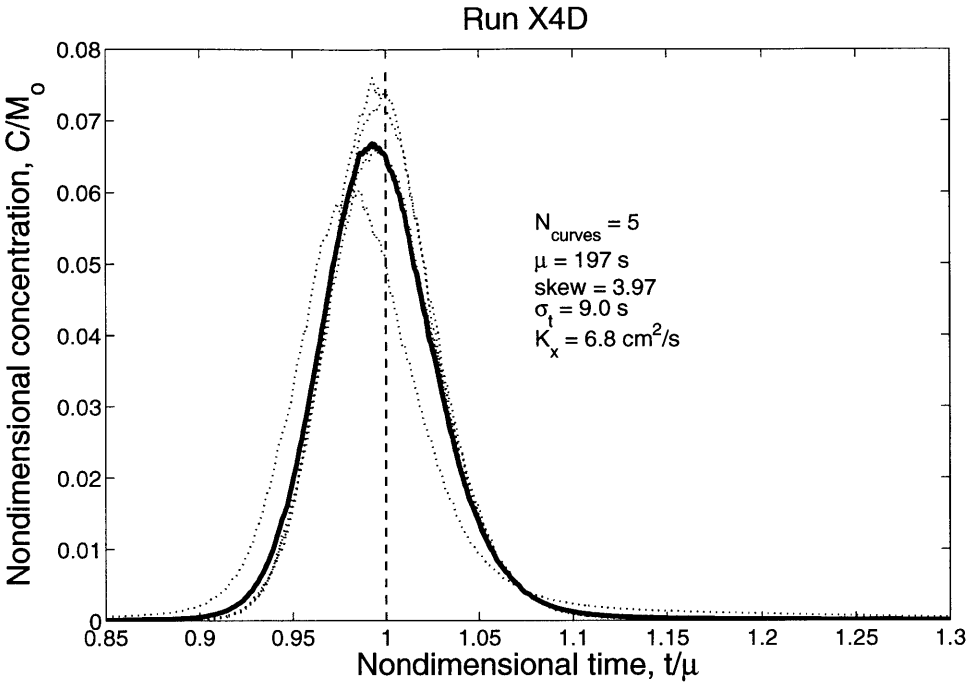
Run X4D
Nondimensional concentration, C/M$_o$
Nondimensional time, t/μ
N$_{curves}$ = 5
μ = 197 s
skew = 3.97
σ$_t$ = 9.0 s
K$_x$ = 6.8 cm^2/s
0.08
0.07
0.06
0.05
0.04
0.03
0.02
0.01
0
0.85
0.9
0.95
1
1.05
1.1
1.15
1.2
1.25
1.3

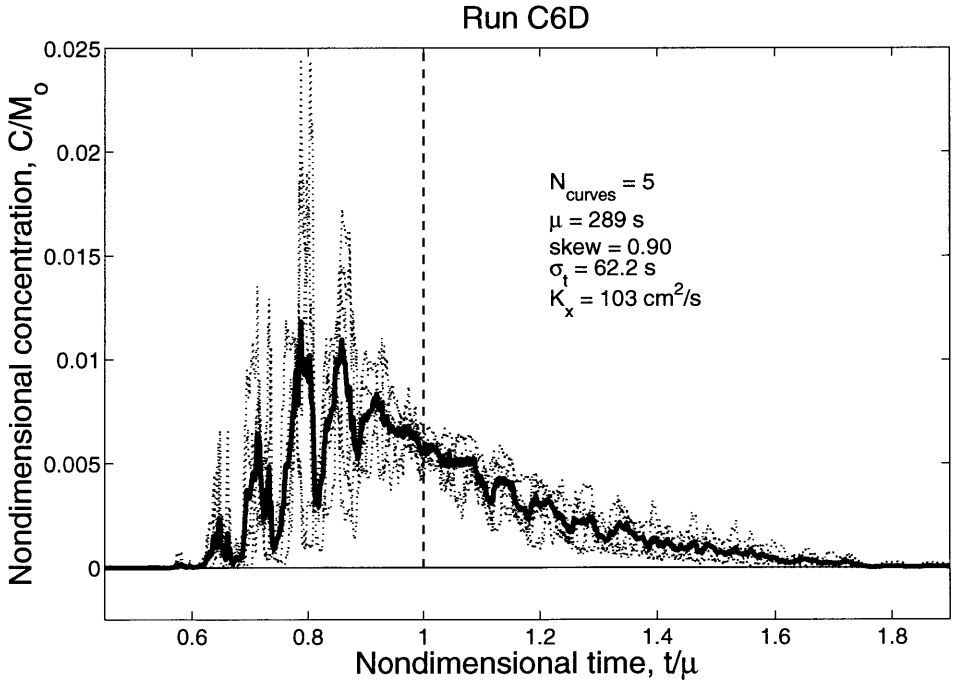
Run C6D
Nondimensional concentration, C/M$_o$
Nondimensional time, t/μ
N$_{curves}$ = 5
μ = 289 s
skew = 0.90
σ$_t$ = 62.2 s
K$_x$ = 103 cm^2/s
0.025
0.02
0.015
0.01
0.005
0
0.6
0.8
1
1.2
1.4
1.6
1.8

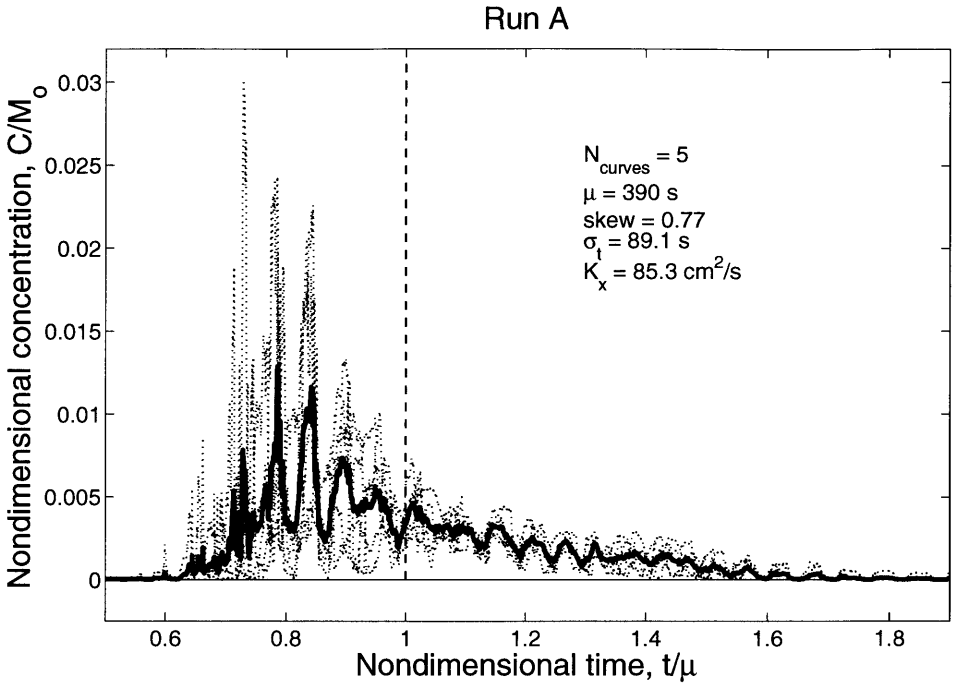
Run A
Nondimensional concentration, C/M$_o$
0.03
0.025
0.02
0.015
0.01
0.005
0
N$_{curves}$ = 5
μ = 390 s
skew = 0.77
σ$_t$ = 89.1 s
K$_x$ = 85.3 cm^2/s
0.6
0.8
1
1.2
1.4
1.6
1.8
Nondimensional time, t/μ

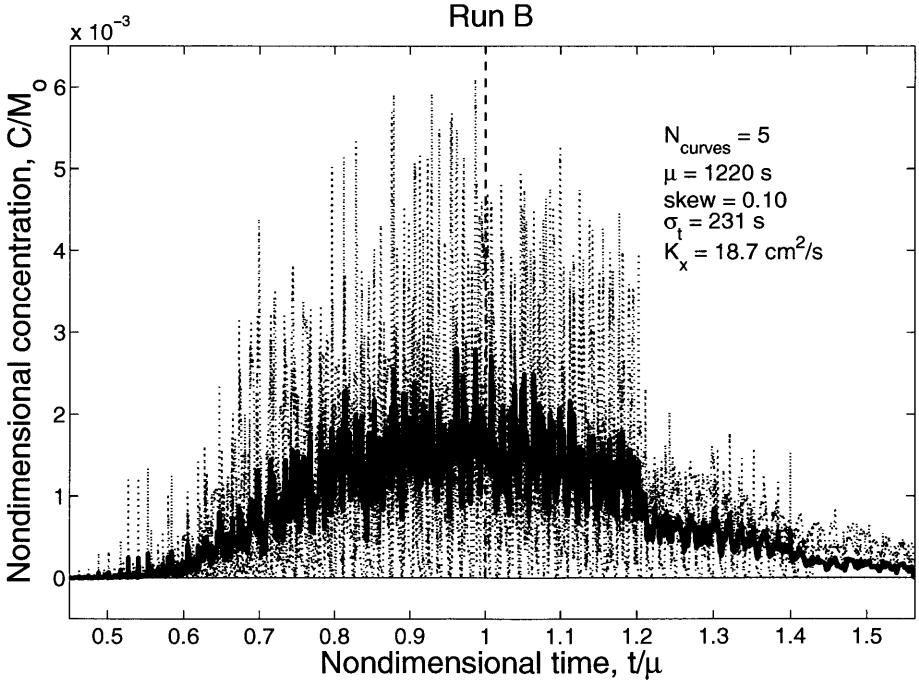
Run B
x 10^{-3}
Nondimensional concentration, C/M$_o$
6
5
4
3
2
1
0
N$_{curves}$ = 5
μ = 1220 s
skew = 0.10
σ$_t$ = 231 s
K$_x$ = 18.7 cm^2/s
0.5
0.6
0.7
0.8
0.9
1
1.1
1.2
1.3
1.4
1.5
Nondimensional time, t/μ

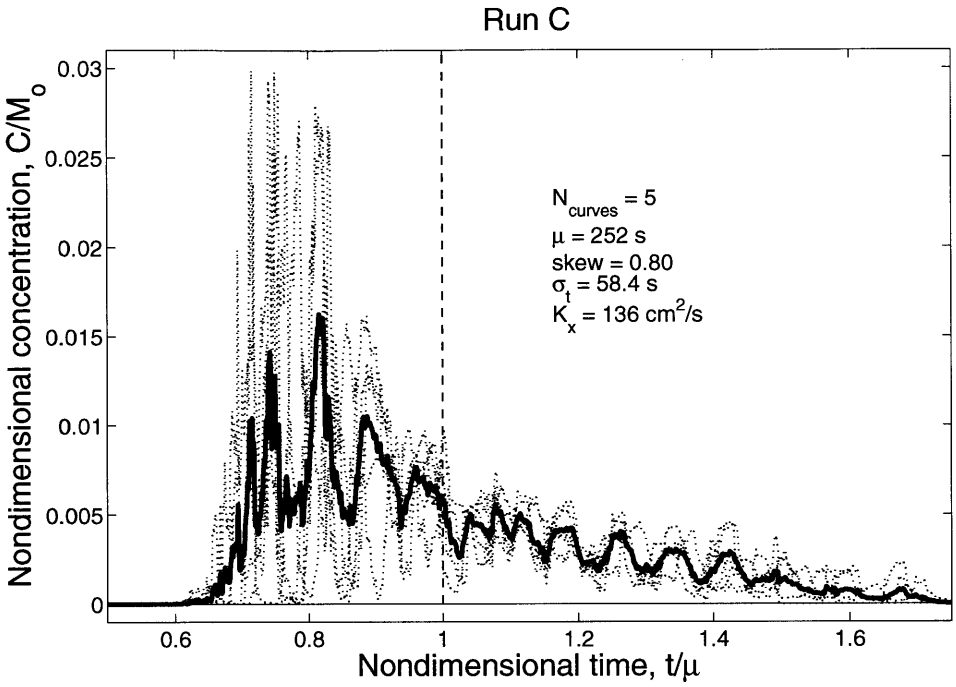
Run C
Nondimensional concentration, C/M$_o$
0.03
0.025
0.02
0.015
0.01
0.005
0
0.6
0.8
1
1.2
1.4
1.6
Nondimensional time, t/μ
N$_{curves}$ = 5
μ = 252 s
skew = 0.80
σ$_t$ = 58.4 s
K$_x$ = 136 cm^2/s

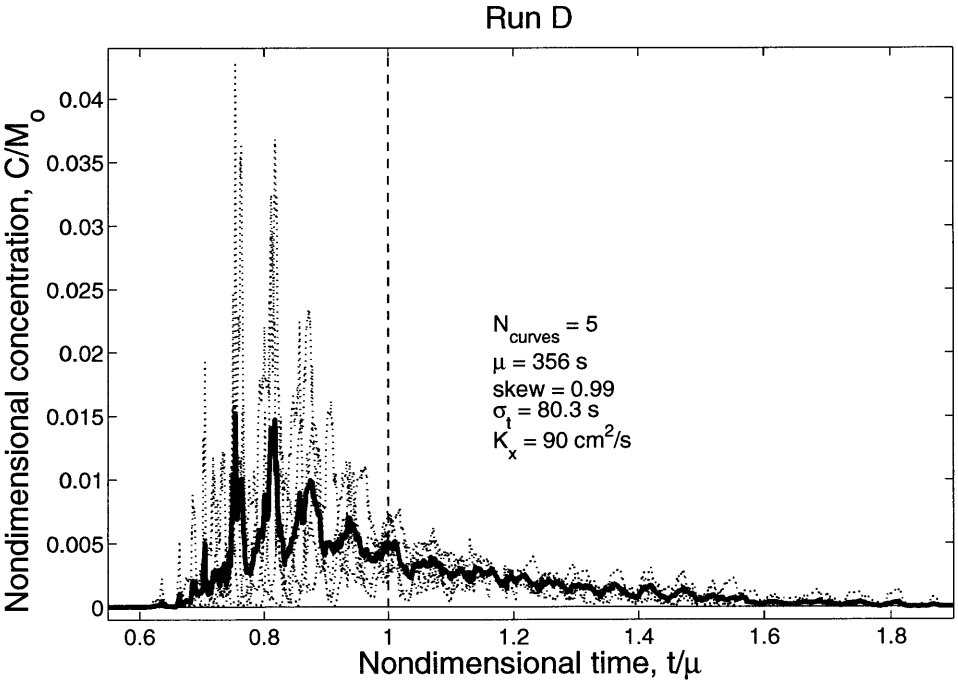
Run D
Nondimensional concentration, C/M$_o$
0.04
0.035
0.03
0.025
0.02
0.015
0.01
0.005
0
0.6
0.8
1
1.2
1.4
1.6
1.8
Nondimensional time, t/μ
N$_{curves}$ = 5
μ = 356 s
skew = 0.99
σ$_t$ = 80.3 s
K$_x$ = 90 cm^2/s

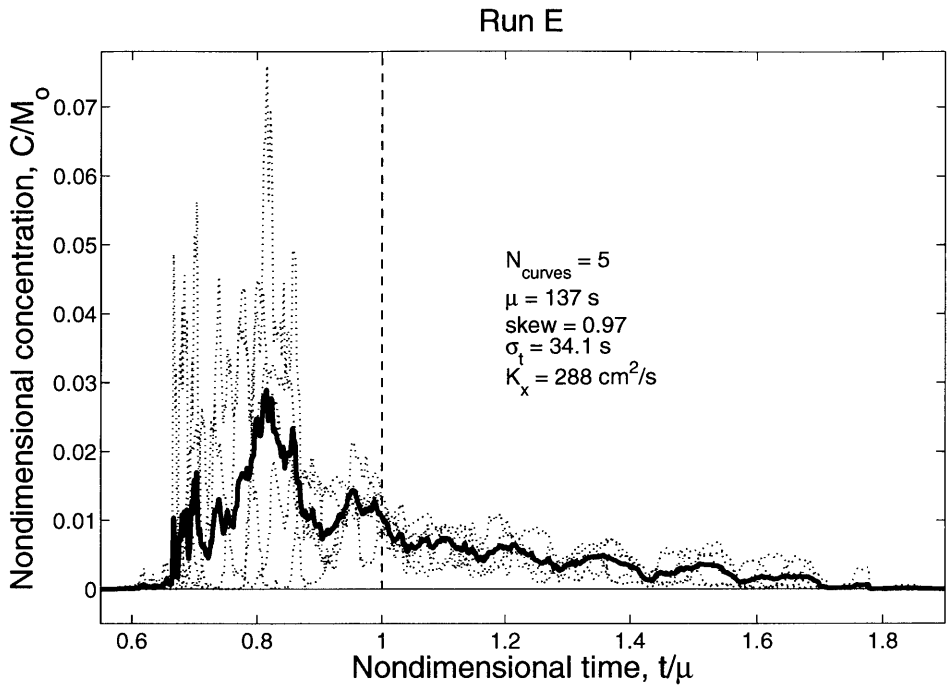
Run E
Nondimensional concentration, C/M$_o$
0.07
0.06
0.05
0.04
0.03
0.02
0.01
0
N$_{curves}$ = 5
μ = 137 s
skew = 0.97
σ$_t$ = 34.1 s
K$_x$ = 288 cm^2/s
0.6
0.8
1
1.2
1.4
1.6
1.8
Nondimensional time, t/μ

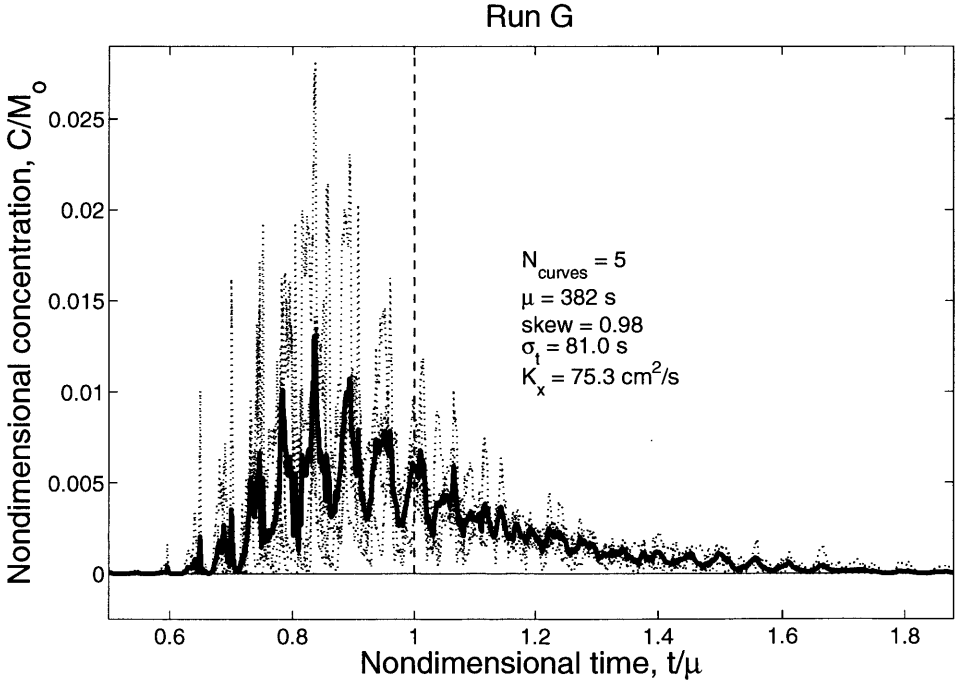
Run G
Nondimensional concentration, C/M$_o$
0.025
0.02
0.015
0.01
0.005
0
N$_{curves}$ = 5
μ = 382 s
skew = 0.98
σ$_t$ = 81.0 s
K$_x$ = 75.3 cm^2/s
0.6
0.8
1
1.2
1.4
1.6
1.8
Nondimensional time, t/μ

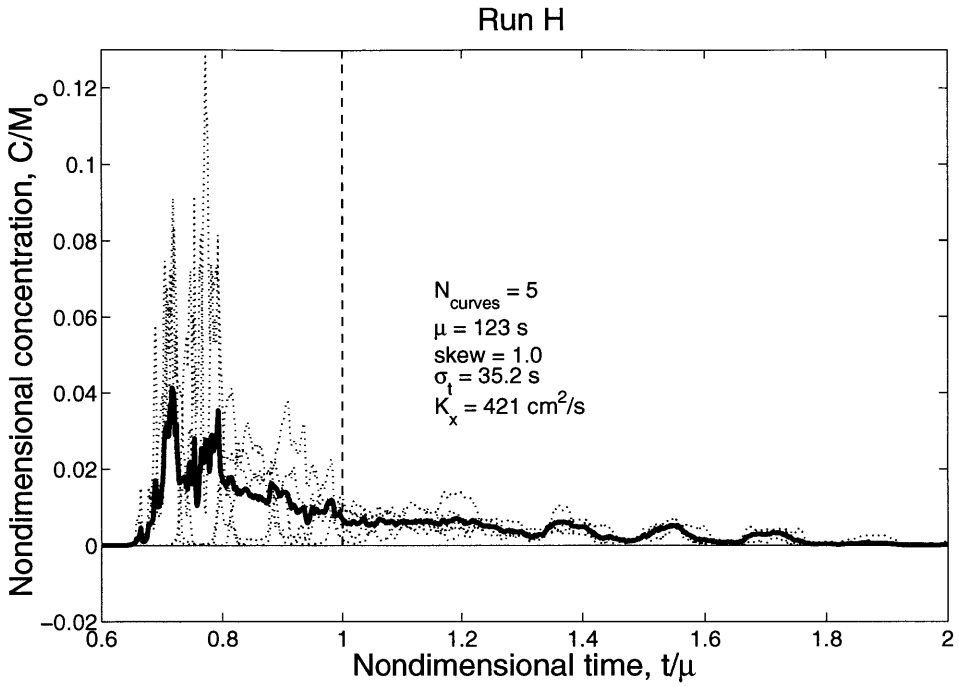
Run H
Nondimensional concentration, C/M$_o$
0.12
0.1
0.08
0.06
0.04
0.02
0
−0.02
N$_{curves}$ = 5
μ = 123 s
skew = 1.0
σ$_t$ = 35.2 s
K$_x$ = 421 cm^2/s
0.6
0.8
1
1.2
1.4
1.6
1.8
2
Nondimensional time, t/μ

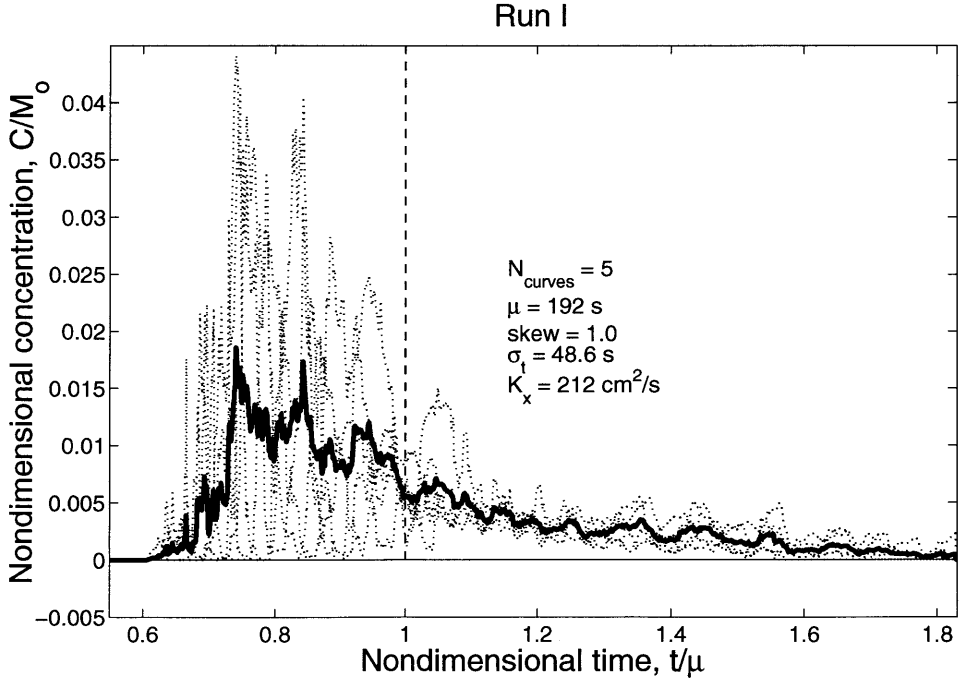
Run I
Nondimensional concentration, C/M$_o$
0.04
0.035
0.03
0.025
0.02
0.015
0.01
0.005
0
−0.005
N$_{curves}$ = 5
μ = 192 s
skew = 1.0
σ$_t$ = 48.6 s
K$_x$ = 212 cm^2/s
0.6
0.8
1
1.2
1.4
1.6
1.8
Nondimensional time, t/μ

Appendix B

Matlab Programs

B.1 removeblips.m

```
% Program to remove spurious data from fluorometer recordings
% 24 June 05
% Input: 'filename' (No extension)

function removeblips(filename)

% Load data
file_string=char(strcat(filename,'.asc'));
fid=fopen(file_string);
data=fscanf(fid,'%f',[11,inf]);
data=data.';
fclose(fid);

l=size(data,1);
datanew(1,:)=data(1,:);
j=2;
```

```
% Search for rows of data with order of magnitude differences from the
% previous row. Remove these rows from ASCII file.

for i=2:l,
    if abs(data(i,6)) > 10.*(abs(data(i-1,6)))
        data(i,:)=data(i-1,:);
    elseif abs(data(i,11)) > 10*(abs(data(i-1,11)))
        data(i,:)=data(i-1,:);
    elseif abs(data(i,6)) < 0.1.*(abs(data(i-1,6)))
        data(i,:)=data(i-1,:);
    elseif abs(data(i,11)) < 0.1.*(abs(data(i-1,11)))
        data(i,:)=data(i-1,:);
    elseif abs(data(i,10)) < 0.1.*(abs(data(i-1,10)))
        data(i,:)=data(i-1,:);
    elseif abs(data(i,10)) > 10*(abs(data(i-1,10)))
        data(i,:)=data(i-1,:);
    else
        datanew(j,:)=data(i,:);
        j=j+1;
    end
end
m=j-1;

% Print new rows of data to file with "corrected" appended to filename.

file_output=strcat(char(filename),'corrected.txt');
fout = fopen(file_output,'wt');
    for i=1:m
        fprintf(fout,'%12.9f %12.9f %12.9f %12.9f %12.9f %12.9f'
        '%12.9f %12.9f %12.9f %12.9f %12.9f\n',datanew(i,:));
```

```
end
fclose(fout);
```

B.2 compilecurves.m

```
function [tavgcomposite,Ubarcomposite,sigmatcomposite,sigmax,skewcomposite,
    seriestime,avgC,Crmscomposite,Kx,Mo]=compilecurves(file)

% Program to read ASCII files output from fluorometer, adapted from
% "curveslinedup.m" by Anne Lightbody.
% Requires accompanying program, "individualcurve.m" (also modified from
% version created by Anne Lightbody), which processes each individual
% fluorometer record.
% This program also requires an accompanying text file
% with a row for each realization in ensemble, and with the following
% columns:
%  "filename", "injection time", "#", "#", "approximate start time of
%  record", "approximate end time of record", "distance from injector to
%  fluorometer", "#", "#", "#", "#". # are unimportant numbers.
% Example:
%  FL060102.ASC 2.00 33 33 3.00 7.97 1130 0.143 0.143 4 2
% Input:  file     = file designation, e.g. 'A5'
% Output: curves of normalized concentration versus time and statistics
% of concentration distribution.

if nargin<2, toggle1=0; end
if nargin<3, toggle2=0; end
if nargin<4, X=0; end
```

```
if nargin<5, R=0; end
if nargin<6, M=0; end
if nargin<7, SITE=0; end

% Load data
prep=strcat(char(file),'prep.txt');
[filename,T,Vstart,Vend,Tstart,Tend,x,r,m,site,dye]                    30
=textread(prep,'%s%f%f%f%f%f%n%n%n%n%n');

totaln=length(filename);

Trelease=T.*60
Tstart=Tstart.*60
Tend=Tend.*60              % convert time to s

% Check to make sure that there are no errors in prep file
if exist(find((Tend-Tstart)<0))~=0;                                    40
    error('At least one Tstart value is greater than its Tend value');
end
if exist(find((Vstart-Vend)<0))~=0;
    error('At least one Vend value is greater than its Vstart value');
end
if exist(find((Tstart-Trelease)<0))~=0;
    error('At least one Trelease value is greater than its Tstart value');
end

ncurves=totaln;                                                        50
for i=1:1:ncurves
    index(i)=i;
end
```

```
% Use individualcurve.m to evaluate each curve listed in prep file,
% creating matrices of C and time (in seconds) with all the results and
% 0's filling the empty spaces
disp('Now processing: ')
disp(filename(index(1)))
[timematrix,Cmatrix,tavg,sigmat,skewness,Mo]
=individualcurve(filename(index(1)),Trelease(index(1)),Tstart(index(1)),
Tend(index(1)),dye(1),0);
timematrix(:,1)=timematrix(:,1)/tavg(1);

for i=2:ncurves
    disp(filename(index(i)))
    longest=size(timematrix,1);
    [timetemp,Ctemp,tavg(i),sigmat(i),skewness(i),Mo(i)]
    =individualcurve(filename(index(i)),Trelease(index(i)),
    Tstart(index(i)),Tend(index(i)),dye(i),0);

    if length(timetemp)>longest
        timematrix=[timematrix;zeros((length(timetemp)-longest),(i-1))];
        timematrix(:,i)=timetemp/tavg(i);
        Cmatrix=[Cmatrix;zeros((length(timetemp)-longest),(i-1))];
        Cmatrix(:,i)=Ctemp;
    else
        timematrix(:,i)=
        [timetemp/tavg(i);zeros((longest-length(timetemp)),1)];
        Cmatrix(:,i)=[Ctemp;zeros((longest-length(timetemp)),1)];
    end

end
```

```
x=x(:); tavg=tavg(:); sigmat=sigmat(:); skewness=skewness(:);
clear Ctemp; clear timetemp;

% Line up the curves so that they all have values at the same points
dt=min(timematrix(20,:)-timematrix(19,:));
timemin = min(nonzeros(timematrix))-2*dt;                          90
timemax = max(max(timematrix))+2*dt;
seriestime = linspace(timemin,timemax,(timemax-timemin)/dt)';

for i=1:ncurves
    timetemp=
    [seriestime(1);timematrix(1,i)-dt;nonzeros(timematrix(:,i));...
            max(nonzeros(timematrix(:,i)))+dt;seriestime(end)];
    Ctemp=[0;0;Cmatrix((1:length(nonzeros(timematrix(:,i)))),i);0;0];
    Cmatrixnew(:,i)=interp1q(timetemp,Ctemp,seriestime);
end                                                                100

ubar=x./tavg;                                  % units of cm/s
sigmax=sigmat.*ubar;                           % units of cm
avgC=mean(Cmatrixnew,2);                       % units of ug/L
Crms=std(Cmatrixnew-repmat(avgC,1,ncurves)); % units of ug/L
relCrms=Crms./mean(Cmatrixnew,1);              % nondimensional

figure(1); clf; hold on
for i=1:ncurves
    plot(seriestime,Cmatrixnew(:,i),'k:','LineWidth',1)            110
end

tavgcomposite=mean(tavg);
```

```
skewcomposite=mean(skewness);
sigmatcomposite=mean(sigmat);
Kx = 0.5*(((1130/tavgcomposite)^2)*((sigmatcomposite)^2))/tavgcomposite;
Ubarcomposite=mean(ubar);
Crmscomposite=mean(relCrms);

plot(seriestime,avgC,'k-','LineWidth',3)                                    120
plot([1 1],[0 (max(max(Cmatrixnew))+0.001)],'k--','LineWidth',1)
plot([0 max(seriestime)],[0 0],'k-')
xlabel('Nondimensional time, t/\mu','FontSize',22)
ylabel('Nondimensional concentration, C/M_o','FontSize',22)
title(horzcat('Run ',file(1),file(2)),'FontSize',22)

text(1.2,(max(max(Cmatrixnew))+0.001),strvcat((horzcat('N_{curves} = ',
num2str(ncurves))),horzcat('\mu = ',num2str(tavgcomposite),' s'),
horzcat('skew = ',num2str(skewcomposite)),
horzcat('\sigma_t = ',num2str(sigmatcomposite),' s'),                       130
horzcat('K_x = ',num2str(Kx),' cm^2/s')), 'FontSize',16)
set (gcf, 'PaperPositionMode','manual'); set(gcf, 'PaperPosition',
[0.5 0.5 7.5 10]); orient portrait;
hold off
```

B.3 individualcurve.m

```
function [time,Ccorrect,tavg,sigmat,skewness,m0]
=individualcurve(filename,Trelease,Tstart,Tend,dyetype,toggle)

% Program to read voltage-time output from a single fluorometer ASCII file,
```

```
% convert to a concentration-time distribution, and calculate statistics of
% the distribution. Modified version of program written by Anne Lightbody.

% Input:  filename = name of the data record entered as a string
%         Trelease = release time in decimal seconds after start of time
%         record                                                          10
%         Tstart = time of start of peak after start of time record (in
%         s)
%         Tend = time of end of peak after start of time record (in s)
%         dyetype = indication of which calibration curve to use
%             (1 = Rhodamine 6G, 2 = Rhodamine WT)
%         toggle = graph switch (default = 1, graphs)
%         toggle2 = print switch (default = 0, records not saved to file)
%
% Output: time = vector containing values of time, measured in seconds
%         after Trelease                                                  20
%         Ccorrect = vector containing nondimensional concentration
%         tavg = average cloud passage time
%         sigma = standard deviation of the curve of concentration vs.
%         time
%         skewness = skewness of the concentration curve vs. time


if nargin<5, toggle=1; end


file_string=char(filename);                                               30
fid=fopen(file_string);
data=fscanf(fid,'%f',[11,inf]);
data=data.';
fclose(fid);
```

```
hour=data(:,3);
minute=data(:,4);
second=data(:,5);
snew=splitsecond(second);
% correct for having the CTD record multiple readings at one time

timeraw=(hour+(minute./60)+(snew./3600)).*3600;
% recorded time in seconds

timefromstartlong=(timeraw-timeraw(1));
% time in seconds after start of record

Vwithneg=data(:,10);
Vraw=Vwithneg(Vwithneg>-0.03);
timefromstart=timefromstartlong(Vwithneg>-0.03);
if dyetype==1; Craw=10.^(1.5423*log10(Vraw+0.03) + 1.4529);
elseif dyetype==2; Craw=10.^(1.9905*log10(Vraw+0.03) + 2.1029);
end

minindex=min(find(timefromstart>=Tstart));
maxindex=max(find(timefromstart<=Tend));

timesingle=timefromstart(minindex:maxindex)-timefromstart(minindex);
% time only in peak counting from start of peak

Csingle=Craw(minindex:maxindex);
% concentration of this peak only

n=length(Csingle);
```

```
data=[];                                % clears data to release memory
hour=[];
minute=[];
second=[];
snew=[];                                                                    70
timeraw=[];
timefromstart=[];
Vraw=[];
Craw=[];

startlevel=mean(Csingle(1:4));
endlevel=mean(Csingle((end-3):end));

C=Csingle-startlevel;
% subtracts out background concentration (rectangular)                     80


%diagnostic plot to see if concentration correction is working
if toggle~=0
    figure(1); clf; hold on;
    plot(timesingle,Csingle,'c-',timesingle,C,'k-');
    xlabel('Time after start of peak (seconds)');
    ylabel('Concentration (\mug/L)')
    plot(timesingle(1),startlevel,'r+',timesingle(end),endlevel,'r+')
    legend('Raw concentration data',                                        90
    'Concentration data with baseline subtracted out','Baseline',
    'Baseline start and end points')
    hold off
end
```

```
time=timesingle+(Tstart-Trelease);


% Calculate statistics from moments of the peak
                                                                    100
Ccorrect = C./trapz(time,C);
% C nondimensionalized by total mass measured

m0=trapz(time,C);
% calculate moments of the peak

tavg = trapz(time,time.*Ccorrect);
% calculates time of passage, mu

sigmat = sqrt(trapz(time,(((time-tavg).^2).*Ccorrect)));            110
% standard deviation

skewness = trapz(time,(((time-tavg).^3).*Ccorrect/sigmat.^3));
% skewness


% diagnostic plot to see if time and concentration corrections are working
if toggle~=0
    figure(2); clf; hold on;
    plot(time,Csingle,'b-',time,C,'r-',time,Ccorrect,'k-')          120
    axis([0 max(time) min(C) (max(Csingle)+1)])
    xlabel('Time after start of peak (seconds)');
    ylabel('Concentration (\mug/L)')
    plot([(Tstart-Trelease) (Tstart-Trelease)],[0 (max(Csingle)+1)],'b:');
```

```
    plot([tavg tavg],[0 (max(Csingle)+1)],'r:');
    legend('Raw concentration data',
    'Concentration data with baseline subtracted out',
    'Nondimensional concentration, C/M_o','Start & end of curve',
    'Tavg (M1/M0)')
    plot([(Tend-Trelease) (Tend-Trelease)],[0 (max(Csingle)+1)],'b:');
    hold off;
end
```

B.4 plotraw.m

```
function plotraw(filename)

% Program written by Anne Lightbody, spring 2003
% Plots voltage vs. time for fluorometer data
% Input: filename = text name of file to plot in single quotes
%        (e.g., '100z06r3.asc')

fid=fopen(filename);
data=fscanf(fid,'%f',[11,inf]);
data=data.';
fclose(fid);

hour=data(:,3);
minute=data(:,4);
second=data(:,5);
```

```
snew=splitsecond(second);
% correct for having the CTD record multiple readings at one time
time=hour+(minute./60)+(snew./3600);
% recorded time in hours
timemin=(time.*60-(time(1)*60))-2;
% time in minutes after start of record

V=data(:,10);
Vzeroed=V-min(V);

figure(2); clf;
plot(timemin,V,'k-');
xlabel('Time after start of record [min]')
ylabel('Voltage [V]')
```

B.5 nlogo.m

```
% 22 January 2006
% Enda Murphy
% Program which reads in Netlogo data and outputs useful statistics
% Inputs: filename - name of Netlogo text file prefix, eg. 'A6'
%         pnumber - number of particle coordinates output from, eg. 1000
%         (pnumber is needed to sort text file)
%         Dz - average diffusivity [cm2/s]
%         (used to calculate Fickian time)
%         H - water depth [cm]
%         mu - mean passage time of tracer cloud in tracer experiment,
%         rounded to the nearest second.
```

```
%          Ubar - average velocity of patches in Netlogo [cm/s]
%          graphtoggle - 0 = default (no graphs)


function [tfick,mu,tagreement,Kx_longtime,Kx_meas,Ubar,Ucloud,skew_mu,
    kurt_mu,time,Kx_inst,Kx_approx,skewfinal,kurtfinal,Ucomfinal, t_inst]
    =nlogo(file,Dz,H,mu,Ubar,graphtoggle)

if nargin<7, graphtoggle=0; end                                          20

t_id=strcat(char(file),'time.txt');
var_id=strcat(char(file),'var.txt');
skew_id=strcat(char(file),'skew.txt');
kurt_id=strcat(char(file),'kurt.txt');
Ucom_id=strcat(char(file),'Ucom.txt');

time=load(t_id);                    %loads Netlogo output files
var=load(var_id);
skew=load(skew_id);                                                      30
kurt=load(kurt_id);
Ucom=load(Ucom_id);

time=time.';
var=var.';
skew=skew.';
kurt=kurt.';
Ucom=Ucom.';

tend=max(time);                                                          40
tfick=0.4*H*H/Dz;                   %calculates fickian timescale
```

```
tbefend=tend-1;

% Now, calculate instantaneous Kx versus time
for i=1:1:tbefend
    dvar(i,1)=var(i+1)-var(i);
    dt(i,1)=time(i+1)-time(i);
    Kx_inst(i,1)=0.5*((dvar(i,1)))/(dt(i,1));
    t_inst(i,1)=time(i)+0.5;
end

% Now calculate Kx approximation (ie. value that would be got from a tracer
% experiment)
for i=1:1:tend
    Kx_approx(i,1)=0.5*(((var(i)))/time(i));
end

tf_sec=round(tfick);
for i=tf_sec:1:tbefend
    Kx_limit(i-tf_sec+1)=Kx_inst(i);
end
Kx_longtime=mean(Kx_limit);
% The value that Kx should asymptote to

Kx_meas=Kx_approx(mu);
% Kx that you should measure for a tracer experiment for the given input mu

Ucloud=Ucom(mu);
% The mean Lagrangian velocity of the tracer cloud at time mu

skew_mu=skew(mu);
```

```
% skew at t = mu

kurt_mu=kurt(mu);
% kurt at t = mu

tagreement=0;

for i=1:1:tend
    if Kx_approx(i) >= (0.9*Kx_longtime)                    80
        tagreement=time(i);
        break;
    end
end

if tagreement == 0
    disp(horzcat
    ('K_x approximate does not converge to within 10% of the final value'
    'within ', tend, ' seconds.'))
end                                                         90

skewfinal=skew(tend);
kurtfinal=kurt(tend);
Ucomfinal=Ucom(tend);




%if graphtoggle == 1
                                                            100
figure(1);
```

```
plot(time,Kx_approx)
hold on
plot(t_inst,Kx_inst,'r-')
plot([tfick; tfick], [0;max(Kx_inst)],'r--')
plot([mu; mu], [0;max(Kx_inst)],'k-')
plot([0;tend],[Kx_longtime;Kx_longtime],'k--')
plot([tagreement;tagreement],[0;max(Kx_inst)],'b:')
xlabel('time, secs')
ylabel('Kx, cm^2/s')
title(horzcat
('Evolution of longitudinal dispersion coefficient in Netlogo: Run ',
char(file)))

legend('K_x = \sigma_x^2(t)/t','K_x = \partial{\sigma_x^2}/ \partial{t}',
't_{Fickian}=0.4*H^2/D_z','\mu','asymptotic K_x', 't_{agreement}',
'Location','SouthEast')

hold off

figure(2);
plot(time,skew)
hold on
xlabel('time, secs')
ylabel('skewness coefficient')
title(horzcat('Evolution of skewness in Netlogo: Run ',char(file)))
hold off

figure(3);
plot(time,Ucom)
hold on
```

```
plot([0;tend],[Ubar;Ubar],'r--')
xlabel('time, secs')
ylabel('Mean Lagrangian velocity of particle cloud, cm/s')
title(horzcat('Evolution of velocity of particle cloud in Netlogo: Run ',
char(file)))
hold off

%end
```

B.6 nlogobatch.m

```
% 22 January 2006
% Enda Murphy
% Function to batch process Netlogo runs - requires nlogo.m and prep file
% containing input columns "run name (eg.A6)",
% "average diffusivity (in Netlogo)","water depth, H","t_mu, the mean
% passage time of the tracer in the corresponding lab experiment", and
% "average velocity of patches in netlogo, Ubar".
% Inputs: prepfilename - name of batchfile as string (eg.
% 'RunsA6toC5.txt')
```

10

```
function [tfick,mu,tagreement,Kxlongtime,Kxmeas,Ubar,Ucloud,skewmu,kurtmu,
    timematrix,Kxinstmatrix,Kxapproxmatrix,skewfinal,kurtfinal,Ucomfinal,
    tinstmatrix]=nlogobatch(prepfilename)

[filename,Dz,H,tmu,U]=textread(prepfilename, '%s%f%f%d%f');

totaln=length(filename);
```

```
longest=7000;                    % longest time that simulations ran for

disp('Now processing: ')                                              20
disp(filename(1))
[tfick,mu,tagreement,Kxlongtime,Kxmeas,Ubar,Ucloud,skewmu,kurtmu,
    timematrix(:,1),Kxinstmatrix(:,1),Kxapproxmatrix(:,1),skewfinal,
    kurtfinal,Ucomfinal, tinstmatrix(:,1)]=nlogo(filename(1),Dz(1),H(1),
    tmu(1),U(1), 0);

for i=2:1:totaln
    disp(filename(i))
 longest=size(timematrix,1);
 longestinst=size(Kxinstmatrix,1);                                    30
 [tfick(i),mu(i),tagreement(i),Kxlongtime(i),Kxmeas(i),Ubar(i),Ucloud(i),
     skewmu(i),kurtmu(i),timetemp,Kxinsttemp,Kxapproxtemp,skewfinal(i),
     kurtfinal(i),Ucomfinal(i),tinsttemp]=nlogo(filename(i),Dz(i),H(i),
     tmu(i),U(i), 0);

     if length(timetemp)>longest
        timematrix=[timematrix;zeros((length(timetemp)-longest),(i-1))];
        timematrix(:,i)=timetemp;
        Kxapproxmatrix=[Kxapproxmatrix;zeros((length(timetemp)-longest),
        (i-1))];                                                      40
        Kxapproxmatrix(:,i)=Kxapproxtemp;

     else
        timematrix(:,i)=[timetemp;zeros((longest-length(timetemp)),1)];
        Kxapproxmatrix(:,i)=[Kxapproxtemp;
                             zeros((longest-length(timetemp)),1)];
     end
```

```
    if length(Kxinsttemp)>longestinst
        Kxinstmatrix=[Kxinstmatrix;zeros((length(Kxinsttemp)-longestinst),
                    (i-1))];
        Kxinstmatrix(:,i)=Kxinsttemp;
        tinstmatrix=[tinstmatrix;zeros((length(Kxinsttemp)-longestinst),
                    (i-1))];
        tinstmatrix(:,i)=tinsttemp;
    else
        tinstmatrix(:,i)=[tinsttemp;zeros((longestinst-length(tinsttemp)),1)];
        Kxinstmatrix(:,i)=[Kxinsttemp;zeros((longestinst-length(tinsttemp)),1)];
    end
end

tfick=tfick(:); mu=mu(:); tagreement=tagreement(:);
Kxlongtime=Kxlongtime(:); Kxmeas=Kxmeas(:);
Ubar=Ubar(:); Ucloud=Ucloud(:); skewmu=skewmu(:); kurtmu=kurtmu(:);
skewfinal=skewfinal(:); kurtfinal=kurtfinal(:); Ucomfinal=Ucomfinal(:);
clear Kxinsttemp; clear Kxapproxtemp; clear timetemp; clear tinsttemp;
```

B.7 readnetlogo.m

```
% 13 March 2005
% Enda Murphy
% function to read in x-coordinates and z-coordinates of particles from
% Netlogo output text file.
% Inputs: filename - name of file input as a string, eg. 'modeldata.txt'
%         pnumber - number of particle coordinates output from, eg. 1000
```

```
%          t - time at which netlogo run was stopped in seconds, eg. 390
%          (pnumber is needed to sort text file)
%  Outputs: xcor,zcor - coordinates of particles
%           tcor,tzcor - coordinates converted to temporal

function[xcor,zcor,tcor,tzcor]=readnetlogo(filename,pnumber,t)

file_string=char(filename);
fid=fopen(file_string);

%  x-coordinates
xcorstart=fscanf(fid,'%s',1);
limit=pnumber - 2;
xcorm=fscanf(fid,'%f',[limit,1]);
xcorend=fscanf(fid,'%s',1);
lst=length(xcorstart) - 1;
lend=length(xcorend) - 1;

for i=1:lst
    xcorstart_short(i)=xcorstart(i+1);
end

for i=1:lend
    xcorend_short(i)=xcorend(i);
end

num1 = str2double(xcorstart_short);
num2 = str2double(xcorend_short);
xcor(1,1)=num1;
d=pnumber-1;
```

```
xcor(2:d,1)=xcorm;
xcor(pnumber,1)=num2;


                                                                    40
% z-coordinates
zcorstart=fscanf(fid,'%s',1);
zcorm=fscanf(fid,'%f',[limit,1]);
zcorend=fscanf(fid,'%s',1);
lstz=length(zcorstart) - 1;
lendz=length(zcorend) - 1;

for i=1:lstz
    zcorstart_short(i)=zcorstart(i+1);
end                                                                 50

for i=1:lendz
    zcorend_short(i)=zcorend(i);
end

num1z = str2double(zcorstart_short);
num2z = str2double(zcorend_short);
zcor(1,1)=num1z;
zcor(2:d,1)=zcorm;
zcor(pnumber,1)=num2z;                                              60


fclose(fid);

xavg=mean(xcor);
uavg=xavg/t;
```

```
ustar=xcor./t;

for i=1:pnumber
    tcor(i)=xavg./ustar(i);
end

tzcor=rot90(zcor);
tzcor=rot90(tzcor);

figure(2);
hist(xcor,70)

figure(3);
hist(zcor,70)

figure(1);
plot(xcor,zcor,'.b')
title('Locations of particles at t = 310seconds')
xlabel('x, cm')
ylabel('y, cm')

hold on
```

B.8 LDVdata.m

```
function [Ubar, U_rms, Vbar, V_rms, RS, uvv, vuu, vvv, uuu, y, datarate]
```

```
= LDV_data2(L, Velfile, Coordfile, Recfile, peaksgn, tmove, figstart)

%Program, modified from version written by Brian White at MIT, which
%takes raw LDV data file and parses into smaller files, corresponding to
%positions in the traverse


%L: length of each position record in seconds
%Velfile:  name of LDV raw data file with extension
%Coordfile: text file with traverse y-positions in order of sampling
%Recfile:  base file name (w/out extension) for parsed data files
%(corresponding to each traverse position)
%peaksgn is important

Rec = load(Velfile);
y = load(Coordfile);

N = length(y);                  %Number of individual position-records

Rec(:, 2) = Rec(:, 2)/1000;     %Convert time to seconds
Rec(:, 3) = Rec(:, 3)/1000;     %Convert transit time to seconds
Rec(:, 4:5) = Rec(:, 4:5)*100;  %Convert velocity to cm/s
probedirect = sign(mean(Rec(:,5)));

if probedirect == -1            %adjust for LDV orientation
    Rec(:, 5) = -Rec(:, 5);
    Rec(:, 4) = -Rec(:, 4);
end

figure(figstart)
```

```
plot(Rec(:,2),Rec(:,4),'b.')
hold on

T = L : L : N*L;          %array of individual position-record end-times
bias = 0;


begin(1) = 1;
for j = 1:N;                                                    40
    j
    lowind = find( ( Rec(1:end-1, 2) <= T(j)-15 ) &
    ( Rec(2:end,2) > T(j)-15 ) );
    %lowind and highind form a window around the approximate time when
    %the LDV probe was moving

    highind = find( ( Rec(1:end-1, 2) <= T(j)+15 ) &
    ( Rec(2:end,2) > T(j)+15 ) );
    %Traverse move time of T(j)
                                                                50
    if isempty(highind)
        highind = size(Rec,1);
    end
    %%In case lowind is < begin(j+1) - happens if this record is empty
    lowind = max(lowind, begin(j));

    if N==1
        begin(j) = 1;
        fin(j) = length(Rec(:,2));
    else                                                        60
```

```
[peak, indx] = max( abs(Rec(lowind:highind,4)) );

maxind = indx + lowind - 1;
fin_vect = find( Rec(maxind,2) - Rec(:,2) >= 1);
%Find all samples at least 1 second prior to peak
fin(j) = fin_vect(end);
%Take the first
begin_vect = find( Rec(:,2) - Rec(maxind,2) >= 1);
%Find all samples at least 1 second after the peak                    70
if j~=N
    begin(j+1) = begin_vect(1);
end
end
%fin(j) is the last point of the previous location-record
%begin(j+1) is the first point of the new location-record
%The traverse move between them is removed
%In case fin(j) < begin(j) - if record is empty

fin(j) = max(fin(j), begin(j));                                      80
if j~=N
    begin(j+1) = max(begin(j+1), fin(j)+1);
end

plot( Rec( begin(j),2 ), Rec( begin(j),4 ), 'ro')
plot( Rec( fin(j),2 ), Rec( fin(j),4 ), 'ro')
% plot( Rec( begin(j),2 ), Rec( begin(j),5 ), 'ro')
% plot( Rec( fin(j),2 ), Rec( fin(j),5 ), 'ro')


                                                                     90
datarate(j) = (fin(j) - begin(j))/L;
```

```
newRec = Rec(begin(j) : fin(j), :);
%parse into individual record

newRec(:,2) = newRec(:,2) - newRec(1,2);
%subtract t0

u = newRec(:, 5);          %u and v for each position record
v = newRec(:, 4);                                              100
tt = newRec(:,3);
wt = tt/sum(tt);

Ubar(j) = sum(u.*wt);
Vbar(j) = sum(v.*wt);

uprime = u - Ubar(j);
vprime = v - Vbar(j);
U_rms(j) = sqrt(sum(wt.*uprime.^2));
V_rms(j) = sqrt(sum(wt.*vprime.^2));                           110
RS(j) = sum(wt.*uprime .* vprime);
uvv(j) = sum(wt.*uprime .* vprime.^2);
vuu(j) = sum(wt.*vprime .* uprime.^2);
uuu(j) = sum(wt.*uprime.^3);
vvv(j) = sum(wt.*vprime.^3);

fileid = num2str( y(j) );
%file identifier is y-coordinate - convert from fp to text string

ifile = [Recfile char(fileid) '.txt'];                         120
%create file name for current position record
```

```
    save( ifile, 'newRec', '-ASCII', '-TABS' )
    %save position record to new file

end

length(y)
hold off
```

130

Appendix C

RWPT Model Code

This is the Netlogo code that implements a random walk particle-tracking model for a vegetated channel with a stepped diffusivity profile. Comments are indicated by double semi-colons (;;). A manual which describes the Netlogo language may be downloaded from http://ccl.northwestern.edu/netlogo/docs/.

C.1 vegetatedchannel.nlogo

```
globals [step time dt L nsolidcells var xbar scale xnewmax
         xnewmin xcmin xcmax xnewbar axmin axmax yhist nhist
         histbars Kx_theory Kx_actual passed nsorb ndesorb nsorbed
         sorbremain desorbremain nmobile nturtles U_o z1 H/h cmscale
         phi tml Dtz fluorheight lowerfluor_range upperfluor_range
         xbarlocal xm xrange yrange vary ybar nb nbottom nt ntop
         ntref ntopreflect ntthru ntopthru nbthru nbotthru nremain
         nr effectivePr averagePr dv vo Kx_inst Ucom skew kurtosis]
                                    ;;  global variables

patches-own [vel Dz]                ;;  patch variables
```

```
turtles-own [ xc        ; unwrapped xcor
              yc        ; unwrapped ycor
              delx dely xnew Gauss Gx
              localvel  ; local velocity
              phase localDz farDz local_turtle_c dzb v1 v2 t1 t2
              dz1 dz2 dzb2 R R2 Prhightolow newdely newdelx
              Xi farvel dx1 dx2 Prcheck skpar kurtpar]
                          ;;  turtle variables                    20


to setup                                ;;  setup command procedure
   ca                                   ;;  clear all
   set-default-shape turtles "circle"   ;;  makes the default turtle shape
                                        ;;  a circle
   set nbottom 0
   set ntop 0
   set ntopthru 0
   set ntopreflect 0                                               30
   set nbotthru 0
   set nremain 0
   set effectivePr 0
   set nturtles 10000                   ;;  global variable set to 10000
   set nsolidcells 8                    ;;  8 solid cells (red border)
   set nmobile nturtles                 ;;  Makes nmobile equal to no. of
                                        ;;  turtles (10000).
   set nsorbed 0
   set cmscale 1.642857143              ;; no. of patches per realworld cm
   set sorbremain 0                                                40
   set desorbremain 0
   set H/h 2 * (screen-edge-y - (nsolidcells + 0.5)) / (h * cmscale)
```

```
set z1 0                                ;; input in cm
set U_o (U1 + U2) / 2
set Dtz 2.201742229                     ;; input in cm^2/s

crt nturtles                            ;; creates 10000 (or nturtle)
                                        ;; turtles


ask turtles [                                                    50
    pd                                  ;; turtles trace path in their own
                                        ;; colour.

    set color yellow                    ;; turtles are yellow.

    set phase "mobile"                  ;; writes "mobile" to the turtle
                                        ;; variable 'phase'.

    set heading 90                      ;; sets turtles heading horizontally
                                        ;; from L to R.                60

    set xcor -1 * screen-edge-x         ;; positions turtles x-coordinate
                                        ;; at leftmost side of graphic display.

    set xc xcor                         ;; stores x-coordinate in 'xc' variable.

    set xnew -1.0 * screen-edge-x       ;; stores initial x-coordinate in
                                        ;;'xnew' variable.

    set ycor -11.5 + (h * cmscale)                               70
    ]
;; ask turtle 10 [set color green]
```

```
if line
    [ ask turtles with [ who <= 500 ] [ set ycor random-int-or-float
    (screen-edge-y - (nsolidcells + 0.5)) ]

      ask turtles with [ who > 500 ] [ set ycor random-int-or-float -1.0
      * (screen-edge-y - (nsolidcells + 0.5))]
    ]                                                                    80
 ;; randomly distributes turtles in a line along the y-axis if 'line'
 ;; switch is on

ask turtles [
    set yc ycor
    ]
 ;;  stores turtle y-coordinate in 'yc' variable

ask patches with [pycor < ((z1 * cmscale) + 0.5 - screen-edge-y
+ nsolidcells) and pycor >= (0.5 + nsolidcells - screen-edge-y )]      90
[set Dz Dw]
;; Initializes wake zone diffusivity

ask patches with [pycor >= ((z1 * cmscale) + 0.5 - screen-edge-y
+ nsolidcells) and pycor <= (screen-edge-y - nsolidcells - 0.5)]
[set Dz Dtz]
;; Initializes shear layer diffusivity

ask turtles [set Prhightolow (1 - sqrt( Dw / Dtz ))]
;; sets probability of reflection at diffusivity interface              100

set scale 1
```

```
    set nhist 0
    set passed 0
    set axmin 0
    set axmax 2 * screen-edge-x
    set dt 1 ;; sets time step

    set L (screen-edge-y - (nsolidcells + 0.5))
    set phi ((z1 * cmscale / (2 * L)) ^ 3) * ((U1 - U2) * tml / Dw)

    if phi <= 0.5 [set Kx_theory (0.5 * (U1 - U2) * ((L * 2 / cmscale)
     ^ 2)) / tml]

    if phi > 0.5 [set Kx_theory (0.1 * (z1 ^ 3) * ((U1 - U2) ^ 2)
    * cmscale) / (Dw * 2 * L)]

    grid-setup ;; runs grid-setup when 'setup' button is pressed
end

to grid-setup ;; Initializes environment

;; Input velocities for each patch in cm/s - sample velocities shown
    ask patches with [pycor = ( - 11)]
      [set vel 0.726782608
       set pcolor scale-color blue vel 0 (1.2 * U1)]
    ask patches with [pycor = ( - 10)]
      [set vel 2.180347825
       set pcolor scale-color blue vel 0 (1.2 * U1)]
    ask patches with [pycor = ( - 9)]
      [set vel 2.378713043
       set pcolor scale-color blue vel 0 (1.2 * U1)]
```

```
ask patches with [pycor = ( - 8)]
   [set vel 2.387182609
    set pcolor scale-color blue vel 0 (1.2 * U1)]
 ask patches with [pycor = ( - 7)]
   [set vel 2.466434783
    set pcolor scale-color blue vel 0 (1.2 * U1)]
 ask patches with [pycor = ( - 6)]
  [set vel 2.614452174                                          140
    set pcolor scale-color blue vel 0 (1.2 * U1)]
 ask patches with [pycor = ( - 5)]
   [set vel 2.814043478
    set pcolor scale-color blue vel 0 (1.2 * U1)]
 ask patches with [pycor = ( - 4)]
   [set vel 3.144595651
   set pcolor scale-color blue vel 0 (1.2 * U1)]
ask patches with [pycor = ( - 3)]
  [set vel 3.606804346
   set pcolor scale-color blue vel 0 (1.2 * U1)]                150
ask patches with [pycor = ( - 2)]
  [set vel 4.372969563
    set pcolor scale-color blue vel 0 (1.2 * U1)]
 ask patches with [pycor = ( - 1)]
   [set vel 5.11565652
    set pcolor scale-color blue vel 0 (1.2 * U1)]
 ask patches with [pycor = ( 0)]
   [set vel 5.845299996
    set pcolor scale-color blue vel 0 (1.2 * U1)]
 ask patches with [pycor = ( 1)]                                160
   [set vel 6.920926083
    set pcolor scale-color blue vel 0 (1.2 * U1)]
```

```
ask patches with [pycor = ( 2)]
  [set vel 7.85133478
   set pcolor scale-color blue vel 0 (1.2 * U1)]
 ask patches with [pycor = ( 3)]
  [set vel 8.520352171
   set pcolor scale-color blue vel 0 (1.2 * U1)]
 ask patches with [pycor = ( 4)]
  [set vel 9.088891302                                          170
  set pcolor scale-color blue vel 0 (1.2 * U1)]
 ask patches with [pycor = (5)]
  [set vel 9.604043477
   set pcolor scale-color blue vel 0 (1.2 * U1)]
 ask patches with [pycor = (6)]
  [set vel 9.947652172
   set pcolor scale-color blue vel 0 (1.2 * U1)]
 ask patches with [pycor = ( 7)]
  [set vel 10.35921739
   set pcolor scale-color blue vel 0 (1.2 * U1)]                180
 ask patches with [pycor = ( 8)]
  [set vel 10.8613913
   set pcolor scale-color blue vel 0 (1.2 * U1)]
 ask patches with [pycor = ( 9)]
  [set vel 11.4003913
   set pcolor scale-color blue vel 0 (1.2 * U1)]
 ask patches with [pycor = ( 10)]
  [set vel 11.871
   set pcolor scale-color blue vel 0 (1.2 * U1)]
 ask patches with [pycor = ( 11)]                               190
  [set vel 11.871
   set pcolor scale-color blue vel 0 (1.2 * U1)]
```

```
  ;; Initializes graphics
   ask patches with [((- (screen-edge-y - nsolidcells - 0.5))
     + (z1 * cmscale) >= pycor) and
     (pycor >= (- (screen-edge-y - nsolidcells - 0.5)))]
        [ifelse pxcor mod 2 != 0
        [set pcolor scale-color blue vel 0 (1.2 * U1)]
        [set pcolor green]]                                          200
   ask patches with [((- (screen-edge-y - nsolidcells - 0.5))
     + (z1 * cmscale) < pycor) and
     (pycor <= (- (screen-edge-y - nsolidcells - 0.5)) + (h * cmscale))]
        [ifelse pxcor mod 2 != 0
        [set pcolor scale-color blue vel 0 (1.2 * U1)]
        [set pcolor green]]


  ;; sets colour and velocity of boundary patches to red and zero respectively
    ask patches with [pycor > screen-edge-y - nsolidcells - 0.5]     210
       [set pcolor white
        set vel 0]
    ask patches with [pycor < ( - (screen-edge-y - nsolidcells - 0.5))]
       [set pcolor red
        set vel 0]
end


to go   ;;   commands that follow are initiated when 'go' button is pressed on
        ;;GUI                                                         220

    move-turtles  ;;   move-turtles is also initiated when 'go' is pressed
```

```
;; write data to file at end time specified in GUI by Stop_time switch
if stopswitch
[if (time = Stop_time) [
ask turtles [set yc (yc / cmscale) + ((H/h * h) / 2)]
ask turtles [set xc (xc + screen-edge-x + 0.5) / cmscale]
set yrange (values-from turtles [yc])
set xrange (values-from turtles [xc])                                    230
file-write xrange
file-write yrange
file-close
stop
]]

set step step + 1
;;  increments global variables

set time time + dt                                                       240
;;  dt is time step

set var (max list (variance values-from turtles [xc]) 0.000000001)
/ (cmscale ^ 2)
;;  gets variance of current x-coordinates of turtles and stores the the max
;;  value in var. The 0.000001 just prevents a zero value

set vary (max list (variance values-from turtles [yc]) 0.000000001)
/ (cmscale ^ 2)
;; variance in the vertical                                              250

set xbar ((mean values-from turtles [xc]) + screen-edge-x + 0.5 )
```

```
  / cmscale
  ;;  distance along x-axis to centre of mass of turtles/tracer

  set ybar ((mean values-from turtles [yc]) + 12) / cmscale
  set Kx_actual 0.5 * var / time
  ;;  computes Kx as estimated by a tracer experiment

ask turtles [set skpar ( ( ( (xc / cmscale) - xbar ) / ( var ^ 0.5 ) ) ^ 3 )]
  set skew (mean values-from turtles [skpar])
ask turtles [set kurtpar (((xc / cmscale) - xbar) ^ 4)]
  set kurtosis (((mean values-from turtles [kurtpar]) / (var ^ 2)) - 3)
  set dv var - vo
  set Kx_inst 0.5 * dv ;; calculate change in variance in 1 time step
  set Ucom xbar / time ;; calculate mean velocity of particles

  ;; Output data to text files
  file-open "var.txt"
  file-write var
  file-close
  file-open "time.txt"
  file-write time
  file-close
  file-open "Ucom.txt"
  file-write Ucom
  file-close
  file-open "skew.txt"
  file-write skew
  file-close
  file-open "kurt.txt"
  file-write kurtosis
```

```
file-close

;; GUI outputs
set-current-plot "Growth of Tracer Variance"
set-current-plot-pen "theory" plotxy time 2 * Kx_theory * (time)
;; plots expected variance from theory
set-current-plot-pen "actual" plotxy time var
;; plots calculated variance                                          290
set vo var

if (step mod 30 = 1) [
set-current-plot "Histogram" clear-plot
if (var > 0.000000001)
    [ set axmin min values-from turtles [xc] - (min values-from turtles
    [xcor] + screen-edge-x) / scale
      set axmin round axmin
      set axmax max values-from turtles [xc] +
      (screen-edge-x - max values-from turtles [xcor]) / scale          300
      set axmax round axmax
      set-plot-x-range axmin axmax
      if (nhist > 0)
          [set-plot-y-range 0 yhist]
    ]
    ;;sets max and min values of axes

set-histogram-num-bars 70
histogram-from turtles [xc]
                                                                        310
set-current-plot "Tracer Concentration Profile vs. Gaussian" clear-plot
set-plot-x-range axmin axmax
```

```
    if (nhist > 0)
            [set-plot-y-range 0 yhist]
    set-current-plot-pen "C(x)"
    set histbars 70
    set-histogram-num-bars histbars

    ;; options for limiting data output to vertical intervals
    set fluorheight (24.5 * cmscale) - (screen-edge-y - nsolidcells - 0.5)   320
    ;; setting range of fluorometer measurement
    set upperfluor_range fluorheight + 2
    set lowerfluor_range fluorheight - 2

    histogram-from turtles with [(ycor <= upperfluor_range) and
    (ycor >= lowerfluor_range)] [xc]

    set-current-plot-pen "Gauss"
    ask turtles [
        set Gx axmin + who * (axmax - axmin) / 999                          330
        set Gauss 1000 * (axmax - axmin) / histbars / sqrt (2 * pi * var)
        * exp ( -1 * (Gx - xbar) ^ 2 / (2 * var) )
        plotxy Gx Gauss
        ]                          ;; plots Gaussian curve
    set yhist plot-y-max
    set nhist 1

    ]
end
                                                                           340

to move-turtles       ;; Assigns rules of particle movements
```

```
;;    change-phase

   ;ask turtles with [phase = "mobile"]
   ask turtles
      [set localvel vel-of patch-here
      ;; assigns velocity of patch to turtle at that patch

       set delx localvel * cmscale * dt
       ;; dist = speed * time (spatial step)

       set localDz Dz-of patch-here
       ;; assigns diffusivity of patch to turtle at that patch

       set Xi random-normal 0 1
       ;; chooses random number from distribution with mean of
       ;; 0 and std deviation of 1

       set dely sqrt( 2 * localDz * (cmscale ^ 2) * dt) * Xi


       set farDz Dz-of (patch-at delx dely)
       set dzb ( -11.5 - ycor) ;; sets distance from particle to diffusivity
                               ;; interface (number must be input manually
                               ;; for specific z1 and resolution

       set R (dely / dzb)
       set R2 ((abs dely) / (abs dzb))

       ]
```

```
ask turtles with [((R2 >= 1) and (R > 0) and (ycor >= (-11.5)))]
                [set Prcheck random-float 1.0000000000000001]

;; Reflect particles at diffusivity step
ask turtles with [((R2 > 1) and (R > 0) and (ycor > (-11.5)) and
                (Prcheck < Prhightolow))]
          [set dzb2 (dely - dzb)                                    380
           set newdely (dzb - dzb2)
           set newdelx delx]

;; Transmit particles from high Dz with mid-step adjustment
ask turtles with [((R2 > 1) and (R > 0) and (ycor > (-11.5)) and
                (Prcheck > Prhightolow))]
          [set v1 (dely / dt)
           set v2 (Xi * (sqrt(2 * Dw / dt)))
           set t1 (dzb / v1)
           set t2 (dt - t1)                                         390
           set dz1 v1 * t1
           set dz2 v2 * t2
           set newdely (dz1 + dz2)
           set farvel vel-of (patch-at delx newdely)
           set dx1 (localvel * cmscale * t1)
           set dx2 (farvel * cmscale * t2)
           set newdelx (dx1 + dx2)]


;; Transmit particles from low Dz with mid-step adjustment          400
ask turtles with [((R2 > 1) and (R > 0) and (ycor < (-11.5)))]
          [set v1 (dely / dt)
```

```
        set v2 (Xi * (sqrt(2 * Dtz / dt)))
        set v2 (Xi * (sqrt(2 * farDz / dt)))
        set t1 (dzb / v1)
        set t2 (dt - t1)
        set dz1 v1 * t1
        set dz2 v2 * t2
        set newdely (dz1 + dz2)
        set farvel vel-of (patch-at delx newdely)                    410
        set dx1 (localvel * cmscale * t1)
        set dx2 (farvel * cmscale * t2)
        set newdelx (dx1 + dx2)]

ask turtles with [((R2 <= 1) or (R <= 0) )]
        [set newdely dely
         set newdelx delx]

 bound-reflect ;; Implement reflection at free surface and bed
                                                                     420

        ask turtles [
        set xc xc + newdelx
        set yc yc + newdely
        set ycor yc
        set xnew xnew + newdelx * scale]
        set xnewmax max values-from turtles [xnew]
        set xnewmin min values-from turtles [xnew]
        set xcmin min values-from turtles [xc]
        set xcmax max values-from turtles [xc]                       430

        if (xnewmax > screen-edge-x)
```

```
        [ if (xnewmax − xnewmin) > 1.5 * screen−edge−x
              [set scale min list 1 (0.67 * screen−edge−x / ( xcmax − xcmin ))
               set nhist 0
               if messages
                 [user−message "Zooming out, note change in x-axis limits"]
              ]
          ask turtles [ set xnew scale * (xc − xcmin) − screen−edge−x ]
        ]                                                                    440
    ask turtles [set xcor xnew]

end

to bound−reflect      ;; bed and free surface reflection algorithm
ask turtles[

   if ( pcolor−of (patch−at delx dely) = red) or
   (distancexy (xcor + delx) (ycor + dely) != distancexy−nowrap
   (xcor + delx) (ycor + dely) )                                             450
       [ set newdely dely − 2 * ( yc + dely − ( L * abs yc / yc ) ) ]

   if ( pcolor−of (patch−at delx dely) = white) or
   (distancexy (xcor + delx) (ycor + dely) != distancexy−nowrap
   (xcor + delx) (ycor + dely) )
      [ set newdely dely − 2 * ( yc + dely − ( L * abs yc / yc ) ) ]]

end

                                                                             460
```

Bibliography

[1] M.A. Abdelrhman. Effect of eelgrass *Zostera marina* on flow and transport. *Mar. Ecol. Prog. Ser.*, 248:67–83, 2003.

[2] J.D. Ackerman and A. Okubo. Reduced mixing in a marine macrophyte canopy. *Funct. Ecol.*, 7:305–309, 1993.

[3] R. Aris. On the dispersion of a solute in a fluid flowing through a tube. *Proc. R. Soc. Lond.*, A235:67–77, 1956.

[4] R. Aris. On the dispersion of a solute by diffusion, convection and exchange between phases. *Proc. R. Soc. Lond.*, A252(1271):538–550, 1959.

[5] Dantec Measurement Technology A/S. *User's Guide: 60X series FiberFlow.* Skovlunde, Denmark.

[6] K.E. Bencala. Characterization of transport in an acidic and metal-rich mountain stream based on a lithium tracer injection and simulations of transient storage. *Water Resour. Res.*, 26(5):989–1000, 1990.

[7] S.J. Bennett, T. Pirim, and B.D. Barkdoll. Using simulated emergent vegetation to alter stream flow direction within a straight experimental channel. *Geomorphology*, 44:115–126, 2002.

[8] J. Biggs, A. Corfield, P. Grøn, H.O. Hansen, D. Walker, M. Whitfield, and P. Williams. Restoration of the rivers Brede, Cole and Skerne: a joint Danish and British EU-LIFE demonstration project, V – Short-term impacts on the

conservation value of aquatic macroinvertebrate and macrophyte assemblages. *Aquatic Conserv.: Mar. Freshw. Ecosyst.*, 8:241–255, 1998.

[9] P. Buchhave and Jr. W.K. George. The measurement of turbulence with the laser-Doppler anemometer. *Ann. Rev. Fluid Mech.*, 11:443–503, 1979.

[10] S.E. Bunn and A.H. Arthington. Basic principles and ecological consequences of altered flow regimes for aquatic biodiversity1. *Environmental Management*, 30(4):492–507, 2002.

[11] F.G. Carollo, V. Ferro, and D. Termini. Flow velocity measurements in vegetated channels. *J. Hydraul. Eng.*, 128(7):664–673, 2002.

[12] F.G. Carollo, V. Ferro, and D. Termini. Flow resistance law in channels with flexible submerged vegetation. *J. Hydraul. Eng.*, 131(7):554–564, 2005.

[13] A. Chadwick and J. Morfett. *Hydraulics in Civil and Environmental Engineering.* E. and F.N. Spon, London, U.K., third edition edition, 1998.

[14] P.C. Chatwin. On the interpretation of some longitudinal dispersion experiments. *J. Fluid Mech.*, 48(4):689–702, 1971.

[15] P.C. Chatwin. The cumulants of the distribution of a solute dispersing in solvent flowing through a tube. *J. Fluid Mech.*, 51(1):63–67, 1972.

[16] P.C. Chatwin and C.M. Allen. Mathematical models of dispersion in rivers and estuaries. *Ann. Rev. Fluid Mech.*, 17:119–149, 1985.

[17] S.C. Chikwendu. Application of a slow-zone model to contaminant dispersion in laminar shear flows. *Int. J. Engng. Sci.*, 24(6):1031–1044, 1986.

[18] S.C. Chikwendu. Calculation of longitudinal shear dispersivity using an N-zone model as $N \rightarrow \infty$. *J. Fluid Mech.*, 167:19–30, 1986.

[19] S.C. Chikwendu and G.U. Ojiakor. Slow-zone model for longitudinal dispersion in two-dimensional shear flows. *J. Fluid Mech.*, 152:15–38, 1985.

[20] H. Christie, S. Fredriksen, and E. Rinde. Regrowth of kelp and colonization of epiphyte and fauna community after kelp trawling at the coast of Norway. *Hydrobiologia*, 375/376:49–58, 1998.

[21] P.M. Davis, T.C. Atkinson, and T.M. Wigley. Longitudinal dispersion in natural channels: 2. the roles of shear flow dispersion and dead zones in the River Severn, U.K. *Hydrol. Earth System Sci.*, 4(3):355–371, 2000.

[22] T.J. Day. Longitudinal dispersion in natural channels. *Water Resour. Res.*, 11(6):909–918, 1975.

[23] R.G. Dean. New Orleans and the wetlands of Southern Louisiana. *The Bridge*, 36(1):35–42, 2006.

[24] Z.-Q. Deng, L. Bengtsson, V.P. Singh, and D.D. Adrian. Longitudinal dispersion coefficient in single-channel streams. *J. Hydraul. Eng.*, 128(10):901–915, 2002.

[25] W.C. Dennison, R.J. Orth, K.A. Moore, J.C. Stevenson, V. Carter, S. Kollar, P.W. Bergstrom, and R.A. Batiuk. Assessing water quality with submersed aquatic vegetation: Habitat requirements as barometers of Chesapeake bay health. *BioScience*, 43(2):86–94, 1993.

[26] F.E. Dierberg, T.A. DeBusk, S.D. Jackson, M.J. Chimney, and K. Pietro. Submerged aquatic vegetation-based treatment wetlands for removing phosphorus from agricultural runoff: response to hydraulic and nutrient loading. *Water Research*, 36:1409–1422, 2002.

[27] K.N. Dimou and E.E. Adams. A random-walk, particle tracking model for well-mixed estuaries and coastal waters. *Estuar. Coast. Shelf Sci.*, 37:99–110, 1993.

[28] J. Duan and S. Wiggins. Lagrangian transport and chaos in the near wake of the flow around an obstacle: A numerical implementation of lobe dynamics. *Nonlinear Processes Geophy.*, 4:125–136, 1997.

[29] C. Dunn, F. Lopez, and M. Garcia. Mean flow and turbulence in a laboratory channel with simulated vegetation. Technical report, Dept. of Civil Engineering, University of Illinois at Urbana-Champaign, Urbana, IL, 1996.

[30] I. Eames and J.W.M. Bush. Longitudinal dispersion by bodies fixed in potential flow. *Proc. Roy. Soc. Lond.*, A455:3665–3686, 1999.

[31] J.W. Elder. The dispersion of marked fluid in turbulent shear flow. *J. Fluid Mech.*, 5:544–560, 1959.

[32] H.B. Fischer. Longitudinal dispersion and turbulent mixing in open-channel flow. *Annu. Rev. Fluid Mech.*, 5:59–78, 1973.

[33] H.B. Fischer, E.J. List, R.C.Y. Koh, J. Imberger, and N.H. Brooks. *Mixing in inland and coastal waters.* Academic Press, San Diego, CA, 1979.

[34] E.R. Vivoni Gallart. Turbulence structure of a model seagrass meadow. Master's thesis, Massachusetts Institute of Technology, 1996.

[35] M. Ghisalberti. Coherent structures and mixing layers in vegetated aquatic flows. Master's thesis, Department of Civil and Environmental Engineering, Massachusetts Institute of Technology, 2000.

[36] M. Ghisalberti and H.M. Nepf. Mixing layers and coherent structures in vegetated aquatic flows. *J. Geophys. Res.*, 107(C2):3–1–3–11, 2002.

[37] M. Ghisalberti and H.M. Nepf. The limited growth of vegetated shear layers. *Water. Resour. Res.*, 40, W07502, doi:10.1029/2003WR002776, 2004.

[38] M. Ghisalberti and H.M. Nepf. Mass transport in vegetated shear flows. *Env. Fluid Mech.*, 5(6):527–551, 2005.

[39] J.B. Grace. Effects of water depth on *Typha latifolia* and *Typha domingensis*. *Amer. J. Bot.*, 76(5):762–768, 1989.

[40] W. Granéli and D. Solander. Influence of aquatic macrophytes on phosphorus cycling in lakes. *Hydrobiologia*, 170(1):245–266, 1988.

[41] J.W. Harvey, J.E. Saiers, and J.T. Newlin. Solute transport and storage mechanisms in wetlands of the Everglades, south Florida. *Water Resour. Res.*, 41, W05009, doi:10.1029/2004WR003507, 2005.

[42] M. Healy and A.M. Cawley. Nutrient processing capacity of a constructed wetland in western Ireland. *J. Environ. Qual.*, 31:1739–1747, 2002.

[43] C.M. Ho and P. Huerre. Perturbed free shear layers. *Ann. Rev. Fluid Mech.*, 16:365–424, 1984.

[44] H. Hoteit, R. Mose, A. Younes, F. Lehmann, and P. Ackerer. Three-dimensional modeling of mass transfer in porous media using the mixed hybrid finite elements and the random-walk methods. *Math. Geol.*, 34(4):435–456, 2002.

[45] C. Hudon. Impact of water level fluctuations on St. Lawrence River aquatic vegetation. *Can. J. Fish. Aquat. Sci.*, 54:2853–2865, 1997.

[46] S. Ikeda and M. Kanazawa. Three-dimensional organized vortices above flexible water plants. *J. Hydraul. Eng.*, 122(11):634–640, 1996.

[47] R.S. Jadhav and S.G. Buchberger. Effects of vegetation on flow through free water surface wetlands. *Ecol. Eng.*, 5:481–496, 1995.

[48] R.H. Kadlec and R.L. Knight. *Treatment wetlands.* Lewis Publishers, Boca Raton, FL, 1996.

[49] S.M. Kashefipour and R.A. Falconer. Longitudinal dispersion coefficients in natural channels. *Water Res.*, 36:1596–1608, 2002.

[50] D.L. Koch and J.F. Brady. Anomalous diffusion due to long-range velocity fluctuations in the absence of a mean flow. *Phys. Fluids*, A1(1):47–51, 1989.

[51] D.L. Koch and A.J.C. Ladd. Moderate Reynolds number flows through periodic and random arrays of aligned cylinders. *J. Fluid Mech.*, 349:31–66, 1997.

[52] K. Koeltzsch. On the relationship between the lagrangian and eulerian time scale. *Atmos. Environ.*, 33:117–128, 1999.

[53] K. Koeltzsch. The height dependence of the turbulent Schmidt number within the boundary layer. *Atmos. Environ.*, 34:1147–1151, 2000.

[54] N. Kouwen, T.E. Unny, and H.M. Hill. Flow retardance in vegetated channels. *J. Irrig. Drain. Div. ASCE*, 95(2):329–342, 1969.

[55] P.K. Kundu and I.M. Cohen. *Fluid mechanics.* Academic Press, San Diego, CA, 2002.

[56] V. Kutija and H.T.M. Hong. A numerical model for assessing the additional resistance to flow introduced by flexible vegetation. *J. Hydraul. Res.*, 34(1):99–114, 1996.

[57] H.V. Leland. The influence of water depth and flow regime on phytoplankton biomass and community structure in a shallow, lowland river. *Hydrobiologia*, 506-509:247–255, 2003.

[58] L.A. Leonard and M.E. Luther. Flow hydrodynamics in tidal marsh canopies. *Limnol. Oceanogr.*, 40(8):1474–1484, 1995.

[59] L.A. Leonard and D.J. Reed. Hydrodynamics and sediment transport through tidal marsh canopies. *J. Coastal Res.*, SI36:459–469, 2002.

[60] O. Levenspiel and W. K. Smith. Notes on the diffusion-type model for the longitudinal mixing of fluids in flow. *Chem. Engng. Sci.*, 6:227–233, 1957.

[61] A.F. Lightbody. Field and laboratory observations of small-scale dispersion in wetlands. Master's thesis, Department of Civil and Environmental Engineering, Massachusetts Institute of Technology, 2004.

[62] A.F. Lightbody and H.M. Nepf. Prediction of velocity profiles and longitudinal dispersion in emergent salt marsh vegetation. *Limnol. Oceanogr.*, 51(1):218–228, 2006.

[63] F. Lopez and M. Garcia. Open-channel flow through simulated vegetation: Suspended sediment transport modeling. *Water Resour. Res.*, 34(9):2341–2352, 1998.

[64] F. Lopez and M. Garcia. Mean flow and turbulence structure of open-channel flow through non-emergent vegetation. *J. Hydraul. Eng.*, 127(5):392–402, 2001.

[65] R.J. Lowe, J.R. Koseff, and S.G. Monismith. Oscillatory flow through submerged canopies: 1. Velocity structure. *J. Geophys. Res.*, 110, C10016, doi:10.1029/2004JC002788, 2005.

[66] M. Mars, M. Kuruvilla, and H. Goen. The role of the submergent macrophyte *triglochin huegelii* in domestic greywater treatment. *Ecol. Eng.*, 12:57–66, 1999.

[67] Y. Mazda, E. Wolanski, B. King, A. Sase, D. Ohtsuka, and M. Magi. Drag force due to vegetation in mangrove swamps. *Mangroves and Salt Marshes*, 1:193–199, 1997.

[68] W.K. Meier and P. Reichert. Mountain streams - Modeling hydraulics and substance transport. *J. Env. Eng.*, 131(2):252–261, 2005.

[69] H.M. Nepf. Drag, turbulence, and diffusion in flow through emergent vegetation. *Water. Resour. Res.*, 35(2):479–489, 1999.

[70] H.M. Nepf, M. Ghisalberti, and B.L. White. A scale constraint for shear-layers generated in canopies and other obstructed flow. Env. Fluid Mech., Submitted, 2006.

[71] H.M. Nepf and E.W. Koch. Vertical secondary flows in submersed plant-like arrays. *Limnol. Oceanogr.*, 44(4):1072–1080, 1999.

[72] H.M. Nepf, C.G. Mugnier, and R.A. Zavistoski. The effects of vegetation on longitudinal dispersion. *Estuar. Coast Shelf S.*, 44:675–684, 1997.

[73] H.M. Nepf, J.A. Sullivan, and R.A. Zavistoski. A model for diffusion within emergent vegetation. *Limnol. Oceanogr.*, 42(8):1735–1745, 1997.

[74] H.M. Nepf and E.R. Vivoni. Flow structure in depth-limited, vegetated flow. *J. Geophys. Res.*, 105(C12):28547–28557, 2000.

[75] H.V. Nguyena, J.L. Niebera, P. Oduroa, C.J. Ritsemab, L.W. Dekkerb, and T.S. Steenhuisc. Modeling solute transport in a water repellent soil. *J. Hydrol.*, 215:188–201, 1999.

[76] K.J. Niklas. The scaling of plant and animal body mass, length, and diameter. *Evolution*, 48(1):44–54, 1994.

[77] C.F. Nordin and B.M. Troutman. Longitudinal dispersion in rivers: The persistence of skewness in observed data. *Water Resour. Res.*, 16(1):123–128, 1980.

[78] B. Oesterlé and L.I. Zaichik. Lagrangian time scales and particle dispersion modeling in equilibrium turbulent shear flows. *Phys. Fluids*, 16(9):3374–3384, 2004.

[79] North Carolina Division of Marine Fisheries. Coastal habitat protection plan 2005. Technical report, North Carolina Department of Environment and Natural Resources, Morehead City, North Carol., 2005.

[80] C.E. Oldham and J.J. Sturman. The effect of emergent vegetation on convective flushing in shallow wetlands: Scaling and experiments. *Limnol. Oceanogr.*, 46(6):1486–1493, 2001.

[81] A.D. O'Sullivan, B.M. Moran, and M.L. Otte. Accumulation and fate of contaminants (Zn, Pb, Fe and S) in substrates of wetlands constructed for treating mine wastewater. *Water, Air and Soil Pollution*, 157:345–364, 2004.

[82] M.A. Palmer, A.P. Covich, S. Lake, P. Biro, J.J. Brooks, J. Cole, C. Dahm, J. Gibert, W. Goedkoop, K. Martens, J. Verhoeven, and W.J. van de Bund. Linkages between aquatic sediment biota and life above sediments as potential drivers of biodiversity and ecological processes. *BioScience*, 50(12):1062–1075, 2000.

[83] M.R. Palmer, H.M. Nepf, T.J.R. Petterson, and J.D. Ackerman. Observations of particle capture on a cylindrical collector: Implications for particle accumulation and removal in aquatic systems. *Limnol. Oceanogr.*, 49:76–85, 2004.

[84] C.H. Peterson, R.A. Luettich, F. Micheli, and G.A. Skilleter. Attenuation of water flow inside seagrass canopies of differing structure. *Mar. Ecol. Prog. Ser.*, 268:81–92, 2004.

[85] D. Poggi, A. Porporato, L. Ridolfi, J.D. Albertson, and G.G. Katul. The effect of vegetation density on canopy sub-layer turbulence. *Bound.-Layer Meteorol.*, 111:565–587, 2004.

[86] J.H. Pollard. *A Handbook of Numerical and Statistical Techniques with Examples Mainly from the Life Sciences.* Cambridge University Press, 1979.

[87] A. Purnama. Boundary retention effects upon contaminant dispersion in parallel flows. *J. Fluid Mech.*, 195:393–412, 1988.

[88] A. Purnama. The effect of dead zones on longitudinal dispersion in streams. *J. Fluid Mech.*, 186:351–377, 1988.

[89] N.N. Rabalais, R.E. Turner, and Jr. W.J. Wiseman. Gulf of Mexico hypoxia, a.k.a. "The Dead Zone". *Annu. Rev. Ecol. Syst.*, 33:235–263, 2002.

[90] R.G. Randall, C.K. Minns, V.W. Cairns, and J.E. Moore. The relationship between an index of fish production and submerged macrophytes and other habitat features at three littoral areas in the great lakes. *Can. J. Fish. Aquat. Sci.*, 53 (Suppl. 1):35–44, 1996.

[91] M.R. Raupach, J.J. Finnigan, and Y. Brunet. Coherent eddies and turbulence in vegetation canopies: the mixing-layer analogy. *Bound.-Layer Meteorol.*, 78:351–382, 1996.

[92] M.R. Raupach and A.S. Thom. Turbulence in and above plant canopies. *Ann. Rev. Fluid Mech.*, 13:97–129, 1981.

[93] A.J. Roberts and D.V. Strunin. Two-zone model of shear dispersion in a channel using centre manifolds. *Q. Jl. Mech. Appl. Math.*, 57(3), 2004.

[94] O.N. Ross and J. Sharples. Recipe for 1-D Lagrangian particle tracking models in space-varying diffusivity. *Limnol. Oceanogr.: Methods*, 2:289–302, 2004.

[95] H. Schlichting. *Boundary-Layer Theory.* McGraw-Hill, New York, NY, 1955.

[96] B.H. Schmid. Simplification in longitudinal transport modeling: Case of instantaneous slug release. *J. Hydrol. Eng.*, 9(4), 2004.

[97] M. Schultz, H.-P. Kozerski, T. Pluntke, and K. Rinke. The influence of macrophytes on sedimentation and nutrient retention in the lower River Spree (Germany). *Water Res.*, 37:569–578, 2002.

[98] I.W. Seo and T.S. Cheong. Moment-based calculation of parameters for the storage zone model for river dispersion. *J. Hydraul. Eng.*, 127(6):453–465, 2001.

[99] S.K. Singh. Treatment of stagnant zones in riverine advection-dispersion. *J. Hydraul. Eng.*, 129(6):470–473, 2003.

[100] R. Smith. A delay-diffusion description for contaminant dispersion. *J. Fluid Mech.*, 105:469–486, 1981.

[101] R. Smith. A 2-equation model for contaminant dispersion in natural streams. *J. Fluid Mech.*, 178:257–277, 1987.

[102] J.H. Stansfield, M.R. Perrow, L.D. Tench, A.J.D. Jowitt, and A.A.L. Taylor. Submerged macrophytes as refuges for grazing cladocera against fish predation: observations on seasonal changes in relation to macrophyte cover and predation pressure. *Hydrobiologia*, 342/343:229–240, 1997.

[103] U. Stephan and D. Gutknecht. Hydraulic resistance of submerged flexible vegetation. *J. Hydrol.*, 269:27–43, 2002.

[104] B.M. Stone and H.T. Shen. Hydraulic resistance of flow in channels with cylindrical roughness. *J. Hydraul. Eng.*, 128(5):500–506, 2002.

[105] G. Strang. *Introduction to Applied Mathematics.* Wellesley-Cambridge Press, Wellesley, MA, 1986.

[106] G.I. Taylor. Dispersion of soluble matter in solvent flowing through a tube. *Proc. Roy. Soc. London Ser. A*, 219(1137):186–203, 1953.

[107] G.I. Taylor. The dispersion of matter in turbulent flow through a pipe. *Proc. Roy. Soc. London Ser. A*, 223(1155):446–468, 1954.

[108] W. C. Thacker. A solvable model of "shear dispersion". *J. Phys. Oceanogr.*, 6:66–75, 1975.

[109] The MathWorks, Inc., Natick, Massachus. *MATLAB, User's Guide*, 1992.

[110] D.J. Thomson, W.L. Physick, and R.H. Maryon. Treatment of interfaces in random walk dispersion models. *J. Appl. Meteor.*, 36:1284–1295, 1997.

[111] D.R. Tilley and M.T. Brown. Wetland networks for stormwater management in subtropical urban watersheds. *Ecol. Eng.*, 10:131–158, 1998.

[112] W.S.J. Uijttewaal, D. Lehmann, and A. van Mazijk. Exchange processes between a river and its groyne fields: Model experiments. *J. Hydraul. Eng.*, 127(11):928–936, 2001.

[113] E.M. Valentine and I.R. Wood. Longitudinal dispersion with dead zones. *J. Hydraul. Div. A.S.C.E.*, 103:975–990, 1977.

[114] A. van Masijk and E.J.M. Veling. Tracer experiments in the Rhine Basin: Evaluation of the skewness of observed concentration distributions. *J. Hydrol.*, 307:60–78, 2005.

[115] D. Velasco, A. Bateman, J.M. Redondo, and V. Demedina. An open channel flow experimental and theoretical study of resistance and turbulent characterization over flexible vegetated linings. *Flow, Turbulence and Combustion*, 70:69–88, 2003.

[116] J.J. Verduin and J.O. Backhaus. Dynamics of plant-flow interactions for the seagrass *Amphibolis antarctica*: Field observations and model simulations. *Estuar. Coast. Shelf Sci.*, 50:185–204, 2000.

[117] G. Voulgaris and J.H. Trowbridge. Evaluation of the acoustic Doppler velocimeter (ADV) for turbulence measurements. *J. Atmos. Ocean. Technol.*, 15:272–289, 1998.

[118] S.G. Wallis and J.R. Manson. Methods for predicting dispersion coefficients in rivers. *Water Management*, 157(WM3):131–141, 2004.

[119] V. Weitbrecht, W. Uijttewaal, and G.H. Jirka. 2-D particle tracking to determine transport characteristics in rivers with dead zones. In G.H. Jirka and W.S.J. Uijttewaal, editors, *Shallow Flows*, pages 477–484. A.A. Balkema Publishers, The Netherlands, 2004.

[120] T.M. Werner and R.H. Kadlec. Wetland residence time distribution modeling. *Ecol. Eng.*, 15:77–90, 2000.

[121] B.L. White, M. Ghisalberti, and H.M. Nepf. Shear layers in partially vegetated channels: Analogy to shallow water shear layers. In G.H. Jirka and W.S.J. Uijttewaal, editors, *Shallow Flows*, pages 267–273. A.A. Balkema Publishers, The Netherlands, 2004.

[122] B.L. White and H.M. Nepf. Scalar transport in random cylinder arrays at moderate Reynolds number. *J. Fluid Mech.*, 487:43–79, 2003.

[123] F.M. White. *Viscous Fluid Flow.* McGraw-Hill, New York, NY, 1974.

[124] U. Wilensky. Netlogo. Technical report, Center for Connected Learning and Computer-Based Modeling, Northwestern University, Evanston, Illin., 1999.

[125] A. Worman. Comparison of models for transient storage of solutes in small streams. *Water Resour. Res.*, 36(2):455–468, 2000.

[126] A. Worman, A.I. Packman, H. Johansson, and K. Jonsson. Effect of flow-induced exchange in hyporheic zones on longitudinal transport of solutes in streams and rivers. *Water Resour. Res.*, 38(1):2–1–2–15, 2002.

[127] W.R. Young and S. Jones. Shear dispersion. *Phys. Fluids*, A3(5):1087–1101, 1990.

[128] R. Zavistoski. Hydrodynamic effects of surface piercing plants. Master's thesis, Massachusetts Institute of Technology, 1994.

[129] M.M. Zdravkovich. *Flow Around Circular Cylinders*, volume 2: Applications. Oxford University Press, New York, 2003.